Molecular and structural determinants that contribute to channel function and gating in channelrhodopsin-2

By Ryan Richards

A dissertation submitted to the faculty of:

Worcester Polytechnic Institute

in partial fulfillment of the requirements for the Degree of Doctor of Philosophy in Biochemistry

March 2016

Approved:

Dr. Robert E. Dempski, Major Advisor

Dr. Arne Gericke, Committee Member

Dr. Shawn Burdette, Committee Member

Dr. William Kobertz, Committee Member

Acknowledgements

First and foremost I want to thank Rob for his continued guidance, support, and everlasting patience for the past 6 years. I will always be grateful for the opportunity he gave me transitioning from chemistry to biophysics and biochemistry. He somehow (amazingly) always kept my head on straight, despite the number of times I've walked into his office with frustration. He has always pushed me to be a better researcher and scientist, and I would not have been able to finish this without him. I should also apologize to him as well for constantly filling his inbox with terrible left shark, Star Wars, and Futurama memes.

Thank you to all my committee members – Arne, Bill, and Shawn for their time, support, and guidance throughout my PhD. They have always made themselves available to help me solve problems encountered along the way.

Thank you to our collaborators Sayan Mondal and Harel Weinstein at Cornell University, who contributed all of the computational work for the residual hydrophobic mismatch project and invaluable discussion.

I would also like to thank all of my lab members (and past lab members): Sagar, Beth, Vi, Ingrid, Louis for their friendship, guidance, and having to put up with my terrible puns, obscure references and my constant listening to Coheed and Cambria. You guys are the best.

I want to acknowledge the department of Chemistry and Biochemistry for funding my research and accepting me into the program and also the Extreme Science and Engineering Discovery Environment for funding our computational research. To Siamak Najafi and Raffaele Potami for their invaluable assistance in setting up our simulations and modeling. And finally Ann, who took care of every logistical problem I had here, and more importantly, always made sure I had plenty of coffee to keep me somewhat functional. I'm not sure what we'd do without you!

To my family – Mom, Dad, Adam, Jill, James, and all the Clays - I never would have gotten to where I am today without your love and support. I will forever miss being asked "so when are you done?"

And finally, to my amazing wife Molly – I can't even begin to put into words what your patience and love means to me. I don't know how you put up with me, but you've always been supportive and kept me going through the toughest days, weeks, and months. Thanks for keeping me sane and making me laugh, even on the worst of days.

Abstract

The green algae *Chlamydomonas reinhardtii* senses light through two photosensory proteins, channelrhodopsin-1 (ChR1) and channelrhodopsin-2 (ChR2). The initial discovery of these two photoreceptors introduced a new class of light-gated ion channels. ChR2 is an inwardly-rectified ion channel that is selective for cations of multiple valencies. Similar to microbial-rhodopsin ion pumps, ChR2 has a seven transmembrane domain motif that binds the chromophore all-trans retinal through a protonated Schiff base linkage. Physiologically, ChR2 functions to depolarize the membrane which initiates a signaling cascade triggering phototactic response. This fundamental property has been pivotal in pioneering the field of optogenetics, where excitable cells can be manipulated by light. ChR2 reliably causes neuronal spiking with high spatial and temporal control. Moreover, the recent discovery of new chloride-conducting channelrhodopsins (ChloCs) has further expanded the optogenetic toolbox.

Although structurally similar to microbial-rhodopsin ion pumps, ChR2 undergoes more complex conformational rearrangements that lead to ion conductance. Currently, the molecular basis for ChR2 gating remains unresolved. Revealing the specific structural interactions that modulate ChR2 function have important implications in understanding the intricacies of ion transport and molecular differences between ion pumps, channels, and transporters. Here we describe a combined computational and experimental approach to elucidate the mechanism of ion conductance, channel gating, and structure-function relationship of ChR2. Our results have contributed to expanding our understanding of the fundamental properties of ion channels.

Abbreviations

e_{12}: Transition parameter for O1 -> O2

G_{d1}: Transition rate parameter for O1 -> C1

5-HT2AR: serotonin receptor

ATR: All-trans retinal

bR: Bacteriorhodopsin

BSA: Bovine serum albumin

C1C2: Channelrhodopsin-1 and 2 chimera

CaTCh: Calcium conducting L132C ChR2 mutant

ChR: Channelrhodopsin

ChR1: Channelrhodopsin-1

ChR2: Channelrhodopsin-2

ChR2-XXL: T159C ChR2 mutant

ClC: Chloride channel

Cryo-EM: Cryogeneic electron microscopy

CTMD: Continuum-theory molecular dyanamics

EC: Extracellular

EDTA: Ethylenediamine tetraacetic acid

EPR: Electron paramagnetic resonance

E_{rev}: Reversal potential

FTIR: Fourier transform infrared spectroscopy

G_r: Thermal relaxation rate for C2 -> C1

GFP: Green fluorescent protein

GHK: Goldman-Hodgkin:Katz

GlpF: Glycerol facilitator in E. coli

GPCR: G-Protein coupled receptor

HA: Hemagluttanin

e_{21}:Transition parameter for O2 -> O1

G_{d2}:Transition rate parameter for O2 -> C2

I_p: Peak current

I_{ss}: Steady-state current

I-V: Current-voltage

KcsA: Potassium channel from *Streptomyces lividans*

LeuT: Bacterial neurotransmitter/sodium symporter

MscL: Mechanosensitive channel in *E.coli*

MTS: Methanethiosulfonate

MTSEA: 2-aminoethylmethane thiosulphonate

MTSES: 2-sulfonatoethylmethane thiosulphonate

MTSET: 2-trimethylammoniumethylmethane thiosulphonate

nAchR: Nicotinic acetylcholine receptor

NAMD: Nanoscale Molecular Dynamics

ODE: Ordinary differential equation

POPC: 1-palmitoyl-2-oleoyl-sn-glycero-3-phosphocholine

PVDF: Polyvinylidene fluoride

P_x/P_{Na}: Permeability ratio with respect to Na^+

RHM: Residual hydrophobic mismatch

RMSD: Root-mean squared deviation

ROS: Reactive oxygen species

SDS-PAGE: Sodium dodecyl sulfate polyacrylamide gel electrophoresis

SEM: Standard error of the mean

UV-vis: Ultraviolet-visible spectroscopy

V_m: Membrane potential

VMD: Visual Molecular Dynamics

HEK: Human embryonic kidney

k_1: Light-activation transition for C1 -> O1

k_2: Light activation transition for C2 -> O2

hRaR: Human retinoic acid receptor

IC: Intracellular

WT: Wild-type

ε: Quantum efficiency of retinal photo absorption

τ_{ChR2}: Time constant for ChR2 activation

τ_{decay}: Decay time constant

τ_{off}: Off time constant

Publications

Chapter 1:
Richards, R. and Dempski, R. E., From phototaxis to biomedical applications: Investigating the molecular mechanism of channelrhodopsins. Springer Series in Biophysics: Electrophysiology of unconventional channels and pores. Anne Delcour, editor. Springer US. (2015)

Chapter 2:
Richards, R. and Dempski, R. E., Re-introduction of transmembrane serine residues reduce the pore diameter of channelrhodopsin-2. *PLoS One*. 7, e50018 (2012)

Chapter 3:
Richards, R. and Dempski, R. E., Cysteine substitution and labeling provide insight into channelrhodopsin-2 ion conductance. *Biochemistry*. 54, 5665-5668 (2015)

Chapter 4:
Richards, R. and Dempski, R. E., Adjacent transmembrane residues regulate the two open states and progressive selectivity of channelrhodopsin-2. *Submitted, Scientific Reports* (2016)

Other publications:
Richards, R. and Dempski, R. E., Examining the conformational dynamics of membrane proteins *in situ* with site-directed fluorescence labeling. *J Vis Exp*. 51, (2011)

Chapter 5 publication in progress:
Mondal, S., **Richards, R**., Dempski, R.E., Weinstein, H. S., Residual hydrophobic mismatch in the cytoplasmic domain modulate channelrhodopsin-2 function. *In progress*

Table of Contents

Figure Index

Table Index

1 Introduction

The ability of unicellular organisms to optimize their light environment is a central component in the marine food chain. As part of the requirement for light optimization, all photosynthetic organisms have evolved a mechanism by which they can swim towards or away from light (phototaxis) (1). Phototaxis is essential not only for viability of a single organism, but for entire food chains. For example, in the marine food web, producers use light energy to orient themselves in an optimal light environment to use the energy of photons to create complex substances, such as sugars and amino acids. These producers include diatoms (ex. plankton and algae) as well as dinoflagellates. Producers are then eaten by first order consumers such as cleaner shrimp, copepodis and pteropoids. Consumers are ingested by subsequently larger organisms until reaching the top of the food chain. Therefore, conversion of light energy to complex substances is a requirement for homeostasis of the marine food web.

The physiology of light detection has been studied for nearly two hundred years. Studies on phototaxis originated in 1817 through the study of the algae *Draparnaldia* (2). Research in this field has ebbed and flowed since then. However the first molecular identification of the proteins which initiate the process of phototaxis within the past twelve years has precipitated an explosion of research in this field, both for basic science and as a tool for biomedical applications (1, 3-5).

Chlamydomonas reinhardtii is a single cell green alga which has been used as a model organism to study evolutionary biology, produce biopharmaceuticals as well as investigate phototaxis (6, 7). *C. reinhardtii* can thrive in fresh water as well as soil. It contains an eyespot region which is a photoreceptive organelle that enables the algae to sense light direction and intensity. Equally, *C. reinhardtii* has two flagella. These flagella swim asymmetrically upon light

exposure to change the direction of the alga. In the absence of light, *C. reinhardtii* can thrive when provided with complex substances. In comparison, *C. reinhardtii* is viable in media lacking organic carbon and chemical energy sources when illuminated. Therefore, *C. reinhardtii* is able to transform light energy into a driving force to make complex substances. This response system to light, which enables synthesis of complex compounds, likely includes a receptor which responds to the light stimulus, a transducer as well as a mechanism for controlling cell movement. Together, this complex behavior enables algae to swim towards (positive phototaxis) or away (negative phototaxis) from light to optimize their environment. In 2002 and 2003, it was shown that channelrhodopsin-1 (ChR1) and channelrhodopsin-2 (ChR2) are two light-stimulated ion channels that mediate the first committed step in photosynthesis (4, 5).

1.1 Channelopsins

Ion channels are proteins that facilitate the passive movement of ions down the electrochemical gradient. The rate at which ions permeate through channels is close to diffusion limits (10^7-10^9 ions/s) (8, 9). As such, channels are vital for signaling processes by rapidly changing the intracellular concentration of ions and are essential to electrical excitability of cells. The permeation pathway for channels includes a continuous pore region accessible to water and lined by specific residues which contribute to ion selectivity. Ion channels contain gating mechanisms that function to switch the channel between the open and closed states. In non-conducting states, channel gates prevent ions from passively moving across the membrane either through hydrophobic interaction or physical occlusion by residues in the pore region (9, 10). Gating mechanisms differ greatly between types of channels but typically require movements of the transmembrane domains or reorientation of residues lining the pore. Gating can be controlled through different stimuli including ligand binding, mechanical stress, or voltage.

With the recent discovery of channelrhodopsins, our understanding of these mechanisms has been expanded to light-gated channels.

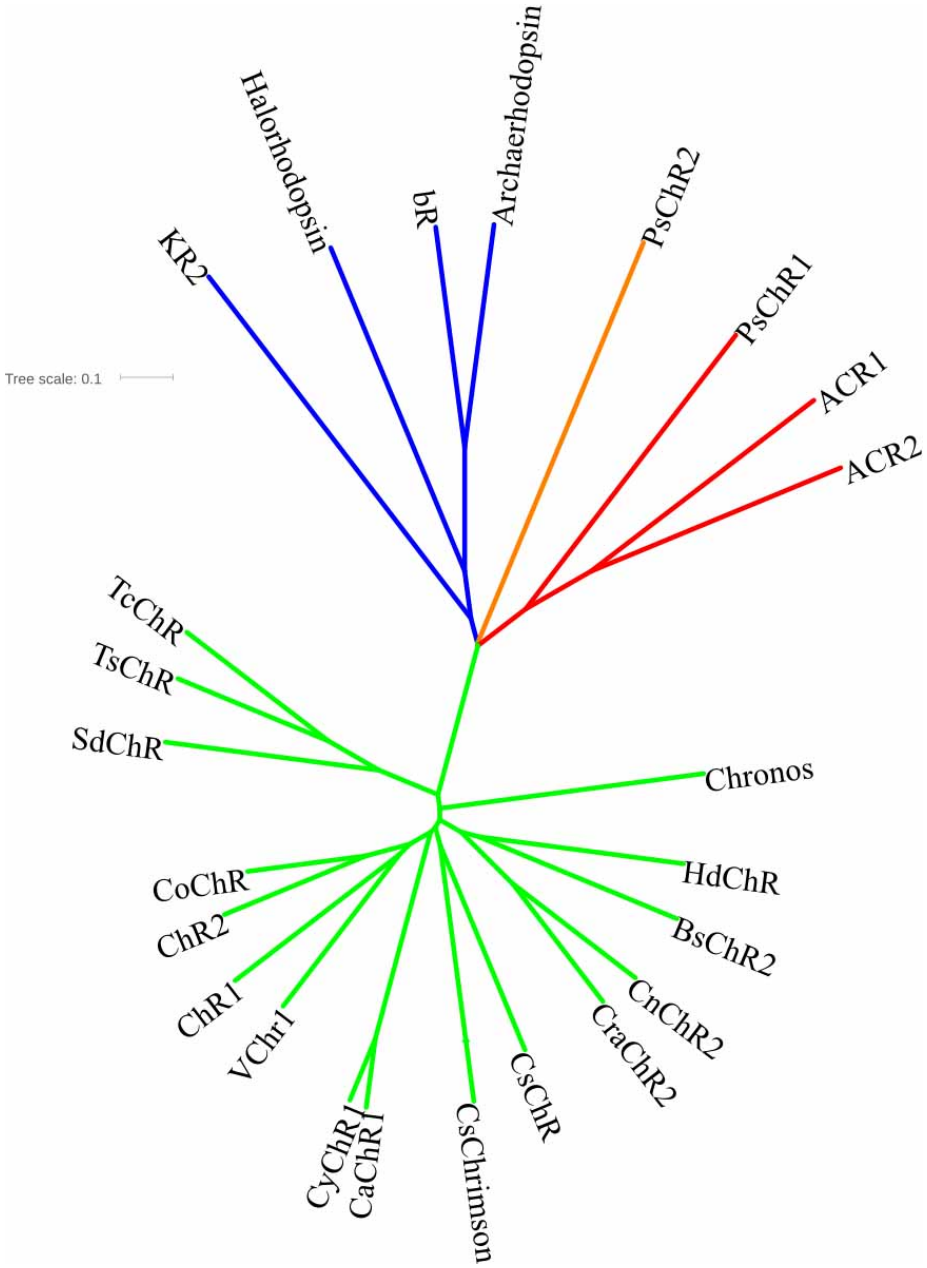

Figure 1.1.1- Phylogenetic tree of select microbial-rhodopsin pumps and channels
Nodes connected by green lines are known cation-conducting channelrhodopsins. Blue lines depict selected rhodopsin ion pumps. Red lines are known anion-conducting channelrhodopsins. Orange line is a cation ChR with unknown anion conducting properties. The scale represents percent genetic change.

The retinyldene containing microbial rhodopsins are a functionally diverse family of membrane proteins comprised of ion pumps and ion channels (Figure 1.1.1). Microbial rhodopsins are photosensory proteins that use light to regulate cellular processes in archaea, bacteria, and alga. Specifically, channelrhodopsins are light-activated ion channels that function as photoreceptors in algal species. The majority of known channelrhodopsins function as cation or proton channels causing a rapid depolarization of the cellular membrane which is the first committed step in phototactic response. This electrical stimulation causes an influx of Ca^{2+} through voltage-gated Ca^{2+} channels, which then transmits the light-response through a currently unknown signal cascade. The end result of this signaling is flagellate movement for algal orientation in light (11).

Conceptually, ChRs differ from retinylidene-containing ion pumps, such as bacteriorhodopsin, as ChRs facilitate passive downhill ion transport. In contrast, ion pumps are capable of transporting ions against the thermodynamic gradient. Recently, it has been suggested that this mechanistic difference between ion channels and ion pumps is due to the fact that channels have one or more gates which are open at the same time (12). When the gate (gates) is (are) open, ions are conducted down the chemoelectric gradient. In contrast, as pumps are performing uphill transport against the chemoelectric gradient, at least two gates are required to sequester ions from the gradient. These gates cannot be open at the same time as ions would flow back down the thermodynamic gradient and opposite of the desired direction. Therefore, it is likely that retinal isomerization induces a distinct conformational change in ChRs when compared to retinylidene-containing ion pumps which enables cations to be conducted down the chemoelectric gradient. However, at this time, the molecular underpinnings that differentiate ion

channels from ion pumps, especially as this relates to the opsin family of proteins, are not understood.

Recently, there has been a new discovery of anion-conducting channelrhodopsins, more commonly referred to as ACRs, in the species *Guillardia theta* and *Proteomonas sulcata* (13). ACRs are able to hyperpolarize the membrane more efficiently than microbial rhodopsin pumps, which are restricted to one charge movement per photon absorbed (14). Although channelrhodopsins function differently *in vivo*, the sequence homology is remarkably similar. There has been a concerted effort to discover and engineer new channelrhodopsins that are advantageous in the field of optogenetics.

1.2 Channelrhodopsin-2

Like other microbial-type rhodopsins, ChR2 is activated through the photoisomerization of all-trans retinal at C13 with blue light (~470 nm). Structurally, ChR2 is comprised of seven transmembrane spanning domains (TM) with a retinal moiety bound to a completely conserved lysine residue on helix 7 (K257 in ChR2) However, unlike other microbial rhodopsins, ChR2 is a light-activated cation channel, and not a pump (Figure 1.2.1A). ChR2 can conduct a large array of cations of multiple valencies, but has the highest affinity for protons. Large cationic molecules such as methylated amines can also pass through the channel. Interestingly, in the absence of an electrochemical gradient, ChR2 is able to outwardly pump H^+. The dual function of ChR2 has provided a unique platform to understand the molecular differences of ion channel and ion pump behavior.

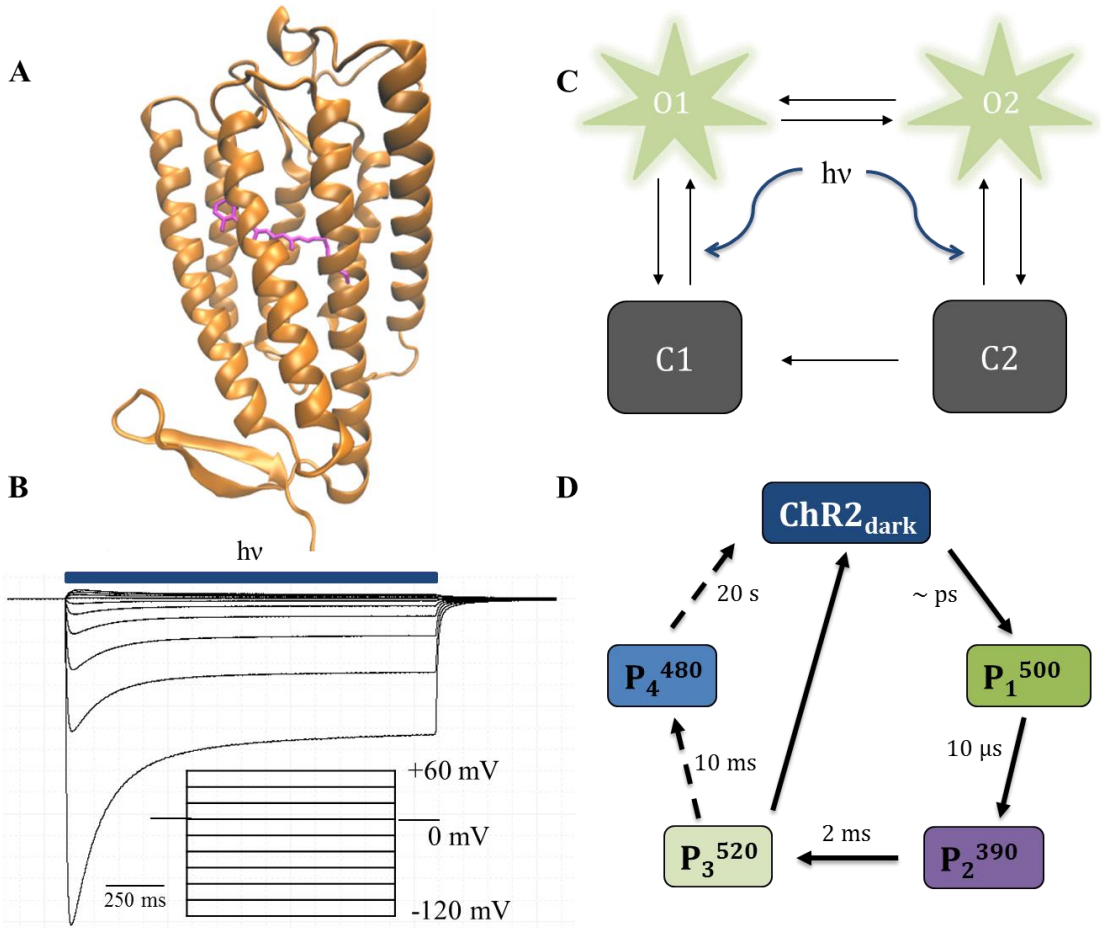

Figure 1.2.1 – Channelrhodopsin-2 structure and photocycle overview
(A) Homology model of ChR2 adapted from the C1C2 crystal structure. All images were created using Visual Molecular Dynamics Software (15) (B) Representative two-electrode voltage clamp recording of ChR2 current in oocytes under continuous illumination. Each trace is recorded at the corresponding membrane potential shown below (ΔV_m = 20 mV). (C) Continuous illumination photocycle with two open (O1 and O2) and two closed states (C1 and C2). Blue light initiates the photocycle to the O1 state. O1 transitions to O2 under constant illumination until the light is turned off, where ChR2 molecules enter the desensitized C2 state. With sufficient recovery in the dark, C2 thermally relaxes back to the ground state (C1). (D) Single turnover photocycle. Kinetic transition values represent the $\tau_{1/2}$ values. The large conformational changes of the backbone and hydration of the helices occurs prior to and persists through the P_3^{520} conducting state.

1.2.1 Channelrhodopsin-2 photocycles

Photoisomerization of retinal initiates the photocycle reaction and ion conductance in ChR2. Under continuous illumination conditions, ChR2 photocurrent decays from an initial peak current to a steady state. Turning the light off causes the steady state photocurrent to decay

bi-exponentially to the baseline (Figure 1.2.1B). The rates of these transitions vary with voltage and light intensity (5, 16) Interestingly, ChR2 exhibits highly reduced peak currents with subsequent light pulses commonly defined as ChR2 desensitization. This suggested that ChR2 can accumulate in a desensitized closed state after light illumination. The initial proposed photocycle used a three-state model to qualitatively describe ChR2 photocurrents (5). In this model, the closed state (C) transitions into an open state (O) during illumination with light (τ_{CO} = 0.2 ms, pH_i = 7.3). Turning the light off causes channel closure and transition from O to the dark desensitized state (D) (τ_{OD} = 20 ms, pH_i = 7.3). The D state relaxes back to the C state after prolonged recovery time in the dark (τ = ~ 2 s at pH_i = 7.3) (5). The possibility for a four state model was also proposed that used two open states with progressive ion conductance to explain the decay from peak to stationary current (16-18). Channel inactivation, typically described as the ratio of I_{ss}/I_p, where I_{ss} is the steady state current and I_p is the peak current, and the bi-exponential decay for this process is most accurately described by a model containing two open states and two closed states (16). For clarity, channel inactivation differs from channel desensitization. Desensitization refers to the reduction in photocurrent with subsequent light activation without adequate recovery in the dark whereas channel inactivation is a measure in the loss of photocurrent during prolonged light exposure (Figure 1.2.1B).

The current four-state photocycle model uses two open states (O1 and O2) and two closed states (C1 and C2) to quantitatively describe ChR2 photocurrents which previously could not be explained by the three-state model (Figure 1.2.1C) (16-18). Prior to light activation, ChR2 is accumulated completely in the C1 state. Immediately following light excitation, C1 rapidly transitions to O1. Under continuous illumination, O1 decays to O2. Here it is important to note that the peak current is not an accurate representation of O1 as the peak current is composed of a

mixture of O1 and O2 states (18). Rather, the peak current describes the moment at which the decrease in O1 and increase in O2 is equal, resulting in no temporal change in current. O1 can be determined by extrapolating the peak current to t=0. When the light is turned off, I_{ss} decays biexponentially to baseline, representing the O2 -> C2 transition. C2 thermally relaxes back to C1 after a recovery period in the dark. Without sufficient recovery between repetitive illumination cycles, the intensity of subsequent peak currents is reduced, while the stationary currents remain unchanged (5). The reduced I_p is indicative of a higher population of the O2 state as C2 can be directly converted to the lesser conducting O2 state by blue light. This results in a lower population of the high conducting O1 state and therefore, smaller peak current (Figure 1.2.1C). Analysis of computational studies has concluded that the experimental current requires a branched four-state photocycle (Figure 1.2.1C) to quantitatively model ChR2 photocurrent (16, 19-21).

An interesting scenario arises when ChR2 is activated with very short light pulses (< 2 ms). This results in a single turnover of ChR2. Under these conditions, I_p immediately decays back to baseline, and no I_{ss} is observed. Single turnover conditions offer a different view of a unidirectional ChR2 photocycle, where several states and intermediates have been elucidated by UV-Vis and time-resolved infrared spectroscopic measurements (Figure 1.2.1D) (22-24). Although it has been suggested that 6-8 exponentials are required to describe ChR2 kinetics, only four states have been spectroscopically identified under single turnover conditions (22, 23, 25-27). The photocycle described here only includes these identified states. Upon excitation, ChR2 transitions to the P_1^{500} non-conducting state in the picosecond range and undergoes a large conformational change in the backbone structure (24, 28). The conformational changes are likely driven by rearrangement of the hydrogen-bonding networks that govern interhelical

interactions (27). The prominent movement of the backbone structure precedes the conducting state of ChR2 and suggests that gating for cation translocation involves much smaller structural changes (24). Such fast and large conformational changes are an unusual property of ChR2 not seen in other microbial-type rhodopsin pumps. The photocycle of channelrhodopsin can be described as the following process.

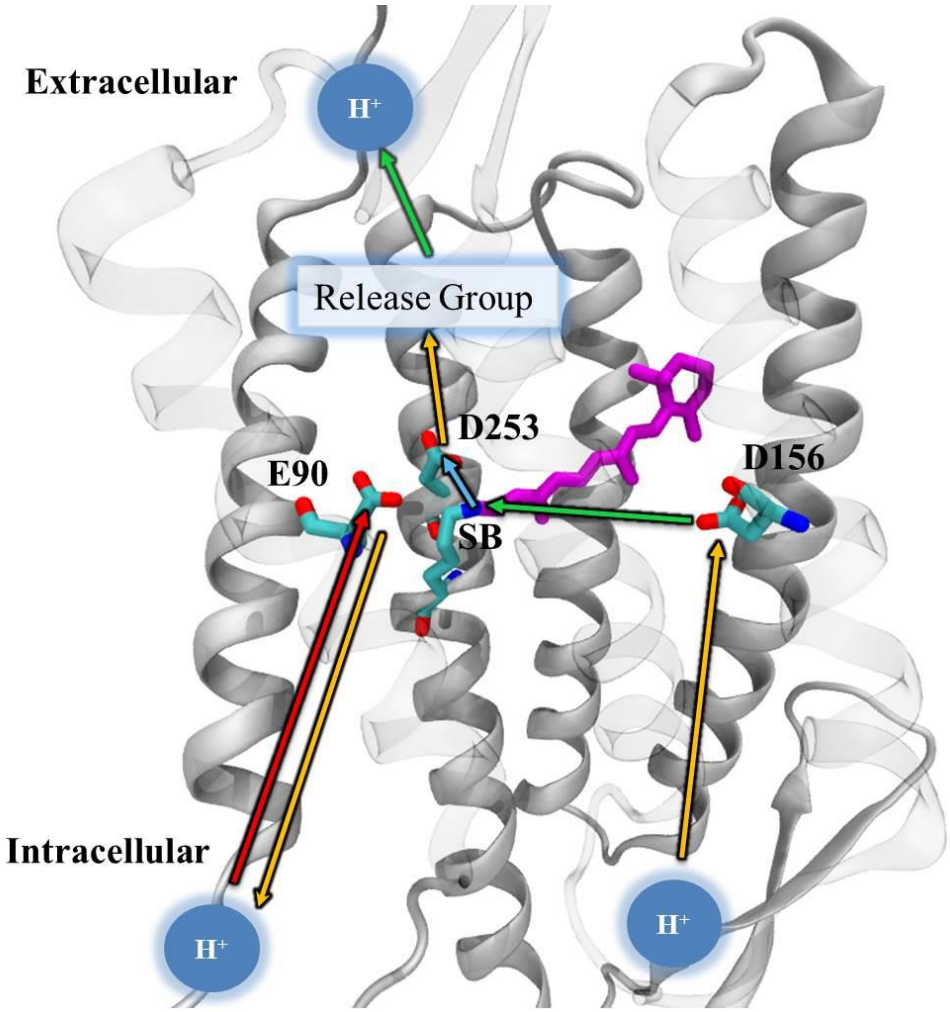

Figure 1.2.2 - Proton relay pathway in ChR2 adapted from Lorenz-Fonfria et al.
Blue arrow – Deprotonation of the SB representing the P_1^{500} -> P_2^{390} transition. Green arrows – Reprotonation of the Schiff base from D156 and release of proton from an unknown proton release group occurring during the P_2^{390} -> P_3^{520} transition. Orange arrows – Deprotonation of E90 and reprotonation of D156 during the P_3^{520} -> P_4^{480} transition. Red Arrow – Reprotonation of E90 during recovery from P_4^{480} to the ground state.

Deprotonation of the Schiff base by D253, the internal proton acceptor, leads to P_2^{390}, a non-conducting intermediate (Figure 1.2.1D) (22). Transition to the P_3^{520} conducting state occurs after reprotonation of the Schiff base by the internal proton donor D156 (Figure 1.2.2, green arrows). Furthermore, rise of P_3^{520} occurs simultaneously with the release of a proton to the extracellular side from an unidentified release group. Interestingly, the release of this proton is uncoupled to the deprotonation of the Schiff base as D253 remains protonated throughout the conducting state (27). The rise of the P_4^{480} non-conducting state is concomitant with channel closing kinetics. This transition involves the reprotonation of D156 and deprotonation of E90. E90 resides in the putative pore region and deprotanation of this residue suggests an important step for gating ChR2 (24, 29). P_4^{480} represents the desensitized channel state which decays back to ground state after ~10 s (22). The transition back to the ground state can be accelerated at low pH values, where it is coupled to proton uptake (Figure 1.2.2). This correlates with reprotonation of E90 that occurs during the $P_4^{480} \rightarrow$ ground state transition (24). There is also evidence that the P_4^{480} state is actually part of a branching photocycle, where only ~25% of ChR2 molecules enter from P_3^{520} (27). The remaining ChR2 molecules relax directly to the ground state. Here, large structural changes that occur in the initial excitation of the channel persist through the $P_3^{520} \rightarrow P_4^{480}$ transition. These structural changes do not reverse until the channel enters P_4^{480}, but the process is much slower than the onset (24).

1.2.2 Functional relevance of the Schiff base donor/acceptor and 'DC gate'

Originally, it was thought that the internal proton acceptor from the Schiff base was E123. E123 in ChR2 is the homologous residue to the proton acceptor in bR (D85). (22, 30-32). However, the crystal structure of the C1C2 chimera (ChR1 – helices 1-5; ChR2 – helices 6-7)

revealed that the distance between E123 and the Schiff base was 3.4 Å, but only 3.0 Å for D253. Therefore, it was proposed that D253, not E123, was the internal proton acceptor (33). This was later experimentally determined by monitoring protonation changes of specific residues via time-resolved FTIR spectroscopy in the P_2^{390} state (27). This also provided explanation as to why the E123T mutation (ChETA variant) results in little change for the rise and decay kinetics of P_2^{390} and P_3^{520} and a similar current-voltage relationship to WT ChR2 (27, 34). Moreover, the D253E mutation results in nearly a 50-fold increase in kinetics for the deprotonation of the Schiff base ($P_1^{500} \rightarrow P_2^{390}$ transition). This is analogous to the ~30-fold increase in M-state formation of the D85E mutant in bR (27, 35). An acidic residue at D253 in known ChRs is completely conserved, but not at E123, providing strong evidence of D253 as the proton acceptor.

It is well established that inter- and intramolecular non-covalent forces present in membrane proteins are critical for proper folding, insertion in the membrane, and transport functions (30, 36-40). An integral force that has been of great relevance to ion channels is the hydrogen bonding network within transmembrane domains. The importance of hydrogen bonding in ChR2 has also been observed to be crucial for proper function (41, 42). In bR two residues, T90 and D115, form an interhelical hydrogen bond between TMs 3 and 4 which is critical for proton pumping and photocycle kinetics (43). Sequencing alignments reveal that residues at these two positions are highly conserved among archael rhodopsins and ChR2, where the homologous residues are C128 and D156 (44). Therefore, it was proposed that D156 on TM 4 and C128 on TM 3 formed a putative hydrogen-bond that was closely tied to the photoreaction and the conducting state lifetime (24, 45). The hydrogen bond between C128 and D156 was named the "DC Gate" in reference to how TMs 3 and 4 are linked. To investigate the role of these residues in ChR2 function, mutations at C128 (C128X series) with threonine, serine or

alanine caused a 100-10,000 fold increase in the conducting state lifetime achieved through retardation of closing kinetics after light is turned off (Figure 1.2.3) (31). Mutations at C128 also affect the ground state spectrum due to the proximity to the retinal chromophore. A similar phenotype was observed for D156A (Figure 1.2.3) (41). Analysis of FTIR experiments suggested that a hydrogen-bond was present between the carbonyl oxygen of D156 and the thiol group on C128. Furthermore, the proposed hydrogen bond was present at different strengths in the P_1^{500} (stronger) and P_4^{480} (weaker) photointermediates (45). Replacing D156 with the larger glutamic acid removed the interaction with C128 in both states, while the C128T mutant retained the interaction in the P_1^{500} state. Additionally, the position of the D156 C=O stretching vibration indicates protonation, is sensitive to the presence of C128, and suggests hydrogen-bonding to an undetermined residue. Therefore, it was hypothesized that the interaction between D156 and C128 was responsible for the small structural changes that gate ChR2 conductance after large backbone movement induced by light excitation.

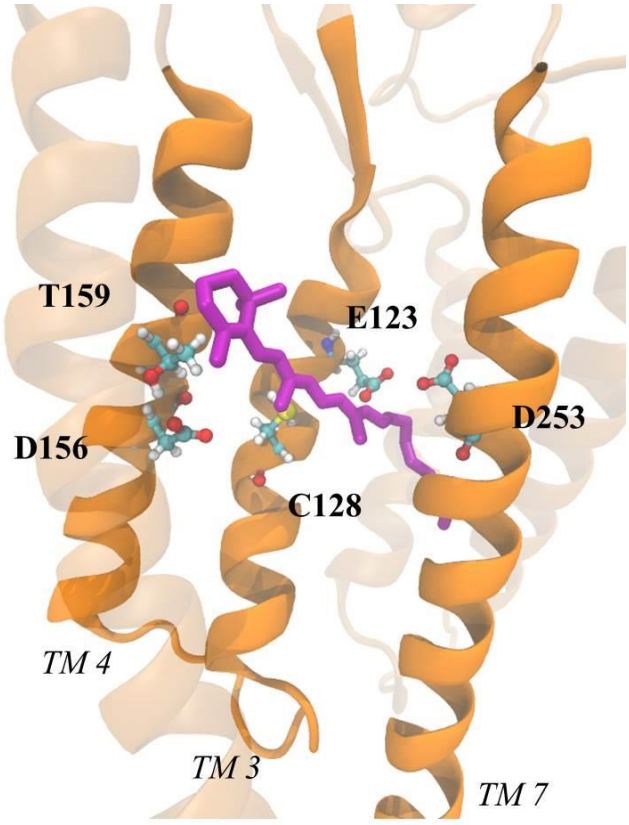

Figure 1.2.3 – Kinetically sensitive residues
ChR2 homology model highlighting residues which affect photocycle kinetics. The distance between D156 and C128 (DC gate) is too far for direct hydrogen bonding. TM 6 is not shown for clarity.

However, recent evidence has suggested that the distance between D156 and C128 is too far for a hydrogen bond to be formed and functions differently than the analogous gate in bR (33, 46, 47). The crystal structure of the C1C2 chimera calculated the distance between D156 and C128 to be 4.4 Å (33). Here, the distances in the crystal structure correspond to the ChR1 structure. Analysis of molecular dynamic simulations of C1C2 hinted at the instability of the conformation of the two residues (47). Interestingly, MD simulations performed by Watanabe and colleagues on a ChR2 homology model suggested that a water mediated hydrogen-bond forms between C128 and D156. Further simulations utilizing the C128T mutation showed the absence of water in the same region, and may explain the slow photocycle kinetics of this

mutant. More recently, analysis of time-resolved FTIR experiments elucidated D156 as the internal proton donor for retinal (27). This explains why the conducting state lifetime is increased for the D156A as reprotonation of the Schiff base becomes the rate limiting step. Additionally, the recent D156C mutation (ChR2-XXL) has a long open state, significantly increased light sensitivity and expression, and the largest photocurrent of all known ChR variants thus far (38 ± 10 μA at -100 mV compared to 2 ± 0.5 uA for WT) (48). The functional role of C128 is unclear; however it is proposed that by it lowers the pK_a of D156 for reprotonation of the Schiff base. A similar result has also been observed for the T90A mutation in bR (49).

1.2.3 Channel Selectivity, Conductance, and Function

One of the most interesting features of ChRs is that, despite the sequence homology to other microbial rhodopsins, it functions as an ion channel *in vivo* and not an ion pump. The ClC family of channels and transporters are also known to include transporters and channels with structural homology (50). Substitution of a single glutamate residue can transform the Cl^-/H^+ exchanger into a channel for the passive transport of Cl^- (51-53). Although transporters and channels function very differently, structurally they are similar. To this end, microbial rhodopsins, and particularly ChR2, can be used to tease out the molecular determinants that govern channel/transporter behavior. Even more unique to ChR2 is that in the absence of an electrochemical gradient, it can act as an outwardly driven proton pump (54). Proton release for ChR2 occurs with reprotonation of the Schiff base. This is in contrast to bR, where proton release is coupled with deprotonation of the Schiff base (Figure 1.2.2) (55, 56).

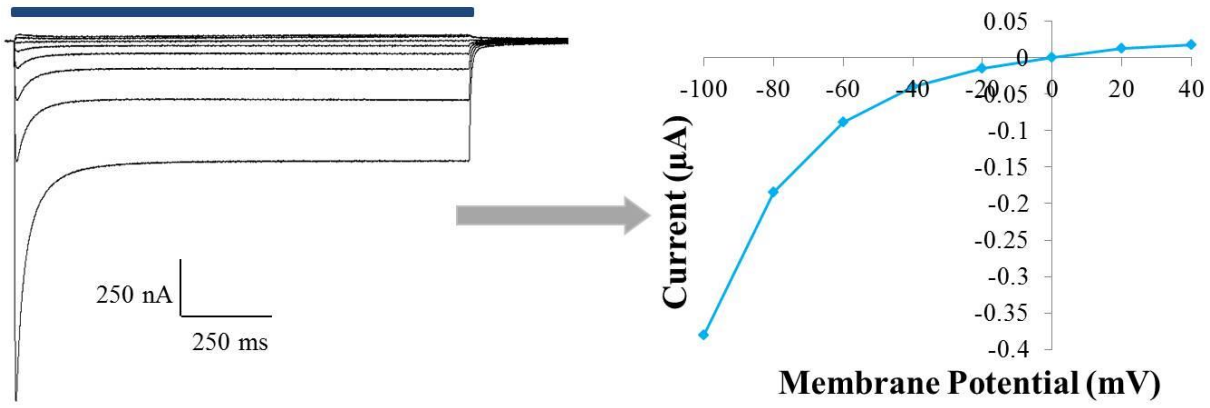

Figure 1.2.4 – Representative ChR2 photocurrent traces and corresponding I-V relationship

Photocurrent traces are recording at different holding potentials under voltage-clamp conditions. The current at each voltage is determined and plotted to generate an I-V curve. I-V curve are used to determine the reversal potential under specific ionic conditions.

The ion conductance properties of ChR2 have been most often measured using electrophysiology. ChR2 can be expressed heterologously into light-insensitive cells, usually *Xenopus laevis* oocytes or in mammalian cells such as human embryonic kidney (HEK) cells. This allows for the precise control of the extracellular buffer conditions and, under patch clamp conditions, control of the intracellular buffer. It also enables a facile method to examine changes in ion conductance upon mutagenesis. Photocurrents are measured under specific ionic conditions at different holding potentials which can be used to generate current-voltage curves and elucidate the reversal potential (E_{rev}) of the channel (Figure 1.2.4). E_{rev} is the membrane potential at which current flowing through the channel changes direction. For ChR2, reversal potentials can be used to determine the relative permeability of ions flowing through the channel and also the progressive selectivity of ions between O1 and O2.

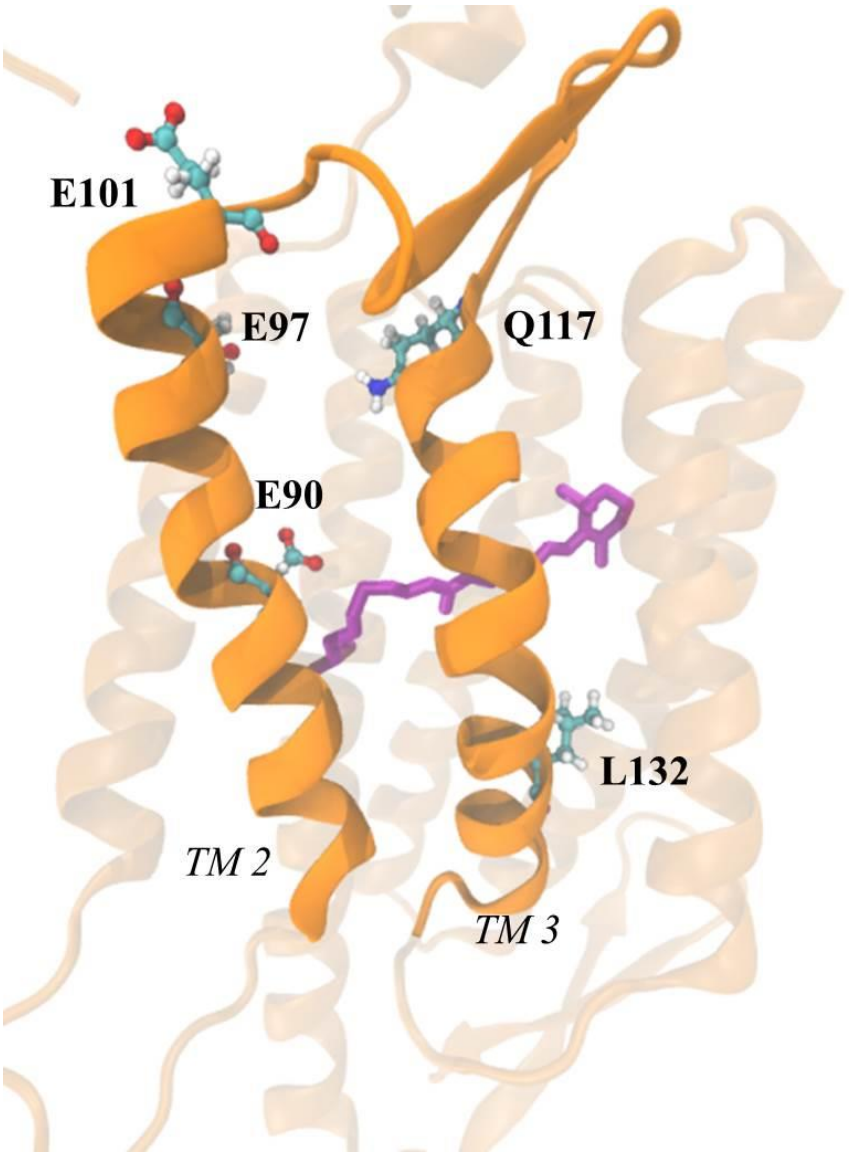

Figure 1.2.5 – Residues that affect selectivity in ChR2
The pore region of ChR2 is lined with several charged polar residues that are important for cation selectivity. Retinal is shown in magenta.

ChR2 can conduct a wide array of cations with differing selectivity (5). ChR2 has the highest affinity for protons, which is about 10^6 fold higher than that of the alkali metals. Likewise, alkali metals are ~10 to 100-fold more selective over alkaline metals. The selectivity among periodic groups decreases with increasing atomic radius, consistent with the hydration shell being stripped during translocation (5). Even large cationic compounds can permeate the

channel, such as methyl- and dimethyl-amine. This is suggestive of a pore diameter larger than voltage-gated sodium channels, but smaller than the nicotinic acetylcholine receptor (5, 57).

TM2 contains multiple charged polar residues facing the pore that contribute to permeability and kinetics (27, 33, 58). Three charged glutamate residues (E90, E97, and E101) have the largest effect on the selectivity of Na^+ and H^+ (58, 59). Charge inversion mutations introduced at these positions significantly reduced Na^+ and H^+ photocurrents at pH 4, and produced negligible currents at alkaline and neutral pH (29, 58, 59). Interestingly, the E90K mutation has no Na^+ conductance but large photocurrents at pH 4, which were originally attributed to H^+ flux. However, no change in reversal potentials at different pH values was observed (29). It was later discovered that this mutation, along with E90R, turned ChR2 into an outward rectified Cl^- channel with minimal conductance for cations (60).

TM3 has also been found to be important for ion conductance and selectivity. Five cysteine mutations located on the extracellular side of TM3 (R115C, Q117C, E123C, L132C, I133C), when treated with the cysteine-specific reagents 2-aminomethanthiosulfonate (MTSEA) and 2-sulfonatoethyl-methanethiosulfonate (MTSES), exhibited significantly increased or reduced photocurrents compared to untreated cells (61). Analysis of these experimental results suggested these residues line part of the conducting pathway. Mutation of Q117 to glutamate showed reduced permeability ratios for alkali metals when compared to WT ChR2. Q117 sits at the interface of extracellular and transmembrane domains and it was reasoned that a hydrogen bond (broken in the Q117E mutant) plays a role in the dehydration of cations entering the pore (Figure 1.2.5).

1.2.4 Models for ChR2 conductance and selectivity

Understanding photocycle kinetics is important for elucidating the mechanism of ion transport and ion selectivity. Several kinetic models have been applied in tandem with electrophysiological measurements to describe photocurrents and ionic composition (Figure 1.2.6) (18, 59, 62). These models have an advantage over the Goldman-Hodgkin-Katz (GHK) equation because ChR2 is non-selective for various cations and these ions do not move independently through the channel. Additionally, ChR2 is a multi-valent channel which is not accounted for in the standard GHK equation (8). Three state and four-state kinetic models, described by Nikolic et al., were able to fit ChR2 photocurrent measurements under short (2 ms) and prolonged light exposure. Although this three state model reproduced photocurrents qualitatively, it could not accurately describe the light-off currents. Instead, the four-state model with an added open state term was able to quantitatively fit ChR2 photocurrents. Here, it is important to note that O1 and O2 have differing ion selectivity and that kinetic models need to account for these differences. Therefore, models were not only extended to reveal selectivity between ions, but also the selectivity between conducting states. The selectivity between open states was first observed using electrophysiological recordings near the reversal potential. At these membrane potentials, inward peak currents switched to outward current during the steady-state. The ionic selectivity between the two states was further elucidated using differences in reversal potentials between peak and stationary currents. It was found that the selectivity for H^+ over monovalent metals (Na^+ and/or K^+) was ~ 10^6 in O1 (18). Furthermore, the preference for divalent metals (Ca^{2+} and/or Mg^{2+}) over monovalent metals was ~0.01. Lastly, during the transition to O2, the divalent metal selectivity decreases 2-fold. These results showed that ChR2 specificity increases temporally under prolonged light pulses. Based on these results, it was suggested that, with

respect to *C. reinhardtii* physiology, this mechanism appears to be a way for the cell to save energy during prolonged light exposure (18).

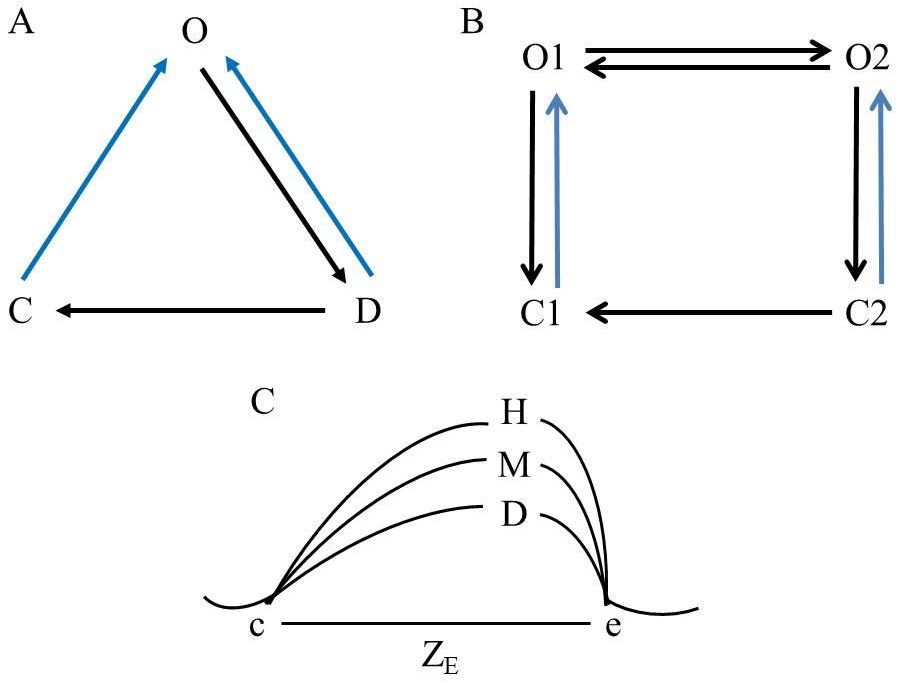

Figure 1.2.6 – Kinetic and enzyme models of ChR2
(A) Three-state photocycle model used to qualitatively reproduce ChR2 photocurrents. (B) Current four-state kinetic model used to quantitatively describe the ChR2 photocycle. (C) Proposed enzyme binding model using three substrates (H – H^+; M – Na^+ and K^+; D – Ca^{2+} and Mg^{2+}) and an asymmetric barrier to describe the I-V relationship of ChR2.

In comparison, Hegemann and colleagues utilized an enzyme model to elucidate the ionic composition of initial and steady-state photocurrents under conditions where there is a large inward driving force (59). This model could accurately recreate the magnitude of photocurrents of wild-type ChR2, the ChR1 and *Volvox carteri* ChR1 chimera (C1V1), and the highly calcium permeable L132C mutant (CatCh). The model also predicted the ionic compositions of the currents. Another enzyme kinetic model was applied to fit the non-linear current-voltage relationship of ChR2 (62). Determination of the kinetic rate constants of the ChR2 photocycle reaction indicated which parameters had the largest effect on the non-linear I-V relationship.

Moreover, it was found that the empty binding site had an apparent charge of about -0.3 and rectification of ChR2 is caused by non-linear transport and competition between cations permeating the channel. Elucidation of the underlying mechanisms and kinetics of the photocycle reaction are imperative for the implementation of ChR2 as an optogenetic tool.

1.2.5 Helix tilt model for ChR2 gating

The first structural information on ChR2 came from projection map images using cryo-electron microscopy (63). It was not until the crystal structure of the ChR1-ChR2 chimera (C1C2; ChR1 TM 1-5, ChR2 TM 6-7) was solved that the putative pore of ChR2 was found to form between transmembrane helices 1-3 and 7 (33). An open vestibule in this region on the extracellular side is lined with polar residues (Figure 1.2.7). This water accessible pathway is occluded on the cytoplasmic side by two constriction sites. The first site is composed of S63, E90, and N258 which are highly conserved across ChRs. Mutations made at E90 (A or Q) and N258 (D) alter cation selectivity while E90Q, N258D, and S63D affect kinetics (33). The central restriction site provides a hydrophobic barrier through a network of interconnected hydrogen-bonds in the dark state. The inner occlusion site is composed of the sterically bulky Y70 on TM 1 (33). Together, these sites prevent water from entering the region between the gates (33, 60).

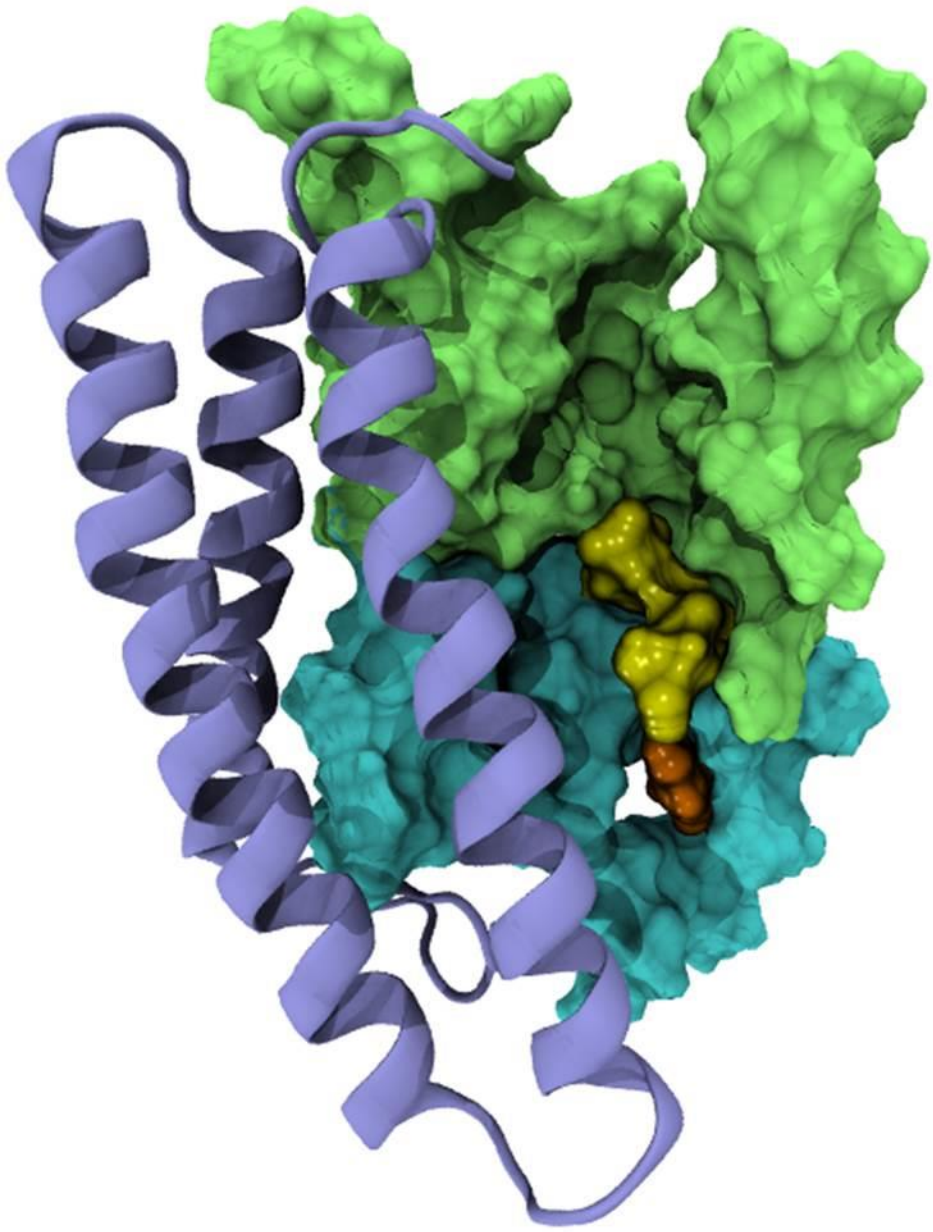

Figure 1.2.7 - Homology model of the conducting pore region of ChR2
The extracellular side of the channel contains an open vestibule (lime color) where cations enter the pore. The pore is constricted by two occlusion sites. The first site of S63, E90, and N258 (yellow) blocks the extracellular side while the second site is formed by Y70 (orange) and blocks the intracellular side. The bottom half of the pore is colored cyan and helices 4-6 are colored blue. For clarity, TM 7 is not shown but also lines the conducting pore.

Experiments utilizing spin-labeled ChR2, EPR spectroscopy, MD simulations, and time-resolved FTIR have begun to resolve the following mechanism for ion conductance. Retinal isomerization protonate D253 and induces movement of N258 on TM 7. This movement disrupts one of two proposed hydrogen-bonds formed between N258 and E90. Breaking of the N258/E90 hydrogen bond subsequently allows E90 to reorient and cause a large conformational change in TM2. There is also large movement observed for TMs 6 and 7, likely caused by the disruption of the complex hydrogen-bonding network at the central and inner gates (64). As a result, an influx of water molecules hydrates TM helices in two distinct phases (fast and slow) (65). The fast component makes up one-third of the hydration and occurs prior to ion conductance with a time constant of 10 μs. This correlates with deprotonation of the Schiff base and reorientation of E90. The slow component makes up the remaining two-thirds of the helical hydration and is concomitant with ion conductance. It remains unresolved whether the rate limiting step for ion conductance, and thus pore formation, is the tilt of TM2 or the influx of water. Furthermore, it is unknown what discrete changes occur within the pore to transition ChR2 into the open state.

1.3 Color tuning of Channelrhodopsins

The discovery of new ChRs has proven beneficial in examining the molecular determinants that contribute to channel activation and selectivity. Initially, the closest structural and sequence homologs were those of microbial-type rhodopsins such as bR. However, homology cloning performed on *C. yellowstonensis, C. augustae, and C. raudensis*, algal species that exhibit similar light-mediated photocurrents to *C. reinhardtii*, produced several new ChR variants (66). These new ChRs had variable kinetic parameters and activation wavelengths when

compared to ChR2 although they shared similar domains and motifs. Additional ChRs were discovered by transcriptome sequencing of 127 algal species (67). From these sequencing experiments, 61 algal opsins were discovered and characterized by their function in different wavelengths of light, kinetics, and recovery.

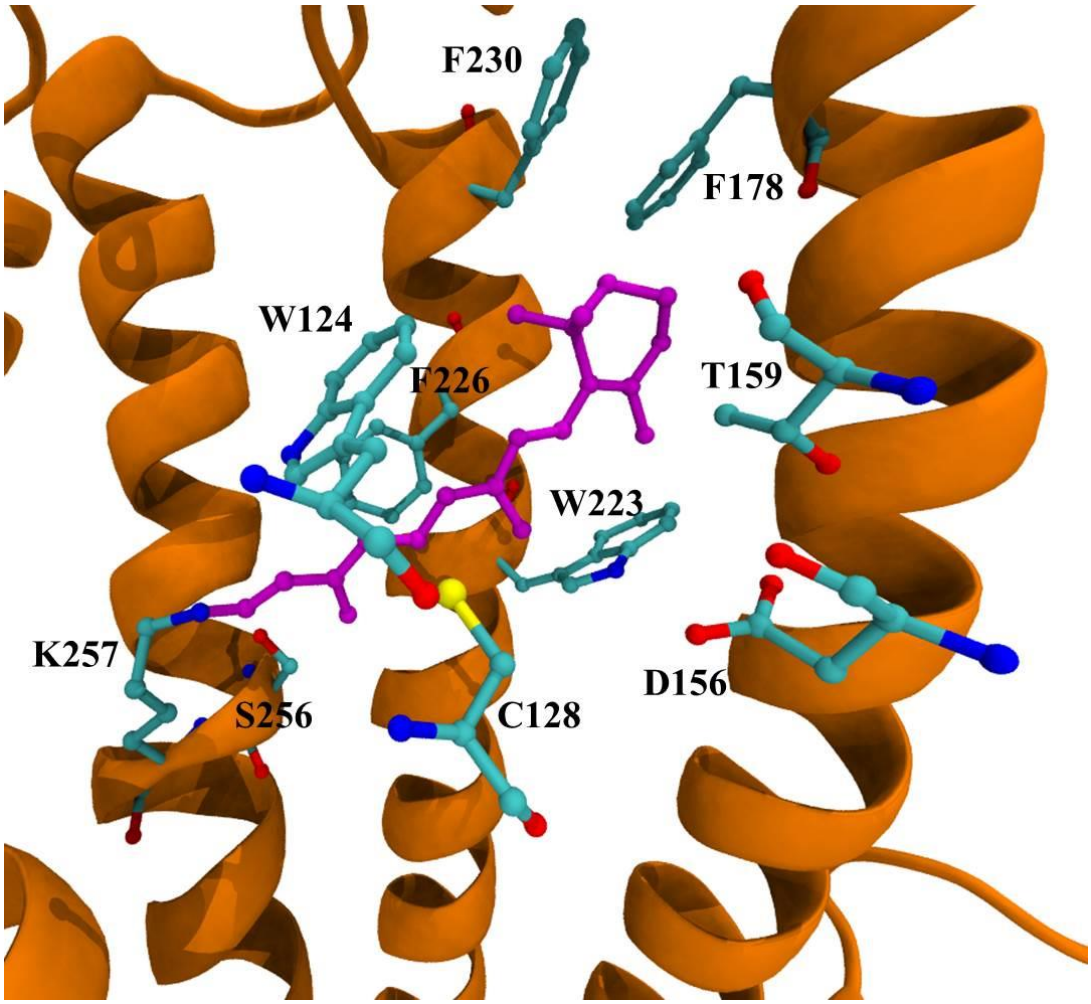

Figure 1.3.1 – ChR2 retinal binding pocket
Residues lining the ChR2 retinal binding pocket. Retinal displayed in magenta.

The activation wavelength of ChR2 has become of particular interest to researchers for multi-wavelength activation of cells containing distinct populations of engineered ChR2 mutants. Several factors affect the activation wavelength and wavelength shifts within retinylidene

proteins. These include the counterions near the Schiff base, the electrostatic environment surrounding retinal, the geometry of retinal, and the hydrogen-bonding environment (68, 69). The C1C2 crystal structure revealed that the retinal binding pocket is lined by W124, D156, F178, W223, F226, and F230 (Figure 1.3.1) (33). It was also suggested that three residues forming a pocket around the β-ionone ring (C128, T159, and S256) may also contribute to the color shift of ChR2 compared to bR (556 nm). Known ChRs contain a highly conserved glutamate (E123 in ChR2) and completely conserved aspartate (D253 in ChR2) that are both in close proximity to the Schiff base. D253 has been identified as the proton acceptor of the Schiff base in the photocycle reaction (27), while E123 was identified as the original internal acceptor (Figure 1.2.3) (22, 27, 31). Action spectrum recordings of the blue-shifted PsChR (found in *Platymonas subcordiformis)* found that mutations at the homologous positions E106 and D236 to Q and N caused a red-shift in the spectrum. The same mutations made at E123 and D253 had a similar effect on ChR2(69). Absorption experiments with the E123T (neutral) and E123D (negative) mutations revealed a red-shift in the ChR2 spectrum (70). Although it is counter-intuitive that a conserved charge mutation (E123D) would have the same effect as a charge inversion (E123Q), the red-shifted spectrum likely occurs from the distortion of the local geometry by the extra methylene or from alteration of the hydrogen-bonding network (70). Interestingly, the homolgous E123T mutation in a chimera ChR comprised of ChR1 and VChR1 produced a blue-shifted spectrum, suggesting structural differences at the counterion site between ChR1 and ChR2 (71).

The discovery of new ChRs has revealed interesting insights on some of the molecular determinants that influence spectral shifts in channel activation. Correlations can be made from newly discovered ChRs, the structure and composition of the retinal binding pocket, and spectral

characteristics. Understanding the structural elements that govern retinal absorbance is of significant importance to the optical control of cells. Blue light activated ChRs are disadvantageous because biological tissue scatters lower wavelengths of light (72). Therefore, there is a concerted effort to discover and engineer new ChRs that are activated by red light for greater tissue penetration. The recently discovered Chrimson ChR, found in the algal species *Chlamydomonas noctigama*, has the farthest red activated spectrum yet discovered at 660 nm (67). The action spectrum for this protein is 45 nm more red-shifted than the engineered ReaChR variant, which used a chimeric approach with ChR1, VChR1, and ChR2 (73). Compared to ChR2, Chrimson has several differences in the residues lining the retinal binding pocket. S256 and T159, which surround the ring structure, are alanine and methionine in Chrimson, respectively. Furthermore, residues that line the pore differ between ChR2 and Chrimson. D156 is a cysteine while the two hydrophobic aromatics F178 and F226 are tyrosine residues. These changes to the environment surrounding the chromophore may account for the large shift in absorbance.

1.4 Application to optogenetics

Recognition that channelopsins could be used as a tool to control excitable membranes was acknowledged upon the first molecular characterization of ChR2 where Bamberg and colleagues wrote "expression of ChR2…may be used as a powerful tool to increase cytoplasmic Ca^{2+} concentration or to depolarize the cell membrane, simply by illumination" (5). The first experiments fulfilling this idea came only two years later when it was shown that excitable membranes could be manipulated in a light-dependent manner using ChR2 (74). Here mammalian hippocampal neurons were transformed with ChR2-YFP (yellow fluorescent

protein) using a lentivirus. Light-activation of ChR2 was sufficient to generate a threshold potential which resulted in neuronal spiking. Equally, neuronal spiking could be resolved on the millisecond time scale. In these experiments, both excitatory and inhibitory synaptic transmission could be controlled upon the light-induced activation of channelrhodopsin. A glimpse of the impending wide utility of these proteins to control neuronal cells was soon established as it was also shown that ChR2 could also be used to control the membrane potential of PC-12 cells (75).

While using ChR2 to control neuronal spiking in cell-based experiments was an exciting development, it was subsequently shown that ChR2 could be used as a tool to manipulate whole animal preparations. Here, Herlitze and colleagues electroporated a GFP-ChR2 gene, under the cytomegalovirus (CMV) promoter into the spinal cords for stage 16 (embryonic day 2-3) chick embryos (76). At embryonic day 4.5-5, the spinal cord and hind limbs were separated and the GFP-ChR2 fusion protein was found distributed in motor and interneurons. Equally, when exposed to continuous light, it was observed that electroporation did not have a deleterious effect on the development of cord circuits, but did increase the frequency of neuronal firing using suction electrode recordings.

The first successful *in vivo* utilization of ChR2 as a tool to control the behavior of an organism was achieved by the Gottschalk group where ChR2 was functionally expressed in excitable cells of *Caenorhabditis elegans* (77). When ChR2 was expressed and activated upon light stimulation in muscle cells, muscle contractions were observed. Equally, following functional expression of ChR2 in mechanosensory neurons light-induced activation of ChR2 induced withdrawal behaviors which are normally associated with mechanical stimulation. This work was an important benchmark in establishing ChR2 as a tool to study excitable cells in

living organisms. Of course, a point which cannot be over-emphasized in this and other studies is the observation that no externally applied retinal is required for the functional expression of channelrhodopsins. If delivery of retinal was required for channelrhodopsin function, then the technical challenges to successfully use this protein as a tool in tissues and organisms would greatly increase. However, it is apparent that even in intact brain tissue, sufficient retinal is available to generate a sufficient population of ChR2 to induce threshold activation upon light stimulation.

The development of ChR2 functional expression in intact organisms opened a new wave of research strategies to apply ChR2 as a tool to investigate cellular processes. These included using ChR2 as a tool to treat retinal degenerative diseases by injecting ChR2 into mouse and rat eyes, triggering appetitive or aversive learning in *Drosophila* larvae, investigating long-term potentiation in rat hippocampal slice cultures, learning behaviors, sleep, as well as mapping circuits between presynaptic and postsynaptic neurons (78-83).

While ChR2 has become a powerful tool to investigate excitable membranes, limitations arise due to the excitation wavelength, ion conductance and kinetic properties and the absence of a mechanism to inhibit action potentials. Therefore, there has been a sustained effort to identify new constructs either through discovery of new channelrhodopsin homologs or manipulation of known genes. Considering that phototaxis is a well-established biological process through multiple organsisms, it is no surprise that related microbes have light activated cation channels with differing properties. One of the first of these novel proteins to be identified was isolated from *Volvox carteri* and named channelrhodopsin (VChR1) (84). This protein has a red-shifted excitation maximum at 589 nm when compared to ChR2 (470nm). Identification of this protein, for the first time, enabled simultaneous investigation of the interaction of different cell types in

circuit computation or behavior. Equally, light at this longer wavelength can penetrate tissue further enable investigation of more distal cells in intact organisms.

In a parallel avenue of research, there has been an emphasis to identify ChR mutants with novel properties. For instance, mutation of L132 to cysteine in ChR2 also revealed a construct with enhanced calcium permeability (CatCh mutant, Figure 1.2.5) (85). Considering that some excitable membranes, most notably heart tissue, are controlled by changing the cytosolic concentration of calcium, identification of this construct has facilitated a new method to control heart tissue (20, 86-88). Finally, it has been demonstrated that the D156C mutation results in a construct, named ChR2-XXL, which has extra high expression and a longer open-state lifetime (Figure 1.2.3) (89). This construct was successfully used in *Drosophila melanogaster* to investigate innate male courtship and olfactory memories.

1.5 Summary

Starting with its central role in phototaxis, the behavior and mechanism of channelrhodopsins has been studied for nearly two hundred years. The past five years have seen an increased effort to fully resolve the residues and underlying mechanisms that contribute to the unique function of ChR2. Equally, identification of mutants and recent sequencing efforts has uncovered a growing array of proteins with novel functionality. These new ChRs have greatly advanced the field of optogenetics, allowing for greater spatio-temporal precision to optically control cells. However, it is clear that a better understanding of the ChR2 photocycle is required in order to fully utilize and engineer mutants for practical applications. Resolving the mechanism for function would also provide a deeper understanding of the intricacies of ion transport and what molecular differences determine functionality between ion pumps, channels, and transporters. To this end,

our objective was to tease out molecular determinants that contribute to ChR2 selectivity, gating, and ion permeation.

2 Re-introduction of transmembrane serine residues reduce the minimum pore diameter of channelrhodopsin-2

2.1 Introduction

The activation mechanism for various ion channels varies greatly between families. Although different, the complex conformational rearrangements that occur in the helical backbone structure of ion channels function to facilitate pore formation (8, 9, 90). Channel gating requires TM helical movement in order to initiate the beginning steps of opening the pore. Several models exist including helical rotation, helical bending, and helical tilt; the latter being the current model for ChR2 (64). After the large TM movements, smaller structural changes within the pore region are required for ion conductance and occur by breaking/forming hydrogen bonds or spatial reorientation of residues. Equally, non-covalent forces, such as inter- and intrahelical hydrogen bonding and helix-helix interactions are critical for proper folding, insertion, and function of membrane proteins (30, 36-38, 91-93). The hydrogen-bonding network present in the TM region is especially important to sense larger conformational movements and link the helices together. Specifically, serine and threonine residues have been shown to be involved in helical packing interactions and motifs (37). A high percentage of serine and threonine residues found within the transmembrane domains of membrane proteins form hydrogen bonds with carbonyl oxygen atoms in the backbone structure or other polar amino acids (30, 91). These hydrogen bonds stabilize protein structures and can be involved in ion transport across the cellular membrane.

ChR2 shares a high sequence homology with other microbial-type rhodopsins, but in contrast with these proteins, ChR2 functions mainly as a cation channel and not an ion pump. However, it has been shown that when ChR2 is reconstituted in planar lipid membranes in the absence of an electrochemical gradient, it functions as an outwardly rectified proton pump (54). Thus, it has been proposed that ChR2 is a proton pump with an inherent leak current that exhibits

ion channel properties. More recent evidence suggests that proton and cation flux occur through separate pathways, contributing to the dual function (64).

ChR2 also undergoes large conformational changes when compared to other opsin proteins (24). These structural changes have been attributed to the backbone movement of the channel through FTIR and Raman difference spectroscopy. Analysis of EPR experiments utilizing spin-labeled ChR2 confirmed the large conformational changes in helical structure (94). Large helical movements, which occur before and after the conductive state, suggest that pore formation precedes gating upon activation of the channel. Cryo-EM experiments that used a trapped open state of ChR2 revealed that TMs 2, 6, and 7 undergo rearrangement during the photocycle. While the movement of TMs 6 and 7 is similar to other rhodopsin ion pumps, the change in TM 2 is unique to ChR2 (64). TM 2 has been shown to confer ion selectivity for ChR2 by electrophysiological experiments (29, 58, 60). The dual function as a proton pump and cation channel may involve two separate pathways, where the proton path is controlled by TMs 6 and 7 as in rhodopsin pumps and TM 2 facilitates the channel function. Thus, the hydrogen-bonding network within the TMs of ChR2 is an important factor for conformational flexibility and function.

An analysis of the sequence of ChR2 reveals that this protein lacks specific residues which contribute to non-covalent forces in bacteriorhodopsin (bR). These residues have been shown to play a role in the hydrogen-bonding network and overall stability of bR (30, 93, 95).

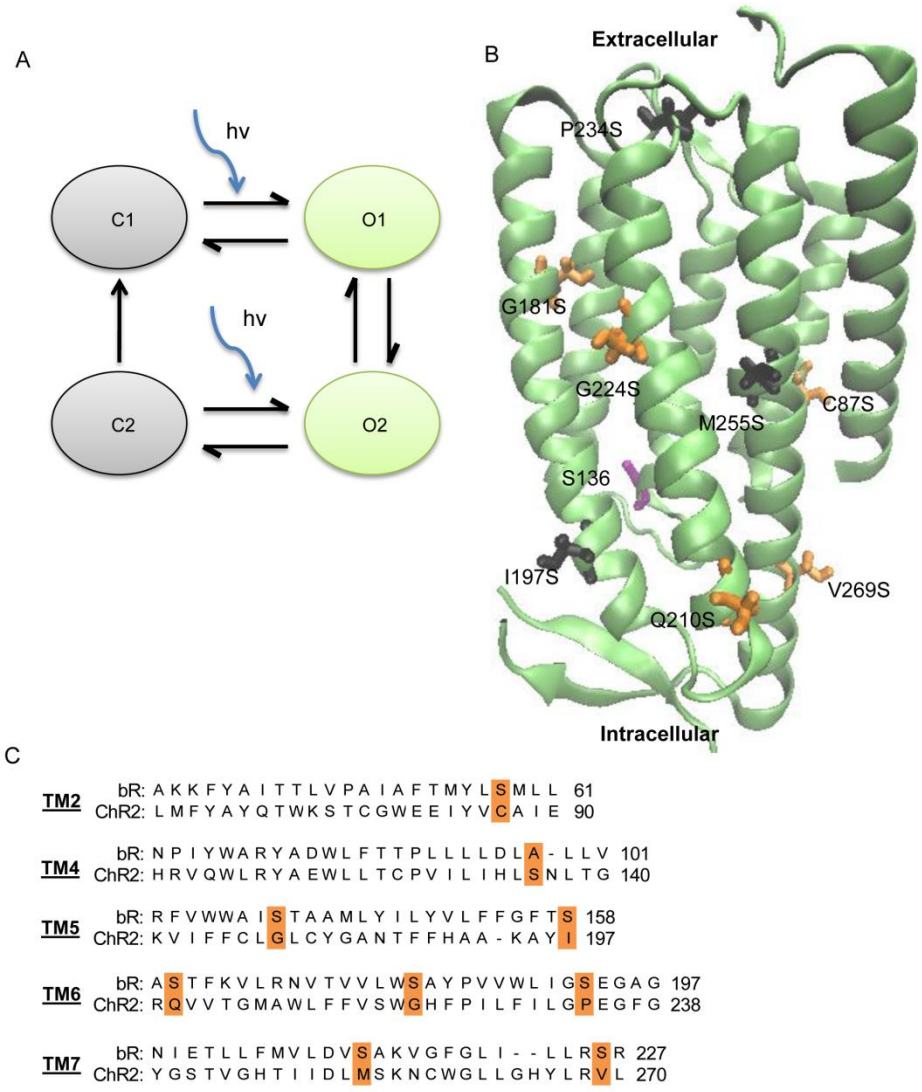

Figure 2.1.1 – Simplified ChR2 photocycle and model highlighting single serine mutations

(A) Simple four-state model of the channelrhodopsin-2 photocycle as described in chapter 1. (B) Structural model of ChR2 based on the channelrhodopsin chimera C1C2 (PDB entry: 3UG9) highlighting the locations of serine mutations. Three residues (black) had highly reduced photocurrents, while 5 mutations showed changes in pore size, permeability, and/or kinetics (orange). Residue S136 is shown in purple. Retinal is shown in yellow. (C) Sequence comparison of transmembrane domains between bacteriorhodopsin and channelrhodopsin-2. Residues that correspond to serine mutations are highlighted in orange.

Specifically, there are eight serine residues within the transmembrane domains of bR that are not present in ChR2. Previously, these residues in bR were individually mutated to Ala in order to disrupt the hydrogen-bonding and proton transfer network (95). It was shown that some, but not

all, serine mutations had altered proton pumping ability, kinetics, and chromophore regeneration. Additionally, all eight mutants were functional pumps. These experiments elucidated specific residues that contribute to the stability and structural changes of bR through hydrogen-bonding, but are not essential for proton transport.

The importance of hydrogen-bonding between specific residues has also been observed in ChR2 (41, 42). Mutations located at C128 have been shown to increase the conduction lifetime of ChR2 (18). C128, located on helix 3, has been proposed to form a hydrogen bond with D156 on helix 4 and is important for proper channel function. This hydrogen bond pair is consistent throughout most microbial-type rhodopsins (44). In bR, the pair corresponds to T90 and D115 where its contribution to protein stability has been studied previously (43, 95). Neither residue is directly involved in the proton conduction pathway, but disruption of this hydrogen-bond alters the kinetics and proton pumping ability. However, the recent crystal structure of the channelrhodopsin chimera C1C2 shows that the distance between the thiol group of C167 and carboxyl oxygen of D196, which correspond to C128 and D156 in ChR2, is 4.4 Å, too large for hydrogen-bonding (33). Instead, it was suggested that the thiol group interacts with the conjugated region of the retinal moiety.

Why ChR2 undergoes much larger structural changes compared to other opsin proteins is still unknown. However, ChR2 lacks specific residues and motifs that contribute to inter- and intrahelical interactions that are present in other microbial-type rhodopsins. We hypothesized that reintroduction of the eight transmembrane serine residues present in bR, but not in ChR2, will restrict the conformational flexibility and reduce the pore diameter of ChR2. In our present work, we created single serine ChR2 constructs that correspond to homologous residues in bR (Figure 2.1.1). We used two-electrode voltage clamp techniques on *Xenopus laevis* oocytes to

study channel permeability, kinetics, and pore size in varying alkali metal solutions. ChR2 has an estimated pore size larger than voltage gated sodium channels (~4.7 Å) but smaller than the nicotinic acetylcholine receptor (~8.4 Å) (5, 96, 97). Minimum pore sizes can be determined using excluded volume theory and can help elucidate specific residues involved in forming the narrowest region of the pore (97, 98). Three substitutions, I197S, P234S, and M255S, resulted in largely reduced photocurrents compared to wild-type ChR2. Furthermore, G224S showed changes in permeability and kinetics while C87S, V269S, G181S and Q210S showed changes in permeability and pore size with no effect on kinetics. Lastly, S136A resulted in a larger minimum pore diameter. These results indicate the importance of hydrogen-bonding on the ChR2 pore size, conformational flexibility, and ion selectivity. An analysis of our experiments demonstrates that the size selectivity filter for ion conductance is not located at a single region within the transmembrane domains. Instead determinants that contribute to ion conductance are distributed along the intracellular side of channelrhodopsin-2.

2.2 Materials and Methods

2.2.1 Ethical animal treatment

Isolation of *Xenopus laevis* oocytes were performed in strict accordance to the guidelines given in the Guide for the Care and Use of Laboratory Animals of the National Institutes of Health. The surgical protocol was approved by the WPI Institutional Animal Care and Use Committee (protocol number- A3277-01). Surgery was performed using the anesthetic tricaine to minimize animal suffering.

2.2.2 Reagents

The mMessage mMachine SP6 kit was purchased from Ambion, Inc. (Austin, TX). Restriction enzymes were acquired from New England Biolabs, Inc. (Ipswich, MA). The

Quikchange site-directed mutagenesis kit was bought from Stratagene. (La Jolla, CA). All other reagents were purchased from Sigma-Aldrich Corp. (St. Louis, MO) unless otherwise noted.

2.2.3 Molecular Biology

A truncated wild type channelrhodopsin-2 (ChR2, amino acids 1-309) with the hemagluttanin (HA) epitope sequence (YPYDVPDYA) was unidirectionally cloned into the vector pTLN [32] using *EcoRV* and *XbaI* restriction sites. Serine mutations were made using the Quikchange site-directed mutagenesis kit. All mutations were verified by full gene sequencing.

2.2.4 Oocyte preparation and mRNA synthesis

Oocytes were isolated according to previously published protocols (99). In brief, oocytes were obtained via collagenase digestion (3 mg/mL; 3 hours, 17^{o}C, shaking) in ORI^{+} solution (90 mM NaCl, 2 mM KCl, 2 mM $CaCl_2$, 5 mM MOPS; pH 7.4) after partial ovarectomy of *Xenopus laevis* frogs. ChR2 mRNA was prepared using the SP6 mMessage and mMachine kit. A volume of 50 nL of 1 μg/μL mRNA was injected into each oocyte and incubated in ORI^{+} containing 1 mg/ml gentamycin and 1 μM all-trans-retinal (1 mM stock in DMSO) in the dark at 17^{o} C for 3-4 days.

2.2.5 Oocyte membrane preparation and Western blotting

Xenopus oocyte total membrane fractions were prepared as described previously (100, 101). Briefly, oocytes were homogenized in 20 μL/oocyte homogenization buffer A (20 mM Tris, 5 mM $MgCl_2$, 5 mM NaH_2PO_4, 1 mM EDTA, and 80 mM sucrose; pH 7.4) supplemented with 1 mM PMSF and 5 μg/ml leupeptin and pepstatin A, Homogenized oocytes were spun at 200 g for 5 minutes at 4^{o}C. After removal of supernatant, centrifugation was repeated. The supernatant was removed and spun at 14,000 g for 20 minutes at 4^{o} C to pellet the membrane.

Protein samples were solubilized in 4 µl/oocyte Laemmli buffer and incubated at 37^{o} C for 30 minutes for denaturing.

Protein samples were separated on a 12% gel using SDS-PAGE and transferred onto PVDF membranes. The membranes were blocked in 3% BSA overnight at 4^{o}C. Blocked membrane were incubated with anti-HA polyclonal antibody (1:1000; Thermo Fisher Scientific, Waltham, MA) for 1 hour at room temperature. Membranes were washed 3 times for 10 minutes in TBST (0.1%) and incubated with an AP conjugated anti-rabbit secondary antibody (1:5000; Rockland Inc., Gilbertsville, PA). The ChR2 band was visualized using developing solution (Bio-Rad Laboratories Inc., Waltham, MA).

2.2.6 Electrophysiology

Microelectrodes were fabricated by pulling borosilicate glass capillaries (World Precision Instruments, Sarasota, Florida) using a PC-10 pipette puller (Narishige, Japan). The microelectrodes had resistances between 0.5-2.0 MΩ. Oocytes were placed in an RC-10 oocyte chamber (Warner Instruments, LLC; Hamden, Connecticut). Solutions were introduced to the chamber using a VC-6 6 channel perfusion valve control system (Warner Instruments LLC; Hamden, Connecticut). Activation of ChR2 was achieved using 75 W xenon arc lamp (Specialty Optical Systems, Inc., Dallas, Texas) and 2 mm light guide (~4 x 10^{21} photons s^{-1} m^{2}). Currents were measured using a Turbo-Tec 03X amplifier (npi electronic GmbH, Germany) set to voltage clamp mode. The membrane potential was varied from -120 mV to +60 mV in 20 mV steps. Data was recorded using pClamp10 software (Axon Instruments, Inc., Burlingame, California) and further analyzed using Clampfit 10.2 and SigmaPlot. Apparent kinetic values were determined by fitting current traces to a biexponential equation at -120 mV in Na^{+} solution.

2.2.7 Minimum pore diameter estimation

The minimum pore diameter of ChR2 was calculated using excluded volume theory (97, 102). In brief, the permeability of an ion moving through a channel is proportional to the region left unoccupied by the ion. Plotting the square-root of permeability ratios versus ionic radius, a linear regression is observed according to the equation:

$$\sqrt{\frac{P_x}{P_{Na}}} = a - bR_x \qquad (1a)$$

$$a = \frac{R_c}{R_c - R_{Na}} \qquad (1b)$$

$$b = \frac{1}{R_c - R_{Na}} \qquad (1c)$$

where R_x is the radius of ion X^+, R_c is the radius of the channel, and R_{Na} is the radius of the sodium ion. Calculating 2a/b gives the minimum pore diameter of the channel.

2.2.8 Structural modeling of ChR2

Structural models were created using Visual Molecular Dynamics software with PDB entry 3UG9 (15, 33). Serine residues were inserted into the structure by creating an automatic protein structure file (psf) from 3UG9. Next, the psf was modified using the mutator plugin for VMD to insert serine residues at the homologous positions in the model.

2.3 Results

Eight individual serine mutations were made at residues that corresponded to transmembrane serine residues in bR. Mutations were located in various areas of the transmembrane domain; C87S, G181S, G224S, and M255S were located near the retinal binding pocket, I197S, Q210S, and V269S were located at the cytoplasmic end of the transmembrane domain, and P234S was located at the extracellular end of the transmembrane domain (Figure

2.1.1). ChR2 constructs were expressed in *Xenopus laevis* oocytes and photocurrents were recorded using two-electrode voltage clamp techniques. Photocurrent measurements were made in the presence of 115 mM alkali metal solution (115 mM XCl, 2 mM $BaCl_2$, 1 mM $MgCl_2$, Tris; pH 9). Function of mutant constructs was determined by measuring photocurrents at -120 mV in 115 mM Na^+ solution and compared to WT ChR2 photocurrents on the same day (Figure 2.3.1A). The mutants I197S, P234S, and M255S were functional, but had highly reduced photocurrents (Figure 2.3.1B). Surface expression of I197S, P234S, and M255S was determined by Western blotting (Figure 2.3.1C). Both I197S and M255S have similar band intensity compared to WT ChR2, suggesting that these mutations have reduced functionality. Conversely, P234S showed very low expression compared to the wild-type. However, because of the low photocurrents I197S, P234S, and M255S were not analyzed further. The five mutants that were measured retained typical inwardly rectified behavior (Figure 2.3.1D).

To measure permeability ratios of mutant ChR2 constructs, we measured shifts in reversal potential using Li^+, K^+, Rb^+, and Cs^+ solutions (pH = 9) relative to Na^+ for individual constructs. Typical electrophysiological recordings for each mutant are shown in Figure 2D. Mutants retained the inwardly rectified current of WT ChR2 in each alkali metal solution. Photocurrents were normalized to the largest signal in Na^+ solution on the same day for E_{rev} analysis. Large negative changes in E_{rev} were observed for C87S (ΔE_{rev} = -47 ± 1 mV; Rb^+) and V269S (ΔE_{rev} = -52 ± 1 mV; Rb^+) in the presence of larger cations when compared to WT ΔE_{rev} values (ΔE_{rev} = -29.2 ± 0.4 mV; Rb^+). A negative shift in reversal potential indicates that the channel becomes less permeable to cation X^+. In contrast, G224S had much smaller shifts in E_{rev} (ΔE_{rev} = -14.2 ± 0.1 mV; K^+) which indicated alkali metals became more permeable relative to other constructs and the phenotype (ΔE_{rev} = -27.9 ± 0.5 mV; K^+). Both G181S and Q210S had

mixed results, with both larger and smaller shifts in E_{rev} compared to WT ChR2 (Table 2.3.1). Interestingly, three mutants (G87S, G181S, and V269S) had highly positive sodium E_{rev} indicating an increased selectivity for this ion over the other alkali metals. Other mutants had Na^+ E_{rev} similar to wild type.

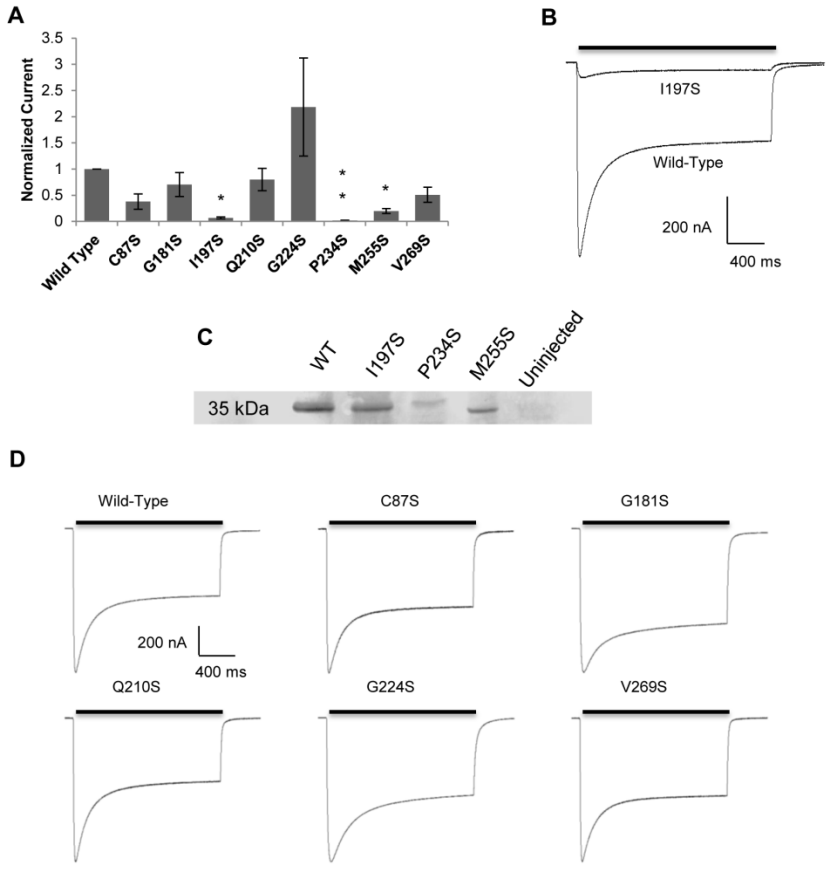

Figure 2.3.1 – Representative single serine electrophysiology traces

Black bars indicate illumination with 473 nm light. (A) Normalized photocurrent traces. Mutant photocurrents were normalized to WT ChR2 on the same day in 115 mM Na^+ solution at pH 9. Values are reported as mean ± S.E.M (n = 3-9). Statistically significant values are denoted by a * (* $P<0.001$; ** $P<0.04$). (B) Reduced photocurrent for I197S compared to WT ChR2 on the same day. M255S and P234S had similar results. (C) Western blot of I197S, P234S, and M255S ChR2 mutants. ChR2-HA tagged band appears at ~ 35 kDa. (D) Typical electrophysiological recordings for single serine mutants. Mutants retained inward rectification of cations, but with altered permeability, kinetics, and/or inactivation ratios.

Next, we used ΔE_{rev} to calculate relative permeability ratios, P_x/P_{Na}, of each ion for ChR2 mutants. Changes in E_{rev} between X^+ and Na^+ for each mutant were used to exclude differences in the cytoplasmic ionic composition of oocytes. Ratios were calculated relative to 115 mM Na^+ solution for each ChR2 mutant (Table 2.3.1). Values > 1 indicated a higher permeability for cation X^+ over Na^+, where values < 1 indicated reduced permeability for cation X^+. In general, the largest changes in permeability ratios were seen for the larger cations (K^+, Rb^+, and Cs^+). V269S showed highly reduced permeability ratios when compared to WT in all solutions. In contrast, G224S had higher permeability ratios when compared to WT except for P_{Cs}/P_{Na}, where it was comparable to WT.

Solution	Construct	ΔE_{rev} (mV)	P_x/P_{Na}
Li^+	WT	-1.8 ± 0.3	0.929 ± 0.16
	C87S	-3.1 ± 1.1	0.881 ± 0.15
	G181S	-7.3 ± 0.1 *	0.747 ± 0.01 *
	Q210S	-7.7 ± 0.3 *	0.735 ± 0.03 *
	G224S	4.9 ± 0.8 *	1.21 ± 0.2 *
	V269S	-18.5 ± 1.3 *	0.479 ± 0.03 *
	S136A	-2.8 ± 1.0	0.895 ± 0.27
K^+	WT	-27.9 ± 0.5	0.330 ± 0.006
	C87S	-31.5 ± 0.3 *	0.286 ± 0.001 *
	G181S	-31.8 ± 0.9 *	0.283 ± 0.008 *
	Q210S	-16.0 ± 0.3 *	0.528 ± 0.02 *
	G224S	-14.2 ± 0.1 *	0.569 ± 0.005 *
	V269S	-43.3 ± 1.3 *	0.179 ± 0.005 *
	S136A	-12.5 ± 1.1 *	0.609 ± 0.02 *
Rb^+	WT	-29.2 ± 0.4	0.314 ± 0.004
	C87S	-47.4 ± 1.1 *	0.153 ± 0.003 *
	G181S	-41.6 ± 0.1 *	0.192 ± 0.001 *
	Q210S	-35.5 ± 1.2 *	0.245 ± 0.008 *
	G224S	-22.9 ± 0.5 *	0.403 ± 0.009 *
	V269S	-52.3 ± 1.4 *	0.125 ± 0.003 *
	S136A	-25.7 ± 1.0 *	0.360 ± 0.007 *
Cs^+	WT	-16.9 ± 0.8	0.511 ± 0.02
	C87S	-26.8 ± 0.3 *	0.345 ± 0.001 *
	G181S	-35.8 ± 0.7 *	0.241 ± 0.005*
	Q210S	-32.0 ± 0.7 *	0.281 ± 0.006 *
	G224S	-20.8 ± 0.7 *	0.438 ± 0.01 *
	V269S	-54.1 ± 1.0 *	0.117 ± 0.002 *
	S136A	-17.5 ± 1.4	0.498 ± 0.01

Table 2.3.1 – Shifts in reversal potential and permeability ratio comparison
Changes in reversal potential were calculated by subtracting E_{rev} in cation X^+ from E_{rev} in Na^+ (mean ± S.E.M; n = 7-25). Permeability ratios were calculated using changes in reversal potential. Values are reported as mean ± S.E.M (n = 7-25). For significance testing, mutant ChR2 values were compared to WT in the same solution. Statistically significant values are denoted by a * ($P < 0.001$).

We measured kinetics and steady-state to peak current ratios (I_{ss}/I_p) to determine the effect of single serine mutations on the ChR2 photocycle. Current traces were fit in Na^+ solution from the dark to peak region for on rates (τ_{on}), the peak to steady-state region for decay rates (τ_{decay}), and the steady state to dark region for closing rates (τ_{off}) (Figure 2.3.2A). Additionally,

opening and decay rates were fit at -120 mV to ensure ChR2 was fully recovered. WT ChR2 had an off rate of 12.1 ± 0.3 ms (-60 mV), on rate of 4.6 ± 0.2 ms, and decay rate of 122 ± 5 ms (n = 16) (Figure 2.3.2B and C). Each mutant ChR2 had similar results for channel closing except for G224S, which showed a two-fold slow-down in channel closing (27.0 ± 0.8 ms; n = 14; -60 mV) (Figure 2.3.2B). Decay rates for ChR2 mutants demonstrated a similar trend with the off rates (Figure 2.3.2C). Only G224S was slower with a decay rate of 175 ± 8 ms (n = 14). Single serine ChR2 on rates were statistically significant when compared to wild-type, except for C87S which had no change. G224S had the largest change in on rate with τ_{on} = 10.3 ± 0.8 ms (n = 14). Q210S also showed a slight slowdown with τ_{on} = 5.5 ± 0.1 ms (n = 8) (Figure 2.3.2C). G181S and V269S had τ_{on} values of 5.4 ± 0.2 ms and 5.6 ± 0.3 ms, respectively. Our kinetic data show that only G224S exhibited a global effect on the ChR2 photocycle and that several ChR2 mutants selectively increased the opening channel kinetics.

Steady-state to peak current ratios were also calculated for each mutant ChR2. Ratios were calculated in Li^+, Na^+, and K^+ solutions by normalizing current traces at -120 mV to -1 μA. I_{ss}/I_p ratios are used as a measure of inactivation of the channel during prolonged light exposure. Additionally, because monovalent cation selectivity decreases in tandem with an increase in proton selectivity during the steady state, these ratios can be used to infer increased cation selectivity in the absence of protons (pH = 9) (14). G181S had larger ratios when compared to WT in the same solution, which indicated less inactivation as ChR2 transitions to the O2 state (Figure 2.1.1A and Figure 2.3.3). Other ChR2 mutants had no significant difference or a change of I_{ss}/I_p in only one solution (Figure 2.3.2C).

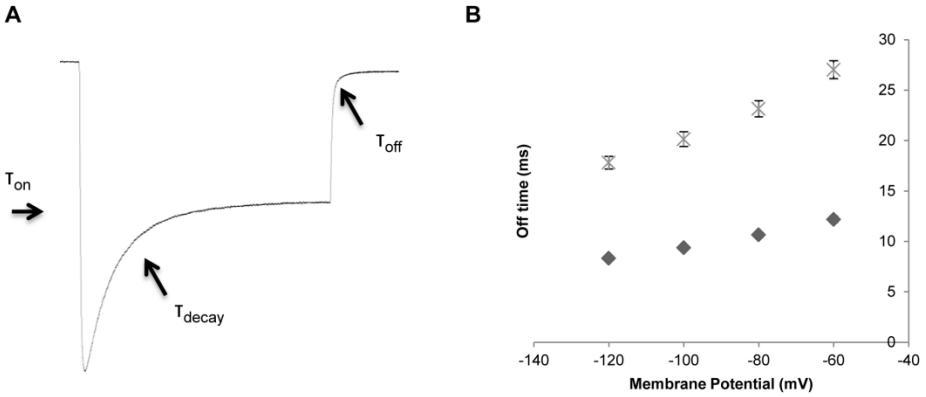

C

Construct	τ_{on} ± SE (ms)	τ_{decay} (ms)	τ_{off} (ms)	I_{ss}/I_p
WT	4.6 ± 0.2 (16)	122 ± 5 (16)	12.1 ± 0.3 (16)	0.46 ± 0.02 (16)
C87S	4.3 ± 0.2 (23)	110 ± 4 (23)	11.1 ± 0.2 (23)*	0.50 ± 0.01 (23)
G181S	5.4 ± 0.2 (14)*	117 ± 3 (14)	11.2 ± 0.3 (14)	0.63 ± 0.01 (14)*
Q210S	5.5 ± 0.1 (8)*	135 ± 6 (11)	13.0 ± 0.3 (8)	0.41 ± 0.02 (8)
G224S	10.3 ± 0.5 (14)*	175 ± 8 (14)*	27.0 ± 0.8 (14)*	0.44 ± 0.01 (14)
V269S	5.6 ± 0.3 (12)*	133 ± 6 (13)	13.2 ± 0.5 (13)	0.54 ± 0.01 (12)*

Figure 2.3.2 – Kinetic parameters for single serine mutants

Kinetic values were obtained by fitting ChR2 photocurrents to exponential equations. All parameters were calculated in 115 mM Na^+ solution at pH 9. For on and decay times, traces were fit at -120 mV to ensure ChR2 was in the dark adapted state. Values reported as mean ± S.E.M (n = 8-23). Significant differences are marked with a * ($P < 0.05$). (A) Summary of photocurrent exponential fits. (B) Off rate comparison of the slow G224S mutant versus WT at different membrane potentials. The off rate of ChR2 had a strong dependence on the holding potential of the cell. Diamond, WT; crossed X, G224S. All values were statistically significant (as described in C) (C) Summary of kinetic parameters and inactivation ratios for single serine ChR2 mutants. Values are reported as mean ± S.E.M (n = 8-23). Statistically significant values are denoted by a * ($P < 0.05$).

To determine whether introducing serine residues into the transmembrane domain of ChR2 facilitates inter- and intrahelical hydrogen-bonding, we estimated the minimum pore diameter of each construct. We applied excluded volume theory using our calculated permeability ratios to estimate the narrowest region of the channel. The permeability of an ion permeating the channel is proportional to the region that is left unoccupied by the ion in the pore

(97, 102, 103). Thus, the diameter of the narrowest region of the pore can be determined by plotting the square root of permeability ratios P_x/P_{Na} versus ionic radii. Values of the y-intercept, a, and slope, b, were obtained by fitting the data with a linear regression (Figure 2.3.4). Fitting the square root of WT permeability ratios to a linear regression afforded values of 1.37 and -0.44 for a and b, respectively with an R^2 value of 0.73. R^2 values were consistent with previously published pore size calculations (102). According to equation 1a, the minimum pore diameter for WT ChR2 was 6.22 Å, in good agreement with the previously described estimates. Single serine mutations had calculated minimum pore sizes smaller than that of WT ChR2, ranging from 4.62 Å to 5.74 Å (Figure 2.3.4B) excluding G224S, which had a pore size of 6.02 Å. The largest change in pore diameter was seen for V269S which had a pore size of 4.62 Å. The change in pore size was consistent with our permeability calculations for this mutant ChR2, where all cations had decreased P_x/P_{Na}. Calculating (1-a)/b (Equations 1b and 1c) gives the radius of a sodium ion permeating the channel. The value obtained for WT was 0.84 Å (Figure 2.3.4B). Calculated sodium radii were found to have ~15% error compared to the dehydrated radius of sodium (0.98 Å) and within reason compared to previously published reports (97, 102, 104).

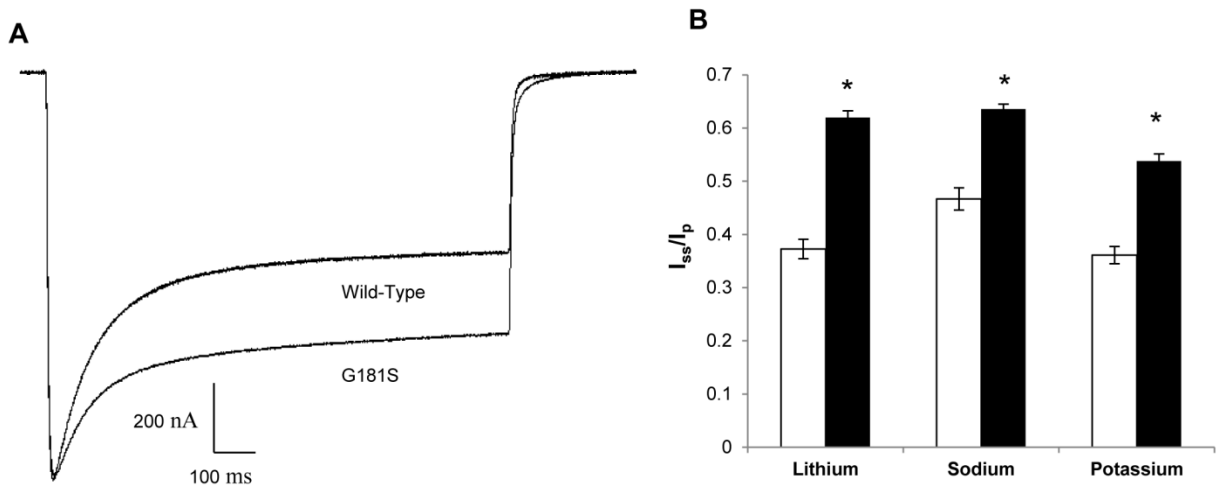

Figure 2.3.3 – Steady-state to peak current ratio comparison for G181S

. Ratios were calculated after normalization to -1 μA at -120 mV in cationic solutions (115 mM XCl, 2 mM $BaCl_2$, 1 mM $MgCl_2$, Tris; pH 9; n = 14-18). Significant differences are marked with a * ($P < 0.05$). (A) Comparison of WT and G181S photocurrents in Na^+ solution. (B) I_{ss}/I_p comparison for WT and G181S in different cationic solutions. Wild-type ChR2 is colored white while G181S is colored black.

Lastly, we replaced an endogenous serine residue located at position 136 with alanine in order to remove an inter- or intrahelical hydrogen bond. We hypothesized that this would cause an opposite effect on ChR2 by increasing the pore diameter. Using permeability ratios (Table 2.3.1) and applying excluded volume theory, we determined the minimum pore diameter to be 7.04 Å with an estimated sodium radius of 0.86 Å (Figure 2.3.4). Removal of S136 provides further evidence that introduction of transmembrane serine residues constrict the pore diameter through inter- or intrahelical hydrogen bonds.

A

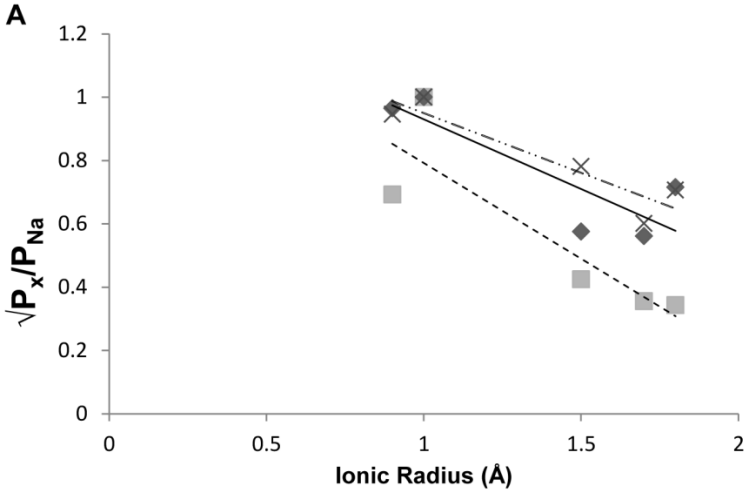

B

Construct	a	b	R^2	Pore Size (Å)	Na^+ Radius (Å)
WT	1.37	-0.44	0.73	6.22	0.84
C87S	1.50	-0.59	0.82	5.10	0.85
G181S	1.46	-0.57	0.88	5.07	0.79
Q210S	1.39	-0.48	0.85	5.74	0.80
G224S	1.53	-0.50	0.97	6.05	1.04
V269S	1.39	-0.60	0.76	4.62	0.65
S136A	1.32	-0.37	0.86	7.04	0.86

Figure 2.3.4 - Relationship of relative permeability and alkali ionic radii for ChR2 serine mutations

Relative permeability ratios were calculated using reversal potentials for each mutant. (A) Plotting the square root of relative permeability ratios vs. ionic radius yielded a linear fit for each data set. Solid line/diamond, WT; dashed line/square, V269S; broken line/X S136A. For all mutants, the larger alkali metal ions (K^+, Rb^+, and Cs^+) were less permeable than the smaller alkali metal ions (Li^+, Na^+). These results were consistent with excluded volume theory [36]. (B) Minimum pore fitting parameters and pore size calcualtions for single serine ChR2 mutants and S136A. The coefficients a and b correspond to the y-intercept and slope of the fitted data, respectively.

2.4 Discussion

A sequence analysis of bR and ChR2 indicates ChR2 lacks eight transmembrane serine residues present in bR. Considering that serine residues within transmembrane domains contribute to inter- and intrahelical hydrogen-bonding, we hypothesized that the lack of these serine residues were an important contributor to the molecular determinants that define ChR2

function. By reintroducing the eight transmembrane serine residues present in bR at homologous positions in ChR2, we have shown that the pore size is decreased. Also, replacement of S136 with alanine increased the pore diameter. An analysis of the crystal structure of the channelrhodopsin chimera C1C2 (PDB entry: 3UG9) indicates that some serine mutations have the potential to form hydrogen-bonds with residues on opposite helices or with the carbonyl backbone. Serine residues were inserted into the crystal structure using the mutator plugin for VMD.

Three ChR2 mutants, I197S, P234S, and M255S, showed little ion conductance upon activation with light. The expression of both I197S and M255S were similar to WT, suggesting that these two mutations cause decreased function. In contrast, the P234S had highly reduced expression compared to WT. The reduced photocurrent is therefore a consequence of expression and not an alteration to the channel.

The most drastic change in pore diameter was observed for the V269S mutant, which had permeability ratios smaller than WT ChR2. V269S resides on the intracellular end of TM 7 near the transmembrane and intracellular interface. This helix extends past the membrane ~18 Å into the cytosol (33). The closest hydrogen-bonding acceptor is E273, where the carboxylate ion is ~3.78 Å away from the hydroxyl proton on V269S. V269S is also in close proximity to the intracellular ends of TM1 and TM2, but the structure is unresolved at the residues of interest (residues 80-88). Homology modeling of ChR2 suggests that V269 is embedded into the lipid bilayer. By introducing a polar residue at this position, an energetic cost would be incurred. Additionally, it has been previously shown for the M intermediate in bR that S226 (V269S in ChR2) moves ~2 Å closer to L100 (T139 in ChR2) (105). We suggest that introducing a polar

residue at this position destabilizes the protein-lipid interface and results in moving TM 7 inward and reducing the pore size.

The C87S and G181S mutants also had large reductions in pore size (5.10 Å and 5.07 Å, respectively). G181S is located next to the β-ionone ring of the retinal moiety (~2.36 Å), but has no effect on the kinetics of the photocycle. However, G181S is 2.08 Å from the backbone carbonyl of T159 and 3.61 Å from the hydroxyl group of T159, which provides two possible hydrogen-bonding sites. This threonine residue has been shown to form part of the retinal binding pocket where it is important for photocycle kinetics, magnitude of photocurrent, and the light intensity required for activation (106) [48]. Furthermore, we observed an increase in steady-state to peak current ratios for G181S under continuous light conditions, which suggests that this residue has an indirect effect on ChR2 inactivation. This is most likely a result of an interaction with T159. The C87S mutant has one possible interaction with the backbone carbonyl of S63 at a distance of ~2.32 Å. This region of the pore is constricted through hydrogen-bonding of S63, E90 and N258. The introduction of a hydrogen-bond with C87S would further constrict this region by coupling TM1 and TM2. Interestingly, cysteine residues also have the propensity toward forming hydrogen-bonds similar to serine in membrane protein structures, but is weaker than typical oxygen/nitrogen mediated hydrogen-bonds (107).

Both Q210S and G224S had small changes in the pore diameter. Analysis of the channelrhodopsin chimera crystal structure suggests that Q210S is oriented toward the lipid bilayer where it has no potential for hydrogen bonding to the channel backbone. This explains why only a small change in pore diameter was observed for this mutation. Lastly, G224S had nearly no change in pore diameter compared to WT ChR2. The side chain, similar to Q210S, is oriented into the bilayer. There is potential for a hydrogen-bond to be formed to the carbonyl of

F220, although the distance is 3.91 Å; above the average for this type of interaction. The changes in kinetics may be explained by having a glycine at this position in the wild-type. G224 could facilitate a favorable helix-helix interaction during the photocycle. Addition of a hydrogen-bond would remove this interaction but the added rigidity of the protein would cause slower kinetics and a pore diameter consistent with the phenotype.

To further test our hypothesis that serine residues play an important role in the conformational flexibility of ChR2, we replaced a serine at position 136 with alanine. The results from experiments with S136A indicated a pore size larger than that of WT ChR2, which was the opposite effect that we observed when introducing serine residues into the transmembrane domain. S136 resides on TM4, approximately 3.2 Å away from T149 on TM5, which provides a potential hydrogen bonding site. Mutation of S136 to alanine would remove this interaction and thus allow for pore expansion. These results suggest that the reduced pore diameter of single serine ChR2 mutants is caused by the introduction of a serine mediated hydrogen-bond.

We calculated permeability ratios for the five single serine insertions and a single serine removal as a measure of channel selectivity to further support the notion that introduction of hydrogen-bonds would restrict the conformational flexibility of the channel. In general, ChR2 mutants that decreased the size of the pore had reduced relative permeability ratios for alkali metals. The V269S mutant had the largest effect on permeability, which was expected because of the large change in pore diameter. C87S, G181S, and Q210S had permeability ratios smaller than wild type for most ions, but larger than V269S. G181S also was the only mutant ChR2 that had a change in steady-state to peak current ratios compared to WT ChR2. An analysis of our experimental results suggest that the size selectivity filter is not restricted to any specific location

within the transmembrane domain, as these residues are located on different helices either at the intracellular end or near the retinal binding pocket. Furthermore, the G224S mutant was the only construct that had a change in the apparent kinetic parameters of the channel. The slowdown in kinetics we observed was a global effect which persisted throughout the entire conducting state. Excluding G224S, serine mutants had little effect on apparent channel kinetics. This suggests that pore constriction is not a result of a global change in the protein, but rather a local effect arising from the introduction of a strong hydrogen bond donor.

Calculation of the pore size can be determined both empirically and computationally (97, 108). Our approach used excluded volume theory, which has general applicability to the translocation of hydrated and dehydrated cations (98, 103). This method has been well established for accurate estimations of the minimum pore size for ion permeation. It is important to note that pore calculations are determined using relative permeability ratios. Therefore, it is possible to see a net decrease in the permeability of all cations with no change in pore diameter. Likewise, a proportional increase in cation permeability would result in no change in pore size. An example of this is the G224S mutant.

Recently, Nack *et al.* reported that 0.3 H^+/ChR2 are pumped during the photocycle, a contribution that we have not taken into account for pore size estimations (55). However, the amount of protons pumped during the photocycle is small in comparison to the amount of ions flowing through the channel. Therefore, we believe that the proton pumping ability of ChR2 has a negligible effect on the pore size calculations.

In summary, the recently elucidated crystal structure of the chimeric channelrhodopsin protein (C1C2) exhibited a large pore lining surface on the extracellular side of C1C2 (33). The putative conducting pathway forms between transmembranes 1, 2, 3, and 7 and is lined with negatively

charged residues. Our results suggest that the size selectivity filter is located further along the channel and at multiple points along the conductance pathway (Figure 2.1.1B). Furthermore, evidence has been presented that residues located adjacent to the retinal binding pocket, along the intracellular side of the protein, and an interaction between TM1 and TM2 all affect the permeability of ChR2. Thus, residues that are located on the cytoplasmic side of the channel are determinants of ion conductance. We also suggest that the high affinity for serine residues to form inter- and intrahelical hydrogen bonds is the cause for reduction in pore size, decrease in permeability ratios, and slowdown of kinetics. The channel activity of ChR2 appears to be a direct consequence of its ability to undergo large conformational changes in the backbone structure for pore formation.

3 Cysteine substitution and labeling provides insight into channelrhodopsin-2 ion conductance

3.1 Introduction

The ion permeation pathway in membrane channels is an important determinant for channel function and selectivity. Elucidating residues which line the conducting pathway provides mechanistic understanding of secondary structure, how selectivity is determined, and where binding sites are located. Cysteine residues provide a modifiable platform in which protein structure-function can be explored. The free sulfhydral group can be modified by a variety of chemical probes and allows for site-specific labeling. This technique has been used to reveal the pore lining regions and gating mechanisms in the cystic fibrosis transmembrane conductance regulator (CFTR), P2X receptors, sodium channels, and the nicotinic acetylcholine receptor (nAChR) (109-112). One class of cysteine labeling compounds are methane thiosulfonate reagents (MTS). Several MTS derivatives have been synthesized so that a permanent negative or positive charge can be introduced to the protein (111). MTS reagents are water soluble and undergo nucleophilic attack from free cysteine sulfhydral groups to form a new disulfide bridge (Figure 3.1.1). Three MTS derivatives ($MTSES^-$, $MTSEA^+$, MTSET) are ~ 6 Å in diameter, lipophilic, and can be used to determine regions of water accessibility in the closed or open conformation of a channel. Site-specific cysteine replacement followed by MTS labeling is a powerful tool to elucidate channel selectivity and the conductance pathway.

The molecular determinants which contribute to ion permeation in ChR2 remain unresolved. Analysis of EPR and FTIR experiments has greatly improved our understanding of the early stages of pore formation (27, 94, 113, 114). Elucidation of the crystal structure of the ChR variant C1C2, which includes transmembrane (TM) domain 1-5 of ChR1 and TM6-7 of ChR2 has provided a scaffold to investigate the molecular mechanism of ChR2 function(33). Inspection of this crystal structure shows that the extracellular side of the protein contains a large

water-filled electronegative vestibule, which includes TM1, TM2, TM3 and TM7. Analysis of cysteine scanning experiments has shown that residues on the extracellular side of TM3 contribute to the cation permeation pathway of ChR2(61). This vestibule is closed further down the pore by an occlusion site comprised of hydrogen-bonding between S63, E90, and N258. A second occlusion site is found at Y70 on the intracellular side. A charged residue on TM2 (E90) is crucial for proper cation flux and likely contributes to cation gating (58, 113). Charge inversion of E90 to lysine turns ChR2 into a Cl^- channel (60, 115).

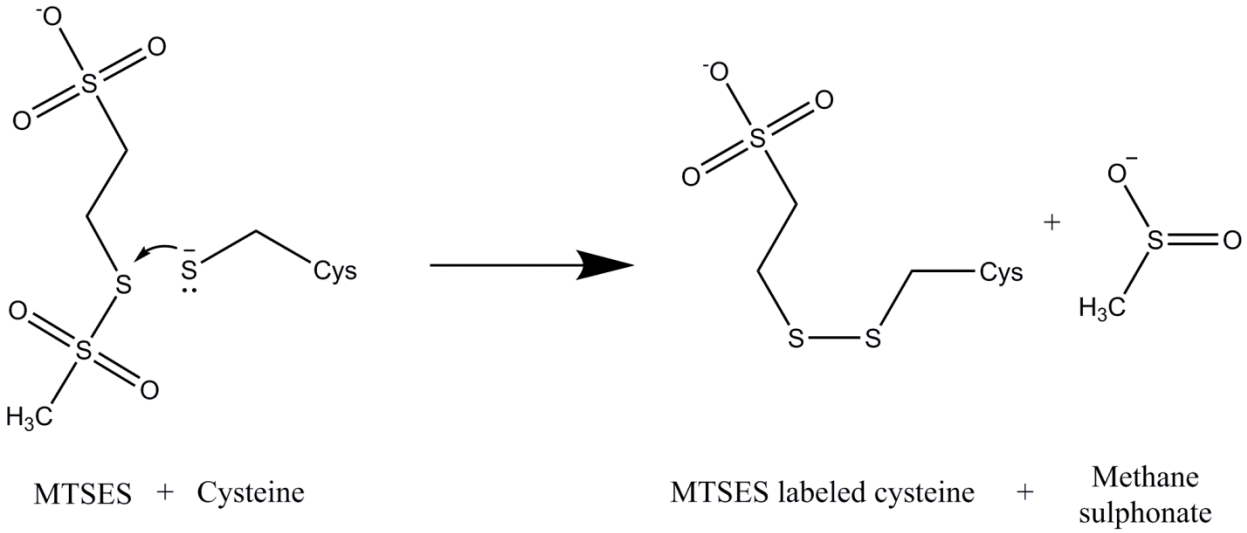

Figure 3.1.1 – Reaction scheme for cysteine specific labeling
Cysteine residues that are water accessible are labeled by MTSES at physiological pH. Nucleophilic attack occurs at the alkylthio group on the MTS reagent forming a disulfide bridge and the bi product methane sulphonate.

While inspection of the C1C2 chimera crystal structure has revealed that TM7 forms part of the extracellular electronegative pore, the contribution of TM7 to the permeation pathway of ChR2 is unresolved. Therefore, we performed cysteine scanning mutagenesis and 2-sulfonatoethyl methanethiosulfonate ($MTSES^-$) labeling on residues which comprise TM7 preceding K257 to elucidate the role of TM7 in ion permeation and accessibility. MTSES labeling introduces a negative charge upon site-specific labeling (Figure 3.1.1). The ability to

site-specifically introduce charge is a powerful tool to identify the contribution of specific residues to the permeation pathway of ion channels(111). We compared photocurrents and kinetics between wild-type (WT) ChR2 and constructs which contained single cysteine replacements within TM 7. Analysis of our experimental results reveals that residues on TM 7 that orient toward TM 1 and 2 serve to funnel cations into the pore.

3.2 Materials and Methods

3.2.1 Molecular Biology

The cDNA of ChR2 (1-309) with a C-terminal hemagluttanin tag (YPYDVPDYA) was cloned into the vector pTLN. ChR2 single cysteine constructs were created using the Stratagene Quikchange kit. Synthesis of mRNA was carried out using the SP6 mMessage mMachine (Ambion).

3.2.2 Oocyte preparation and microinjection

Oocytes were extracted by partial ovarectomy of Xenopus laevis female frogs. Oocytes were digested in filtered Oocyte Ringer's Buffer without Ca^{2+} (ORI-; 90 mM NaCl, 2 mM KCl, 5 mM MOPS; pH 7.4) containing 3.0 mg/mL type II collagenase. After digestion, the cells were washed in copious amount of ORI+ (ORI- with 2 mM $CaCl_2$) and stored in ORI+ buffer supplemented with 1 mg/mL gentamycin. One day after digestion, oocytes were manually injected with 50 ng of ChR2 mRNA in DEPC-treated water using a Nanoject II Auto-Nanoliter Injector (Drummond Scientific). Post injection, oocytes were stored in ORI+ buffer with 1 mg/mL gentamycin and 1.5 uM all-trans retinal for 3 days in the dark at 17^{o}C.

3.2.3 Electrophysiology and data analysis

Glass microelectrode holders were pulled using a PC-12 pipette puller (Narishige), filled with 3 M KCl and had tip resistances of 0.5-2.0 MΩ. The reference and ground electrodes were

connected to the oocyte chamber via agar bridges filled with 3 M KCl. Oocytes were clamped using a Turbo-tec-03X amplifier connected to pClamp software through an Axon 1440A digitizer. All voltage protocols were controlled with Clampex software. ChR2 activation was achieved using a Omicron LEDMOD V2 300 mW LED at 470 nm. Voltage protocols were carried out from -120 to +60 mV in 20 mV steps with 1.5 s of ChR2 activation. A 10 s recovery period was introduced between each voltage step. All experiments were carried out in MTS(-) buffer (115 mM NaCl, 10 mM HEPES, 2 mM $BaCl_2$, 1 mM $MgCl_2$, pH 7.5). During the wait period, cells were washed in either MTS(-) or MTS(+) (MTS(-) buffer supplemented with 1 mM (2-ethylsulfanato)-methanethiosulfonate. Data analysis was carried out using Clampfit software. Kinetic parameters were determined by monoexponential fitting of the peak to stationary current transition (τ_{decay}) or bi-exponential fitting of the stationary to off current transition (τ_{off}). Percent recovery was determined by the ratio of $\Delta I_2/\Delta I_1$ where $\Delta I_2 = I_{p2} - I_{s2}$ and $\Delta I_1 = I_{p1} - I_{s1}$. The numbers correspond to the initial currents (1) and current after the 7 minute wait period (2).

3.2.4 Channelrhodopsin-2 modeling

A model of channelrhodopsin-2 was created using the crystal structure of the channelrhodopsin chimera C1C2 as a template (PDB: 3ug9) (33). The ChR2 sequence (residues 1-308) were built on C1C2 using the SWISS-MODEL database after a sequence alignment (116-118). Retinal coordinates were taken from C1C2 and merged with our model of ChR2. The topology file of retinal was constructed using the molefacture plugin for VMD and atomic charges were used from previously published results (119). The parameter file for retinal was taken from the literature (120-124). A protein structure file was then created using the autopsf builder in VMD with LINK patches applied to residues 256 and 258 to incorporate retinal into

the structure. The titratable residues D253, E123 and E90 were left deprotonated during simulations (29, 62).

The ChR2 model was embedded into a 1-palmitoyl-2-oleoyl-sn-glycero-3-phosphocholine (POPC) lipid membrane (80 x 80 A) and solvated in TIP3 water. The system was ionized in 115 mM NaCl. The entire system consisted of 51,972 atoms.

3.2.5 Molecular Dynamics

All simulations were carried out using NAMD 2.7 at 293 K using constant number, pressure, and temperature (NPT) in addition to periodic boundary conditions (125). Constant temperature and pressure were maintained by utilizing Langevin damping and Langevin piston dynamics. Full-system electrostatics were treated using particle mesh Ewald forces. Short-range van der Waals interactions had a 12 Å cutoff and a switching function at 10 Å. The CHARMM 27 force-field was used for all MD simulations with 1 fs time-steps (126, 127). Initially, a 500 ps minimization was performed to melt lipid tail groups while water and protein remained fixed. Minimization was then continued for a second 500 ps simulation in which water was released. Lastly, a 10 ns equilibration with the entire system released was performed. This resulted in an equilibrated structure indicated by a constant RMSD of 2 Å (Figure 3.3.5). A Ramachandran plot was also created to validate that the backbone dihedrals were within the allowable theoretical limits.

3.3 Results

Cysteine replacement at H249, D253, L254, and S256 resulted in ChR2 proteins which had photocurrents less than 40 nA. This could be due to non-functional protein or protein which did not traffic to the plasma membrane. As a result of low photocurrents, these mutants were not analyzed further. Cysteine replacement at position I252 resulted in significantly greater I_P and I_S photocurrents when compared to ChR2. In contrast, cysteine replacement at positions V242,

Y243, G244, S245, T246, G248, and T250 demonstrated significantly smaller I_P and I_S photocurrents when compared to WT ChR2 (Figure 3.3.1).

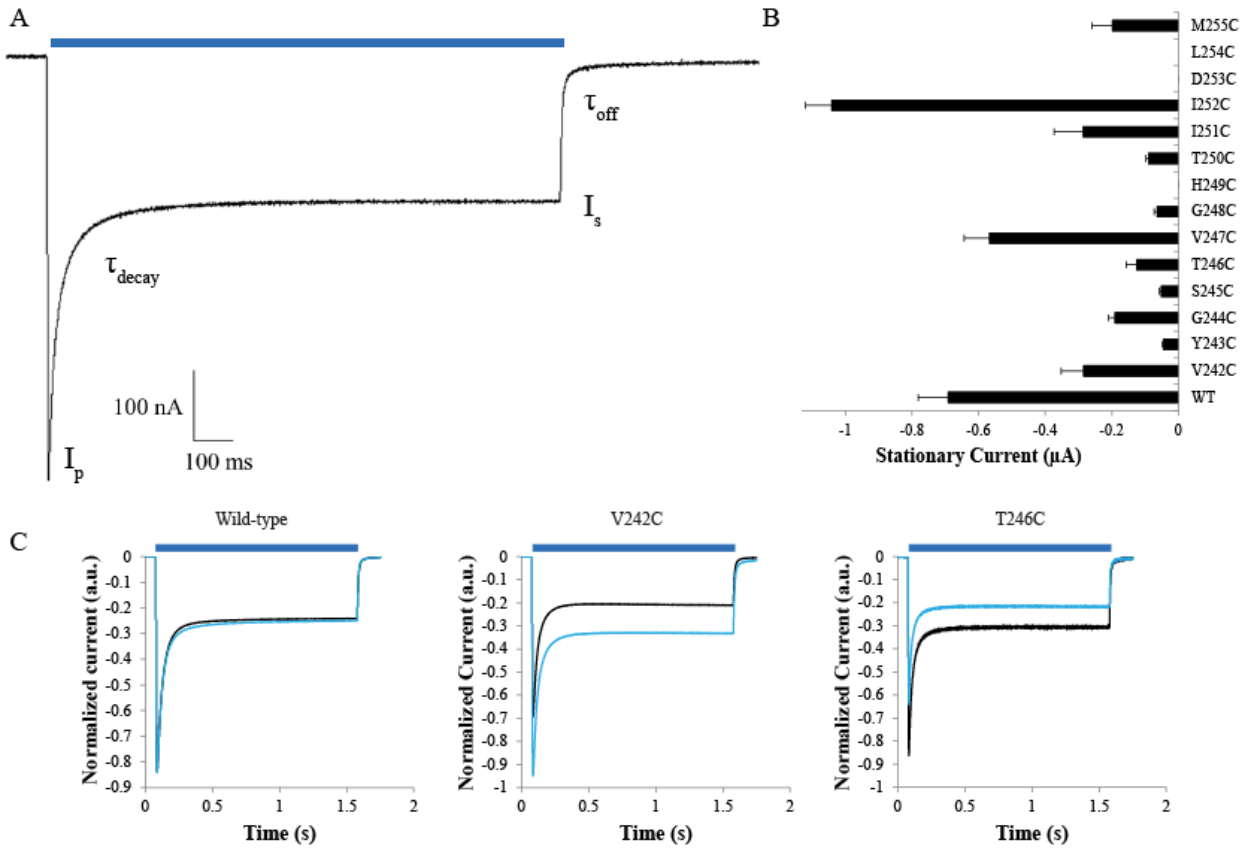

Figure 3.3.1 - ChR2 photocurrent response

(A) Typical ChR2 photocurrent under voltage clamp conditions (V_m = -120 mV in MTS(-) buffer). Black bar indicates 470 nm light application, I_p indicates peak current, and I_s indicates stationary current. (B) Average stationary photocurrents from cysteine constructs. Error bars indicate SEM (n = 6-16). (C) Representative differences in photocurrent response between the unlabeled wait control (black) and MTSES (1 mM) labeled cells (blue) at V_m = -120 mV. Photocurrents were normalized to the unlabeled control cell.

ChR2 I_P undergoes rundown upon repeated photostimuli, a process referred to as desensitization (5). This intrinsic property of ChR2 required a more nuanced protocol to quantify whether MTSES labeling altered ChR2 photocurrents: First, light was applied to oocytes expressing ChR2 at membrane potentials (V_m) of -120 to +60 mV in 20 mV steps (negative

control). Following a wait time of seven minutes, a second stimulus at -120 to +60 mV was applied. During the wait time, oocytes were labeled with MTSES in MTS(+) buffer or washed in MTS(-) buffer to serve as a positive control. Photocurrents from the second stimulus were normalized to the first stimulus. The normalized unlabeled (- MTSES) and labeled (+ MTSES) photocurrents were then compared as a percent difference to determine the effect of labeling (Figure 3.3.2). We used this approach as the recovery of the transient peak response for the WT ChR2 was variable between batches of oocytes expressing ChR2 (109).

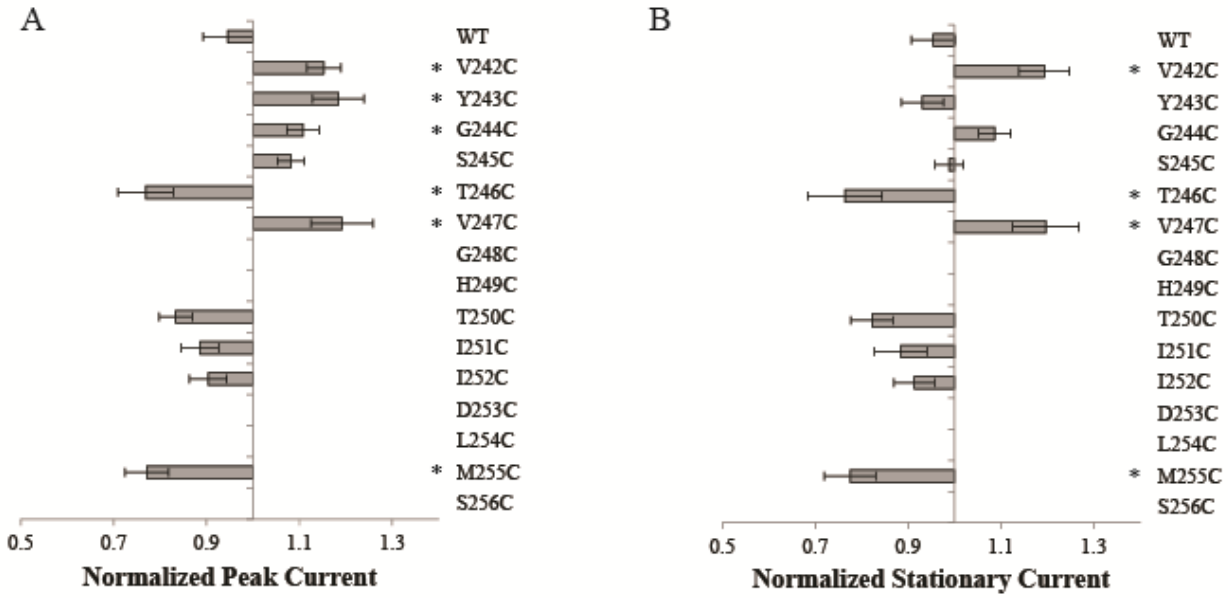

Figure 3.3.2 – Effect of MTSES labeling on ChR2 cysteine constructs
Normalized I_P (A) and I_S (B) photocurrent responses following labeling of ChR2 mutants. V_m = -120 mV; n=3-11). *$p < 0.05$. Error bars indicate SEM. Data in A and B are displayed as a percentage of the control.

There are nine native cysteine residues in ChR2. No functional effect following MTSES labeling with WT ChR2 was observed. For most functional cysteine mutants, MTSES labeling had no effect on the I_P or I_S amplitude when compared to WT at V_m = -120 mV (Figure 3.3.2). No observed effect upon MTSES application could be the result of no MTSES labeling or no functional effect upon MTSES labeling. A significant increase in I_P upon labeling was observed

for V242C, Y243C, G244C, and V247C, while a significant decrease was observed for T246C and M255C. MTSES labeling induced an increase in I_S for V242C and V247C while resulting in a decrease in I_S for T246C and M255C. We also investigated I_s/I_p ratios and percent channel recovery upon MTSES labeling (Figure 3.3.3). I_s/I_p ratios represent channel inactivation from the high conducting O1 state to the low conducting O2 state during prolonged light exposure, an effect not observed under single turnover conditions. The largest effect on channel inactivation was seen at Y243C where the I_s/I_p ratio decreased from 0.36 ± 0.05 to 0.30 ± 0.01 upon MTSES labeling.

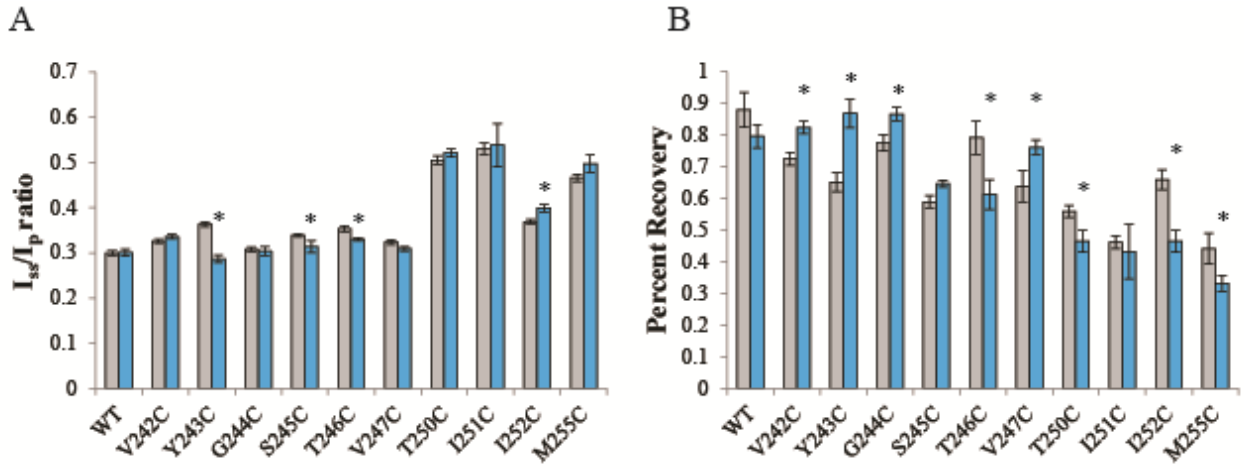

Figure 3.3.3 – ChR2 inactivation and recovery
(A) Steady-state to peak current ratios and (B) percent recovery of the 2nd photostimulus. Gray bars, unlabeled control; blue bars, MTSES labeled; Vm = -120 mV; n=3-11). *p < 0.05. Error bars indicate SEM..

Percent recovery gives insight into the efficiency of ChR2 recovering to the initial dark state. Recovery of MTSES labeled constructs was higher for V242C, Y243C G244C and V247C while it was lower for T246C, I252C, and M255C compared to the unlabeled wait control. Labeling of WT ChR2 had no effect on I_{ss}/I_p or recovery in the dark.

Photoactivation of ChR2 results in an initial transient peak current which decays rapidly to a steady state current under continuous illumination (Figure 3.1.1). Decay rates were fitted

with a mono-exponential function. Off rates were fitted with a bi-exponential function. Under prolonged light exposure, off kinetics are biphasic with a slow and fast component representing multiple decay processes. Although decay kinetics are voltage independent, off kinetics are dependent on the holding potential under our experimental conditions (Figure 3.3.4). Analysis of changes in response to photostimulus upon cysteine substitution provides information on channel gating. Cysteine replacement had a significant effect on the decay kinetics (from I_P to I_S) (Table 3.3.1). V242C and I252C resulted in accelerated decay kinetics while G244C, S245C, and T246C had slower decay rates (Table 3.3.1). Cysteine replacement had a significant effect on the off kinetics (from I_S to off) resulting in faster rates for V242C and T250C, but slower rates for G244C, S245C, T246C, V247C and I252C. Labeling with MTSES significantly increased τ_{decay} for T250C from 40.1 ± 4.6 ms to 29.6 ± 3.4 ms (n = 4). In contrast, τ_{off} was slower upon MTSES labeling for G244C and V247C (Table 3.3.1).

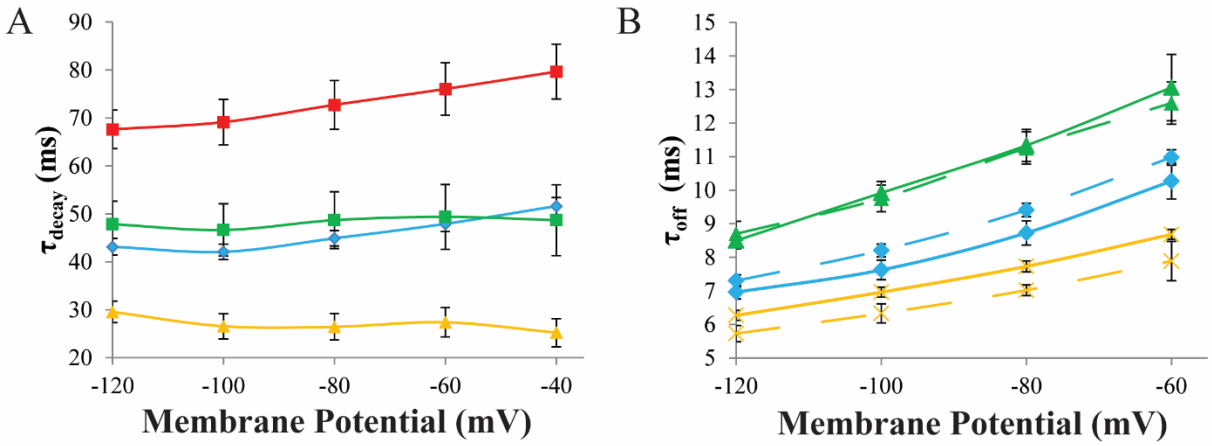

Figure 3.3.4 – Voltage dependency of kinetics
(A) Decay kinetics of WT ChR2 and select cysteine constructs. Blue – WT; green – V242C; red – I252C; yellow – V247C. (B) Off Kinetics comparison of unlabeled control and MTSES labeled cells. Same color scheme as in (B). Solid lines – unlabeled control; dashed lines – MTSES labeled. Error bars represent SEM (n = 6-16).

	Decay Kinetics (ms)		Off Kinetics (ms)	
	Unlabeled Control	**MTSES Labeled**	**Unlabeled Control**	**MTSES Labeled**
WT	43.1 ± 1.7	45.6 ± 3.1	7.3 ± 0.1	6.7 ± 0.2
V242C	47.8 ± 4.8	40.1 ± 2.7	8.7 ± 0.3*	8.5 ± 02
Y243C	33.2 ± 2.5*	29.3 ± 1.3	7.4 ± 0.2	7.1 ± 0.3
G244C	35.7 ± 1.1*	39.7 ± 2.2	6.6 ± 0.002*	6.8 ± 0.002**
S245C	24.5 ± 0.9*	25.3 ± 1.8	6.2 ± 0.1*	5.8 ± 0.1
T246C	29.5 ± 2.2*	26.5 ± 0.9	5.7 ±0.2*	5.6 ± 0.1
V247C	40.1 ± 2.2	37.2 ± 1.8	5.7 ± 0.1*	6.3 ±0.1**
T250C	40.1 ± 4.6	29.6 ±3.4**	8.6 ± 0.5*	8.4 ± 0.3
I251C	34.0 ± 3.1*	30.4 ± 1.8	6.2 ± 0.4	7.1 ± 0.4
I252C	67.6 ± 4.0*	70.1 ± 3.3	6.2 ± 0.2*	6.2 ± 0.1
M255C	37.3 ± 4.0	35.1 ± 2.4	6.6 ± 0.3	6.4 ± 0.1

Table 3.3.1 - Effect of cysteine replacement or MTSES labeling on decay and off kinetics of ChR2 photocurrents

Current traces were fit to a monoexponential or biexponential function for decay and off kinetics, respectively (Vm = -120 mV; n=5-11). *$p<0.05$ for unlabeled control compared to WT. **$p<0.05$ for MTSES labeled compared to the unlabeled control. Errors indicate SEM.

To spatially inspect the results of our experiments, we developed an equilibrated model of ChR2 based on the crystal structure of the channelrhodopsin chimera C1C2 (33). The ChR2 sequence was built on C1C2 using the SWISS-MODEL database following a sequence alignment (15, 116-118). When compared to C1C2, ChR2 has 76.3% identity and 91.7% similarity using the Waterman-Eggert scoring system (128). Our ChR2 homology model was inserted into a 1-palmitoyl-2-oleoyl-sn-glycero-3-phosphocholine (POPC) and the structure was equilibrated as described in the materials and methods. We calculated the RMSD of the model backbone structure over the course of a 10 ns equilibration (Figure 3.3.5A). The constant RMSD of ~2 Å was indicative of a stable structure. To further validate the structure, a Ramachandran plot was generated and revealed that residue dihedrals were within allowable limits (Figure 3.4.1B).

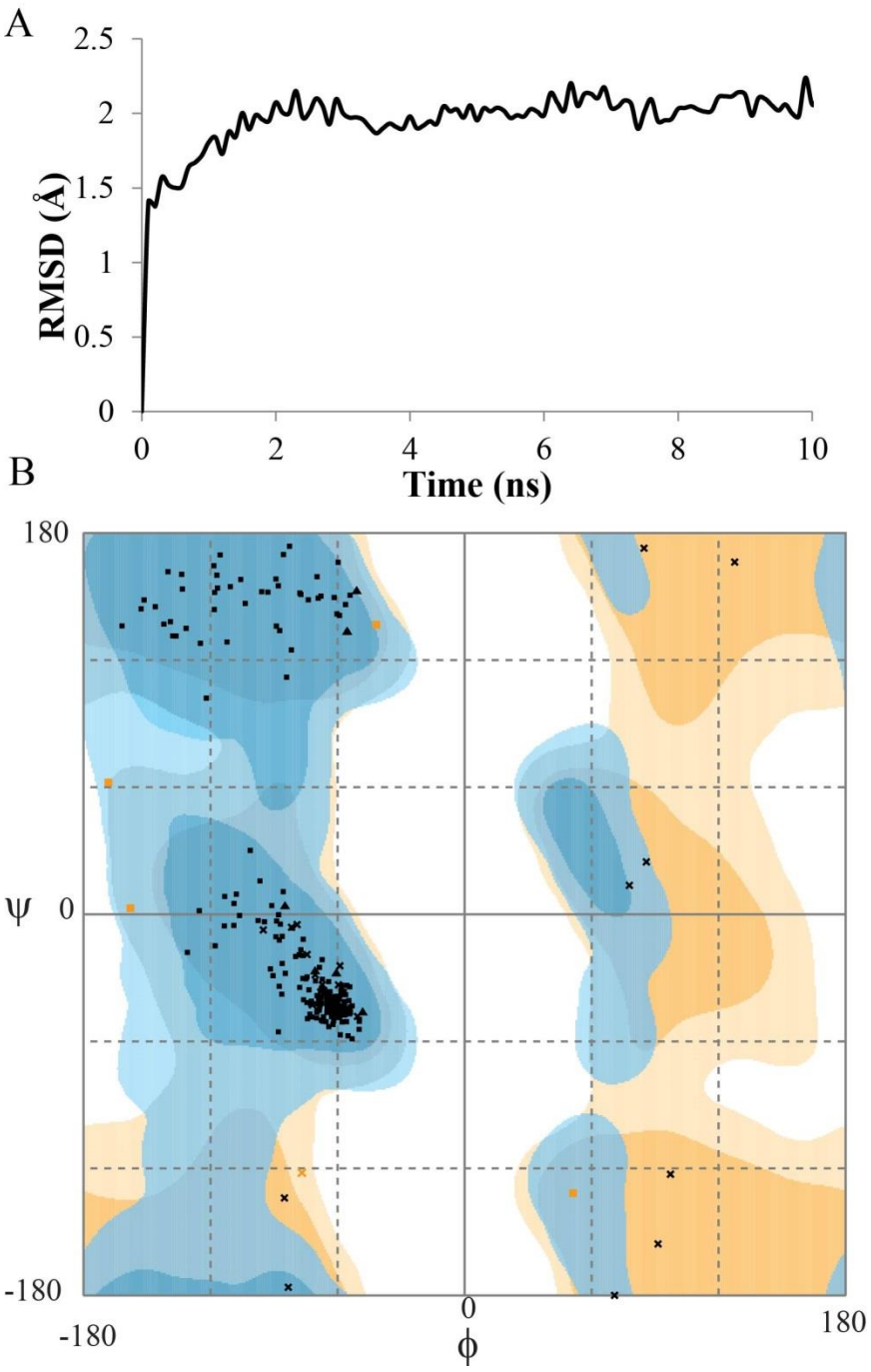

Figure 3.3.5 - Homology model equilibration results

(A) RMSD of ChR2 homology model after 10 ns equilibration excluding the N- and C-terminal tails. (B) Ramachandran plot of ChR2 homology model created using the RAMPAGE server (129)

3.4 Discussion

We monitored the effects that cysteine substitution and labeling had on ChR2 function. We found several cysteine substitutions on TM 7 resulting in little or no photocurrent response. Among these was D253, which has been identified as the internal proton acceptor for the Schiff base (27). Therefore it was not unexpected that mutation of this residue to cysteine would result in no photocurrent. Additionally, S256 is located directly above the Schiff base in the retinal binding pocket where mutation could alter the absorption maximum or change the geometry around retinal, explaining the lack of photocurrent. All four mutants that had minimal photocurrent (H249, D253, L254, and S256) are moderately conserved across known channelopsin proteins. While the function of D253 has been determined, the role of the remaining three residues is currently unknown. H249, L254, and S255 appear important for ChR2 expression and/or cation conductance.

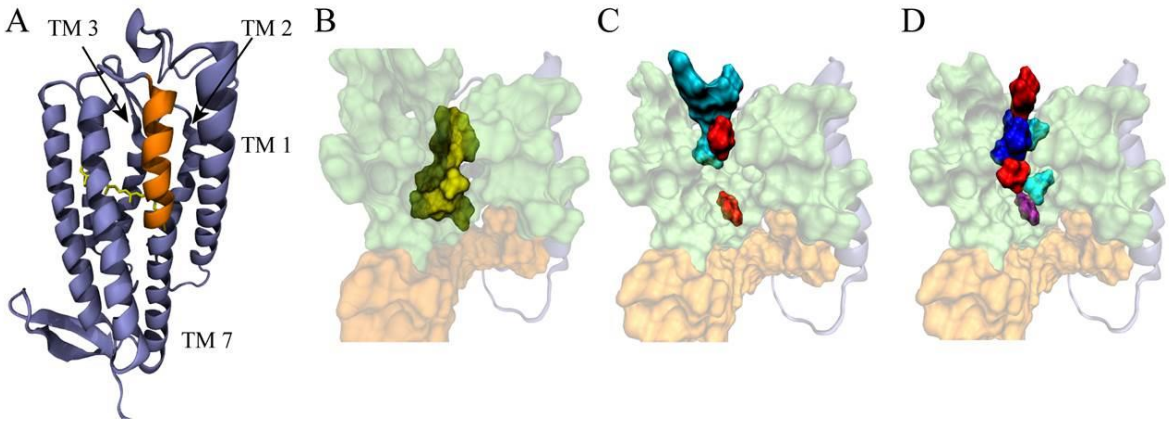

Figure 3.4.1 – Homology model of ChR2

(A) Equilibrated ChR2 structure with cysteine mutations colored orange and all-trans retinal highlighted in yellow. (B) Location of cysteine mutations which had no effect on ChR2function upon labeling or were non-functional/had low expression. (C) Location of residues which upon cysteine mutagenesis affected ion conductance. Mutations which had a significant increase of peak current upon MTSES labeling are shown in cyan while those which had a decrease are shown in red. (D) Location of residues which altered ChR2 kinetics upon cysteine replacement. Single cysteine mutants which affected decay kinetics only (purple), off kinetics only (red), or both (cyan) when compared to WT are shown. Residues which had a significant effect on kinetics upon labeling with MTSES are shown in blue. Images were created using Visual Molecular Dynamics Software.

Within the context of our homology model, residues which affected I_s and I_p were located at the interface of TM7 and TM1, with the exception of M255, which is oriented into the lipid bilayer (Figure 3.4.1). Our labeling results confirm that ChR2 must have an open extracellular cavity larger than 6 Å as MTSES reagents can label a residue (M255C) deep within the pore. Additionally, this indicates that even in the closed state, ChR2 is sufficiently flexible so that residues adjacent to another TM domain can be labeled. V242 and T246 are in close proximity to R115 and Q117 which were previously identified to affect ion conductance and permeability (61). Introducing a longer-chained negative charge at V242 or T246 may facilitate interhelical hydrogen bonding which enhances or reduces ion conductance, respectively. Placing a negative charge at the top of the vestibule, as with labeling of V242C, Y243C, G244C and V247C, may serve to increase cation access to the pore which results in an increase in I_P ion conductance

(130). Curiously, M255C had a detrimental effect to I_p and I_s, when labeled, but faces into the membrane. We have shown previously that mutation of M255 to a polar residue (M255S) results in highly reduced photocurrents (57). However, free cysteines behave similarly to hydrophobic residues which is evident by the modest photocurrents of M255C (131). This suggests that introduction of a negative charge with MTSES at this position disturbs the interaction between the membrane and TM7, resulting in severely reduced conductance.

Recovery of ChR2 after photostimulation is an important property to take into consideration for use in optogenetics to reliably spike action potentials. ChR2 recovery is dependent on the re-isomerization of retinal to the all-trans isomer and the reprotonation of E90, which is deprotonated during the photocycle (27). Accelerated recovery of ChR2 can be achieved by low external pH (5). Labeled cysteine constructs that increased recovery may be facilitated by funneling protons to the extracellular vestibule, increasing accessibility to E90. We propose the decrease in recovery for T246C, I252C, and M255C is likely caused by changing the electrostatic environment around E90 and the retinal binding pocket.

Cysteine substitution had a modest effect on inactivation (τ_{decay}) and closing (τ_{off}) kinetics compared to WT ChR2. However, only T250C had a significant decrease in τ_{decay} compared to the unlabeled control. Thus, the transition from O1 to O2 is accelerated in the presence of a negative charge or steric bulk at this position. We suggest that this position is crucial for stability between the two open states, but not for the conductance of ChR2. Similarly, V247C had change in closing kinetics upon MTSES labeling. These results suggest that channel gating is impaired in the presence of a negative charge or steric hindrance. Although V247C slows channel closing following labeling, it has increased recovery in the dark providing evidence that this is a separate process than channel closing.

Analysis of our experimental results indicates that the extracellular side of TM7 forms, in part, the permeation pathway for ChR2. Residues that are located near the extracellular interface had the largest effect on ion conductance, while those closer to the first occlusion site had no observable effect or were not accessible for labeling, with the exception of M255C. Compared to other opsin pumps, the backbone of ChR2 undergoes large conformational changes preceding conductance (24). This flexibility likely contributes to the accessibility of residues for labeling. As most of TM7 has little to no conservation we postulate that the diversity among residues in TM7 may contribute to the unique functionality and broad selectivity of ChR2 compared to other rhodopsins. Moreover, labeling of cysteine constructs in the extracellular vestibule with a negative charge likely causes a funneling effect to increase cation access to the permeation pathway.

4 Adjacent transmembrane residues regulate the two open states and progressive selectivity of channelrhodopsin-2

4.1 Introduction

The structure function relationship in membrane proteins is essential for determining how ions are transported into and out of the cell. Transport of molecules across the membrane is imperative to cellular function, and disruption of these processes has major implications in disease. Therefore, understanding the physical mechanisms of how membrane proteins selectively transport specific molecules is of biological significance. However, to resolve the fundamental properties of ion permeation and gating mechanisms, detailed structural information is required.

Molecular dynamic simulations (MD) are a powerful tool to study the conformational and structural dynamics of proteins. Combining MD with electrophysiological and other experimental techniques, the finer molecular details of channel structure and function can be elucidated. Unfortunately, due to the large number of atoms present in these systems, it is not possible to monitor conformational changes alongside transport processes with MD time-scales. This limitation can be overcome using steered molecular dynamics (SMD), which lowers the high energy barrier of an ion translocating across the membrane (132). SMD applies external forces to the system of interest which can be used to probe biological processes on time-scales suitable for MD simulations. Simulations utilizing SMD can be performed at constant velocity or constant force. A major drawback in using SMD is that the results are mostly qualitative because the forces applied are much higher than what is biologically relevant. However, using Jarzynski's equality, one can extract quantitative potentials of mean force (PMF) from non-equilibrium processes (SMD) (133). This technique has been applied to probe ligand binding domains in hRAR, pull sugar molecules through GlpF, and investigate gating mechanisms in MscL (134-136). Here, we describe an iterative theoretical/experimental approach using

qualitative SMD on our ChR2 homology model to identify residues which contribute to barriers of conductance and progressive selectivity in ChR2.

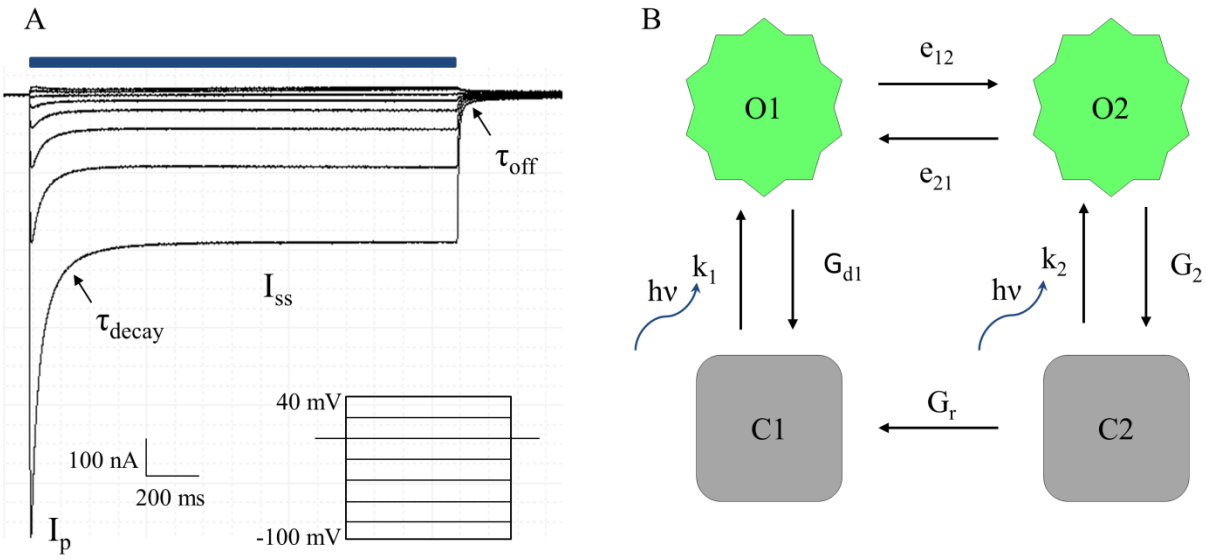

Figure 4.1.1 – Channelrhodopsin-2 photocurrent and photocycle overview
(A) Representative ChR2 photocurrent traces at varying membrane potentials. The blue bar represents photoactivation with 470 nm light. (B) Four-state photocycle of ChR2 with two conducting (O1 and O2) and two non-conducting (C1 and C2) states. Each transition is represented by the corresponding rate parameter used in the kinetic model. The blue arrows represent light-assisted transitions.

The four-state photocycle model can quantify the transition states for ChR2 under prolonged activation, but the mechanism of light-induced ChR2-mediated cation conductance is unresolved. Analysis of structural and functional experiments have led to the proposal that ion permeation occurs between TMs 1, 2, 3, and 7 which form a large extracellular vestibule filled with water and lined with negatively charged residues (29, 33, 61). More specifically, TM 2 contains five glutamate residues that affect the ion selectivity and function of ChR2 (29, 58). Cysteine scanning mutagenesis followed by labeling with methanethiosulfonate derivatives on TM 3 and TM 7 provided experimental evidence that residues which comprise these TMs

partially mediate ion conductance (57, 61). Among these residues is L132, which when mutated to cysteine (CatCh mutant) has large stationary currents and increased Ca^{2+} permeability compared to WT ChR2 (137). Mutation of Q117, which resides at the interface of the extracellular domain and TM 3, has been proposed to disrupt a potential hydrogen bond with E101 at the extracellular interface on TM 2. This hydrogen bond has been suggested to play a role in ion conductance and permeability of ChR2 (61). Furthermore, residues located on the extracellular side of TM 7 and facing TMs 1 and 3 affect ion conductance, kinetics, and serve to funnel cations into the pore region (138).

Equally significant for understanding ChR2 function is the gating mechanism for activation. Initially, it was thought that a hydrogen bond was required between C128 and D156 for proper channel function and kinetics (41, 42). This hydrogen bond is consistently found throughout microbial-rhodopsins such as the proton pump bacteriorhodopsin (bR), where it contributes to overall protein stability (43, 44, 95). Mutagenesis of C128 exhibited an increased conduction lifetime, which suggested alteration of the potential hydrogen bond between C128 and D156 (18, 41, 42). However, inspection of the channelrhodopsin chimera C1C2 crystal structure revealed that the distance between C128 and D156 is greater than 4 Å. This suggests that no direct hydrogen bonding occurs between these residues (33). Furthermore, it has been demonstrated that D156 is the internal proton donor for the Schiff base (27). This indicates that C128 has an undiscovered role in ChR2 function. Currently, gating has been suggested to be controlled, at least partially, through the large conformational changes of the protein and subsequent hydration of helices (65, 94).

To date, experiments designed to elucidate the unique ion permeation pathway of ChR2 have mainly focused on residues known to be important for homologous retiylidene-containing

proteins or through targeting of specific transmembrane domains. Here, our objective was to identify and quantify the role of spatially proximal residues along adjacent TMs which form a barrier to ion permeation. To achieve this objective, we applied steered molecular dynamics (SMD) using a sodium ion to an equilibrated ChR2 model, based on the C1C2 crystal structure, to identify residues which comprise a TM barrier. We then generated conservative mutations at identified positions. These mutations were based on inspection of sequence alignments with homologous algal opsin proteins. Photocurrents under extended illumination were then measured for WT and mutant constructs. We applied the four-state kinetic model to quantify ChR2 transition parameters from our experimental photocurrent traces (16, 20). Finally, photocurrent traces were analyzed to quantify ion conductance, kinetics, and reversal potentials of each mutant ChR2. Using this approach we have identified proximal residues which contribute to the two conducting states as well as the kinetics and cation selectivity of ChR2.

4.2 Materials and methods

4.2.1 Building the structural model of channelrhodopsin-2 and molecular dynamics

The ChR2 model was created using the crystal structure of the channelrhodopsin chimera C1C2 as a template (PDB: 3ug9) and equilibrated as previously described (33, 138). All simulations were carried out using NAMD 2.7 using constant number, pressure, and temperature (NPT) in addition to periodic boundary conditions (125). Constant temperature and pressure were maintained by utilizing Langevin damping and Langevin piston dynamics. Full-system electrostatics were treated using particle mesh Ewald forces. Short-range van der Waals interactions had a 12 Å cutoff and a switching function at 10 Å. The CHARMM 27 force-field was used for all MD simulations with 1 fs time-steps (126, 127). Initially, a 500 ps minimization was performed to melt lipid tail groups while water and protein remained fixed. Minimization

was then continued for a second 500 ps simulation in which water was released(139, 140) . Lastly, a 40 ns equilibration with the entire system released was performed.

SMD simulations were initialized from the final time-step of the equilibration. Pulling directions were utilized to explore the pathway of sodium conductance through the putative pore of ChR2. The arbitrarily placed sodium ion was tagged for pulling with a spring constant of 5 kcal/mol Å and pulling velocities of 5 Å/ns and 1 Å/ns. Similar trajectories were observed for pulling velocities 5 Å/ns and 1 Å/ns. Forces applied to pull the sodium ion were counteracted by anchoring the protein through the Cα of select residues that were located at the interface of lipid and water and facing into the lipid to prevent the bilayer and protein from moving along the same axis as the pulled ion. Three trials were performed. All SMD simulations were performed at 293 K.

4.2.2 Microbiology and Electrophysiology

Expression and functional measurements of ChR2 mutants were carried out as previously described (61, 138). Cells were measured at membrane potentials ranging from -100 to +40 mV in 20 mV steps in either Na^+ solution at pH 7.0, Na^+ solution at pH 9.0, or K^+ solution at pH 9.0 (115 mM XCl, 2 mM $BaCl_2$, 1 mM $MgSO_4$, 10 mM HEPES (pH 7.0) or Tris (pH 9.0) where X = Na^+ or K^+).

4.2.3 Numerical Fitting

The mathematical model was developed based on the four-state photocycle model (16, 20). This model is described by two closed states (C1 and C2) and two open states (O1 and O2) by the following rate equations:

$$\frac{dC1}{dt} = G_r * O2 + G_{d1} * O1 - k_1 * C1 \quad (1)$$

$$\frac{dC2}{dt} = G_{d2} * O2 - (k_1 + G_r) * C2 \quad (2)$$

$$\frac{dO1}{dt} = k_1 * C1 + e_{21} * O2 - (G_{d1} + e_{12}) * O1 \quad (3)$$

$$\frac{dO2}{dt} = k_2 * C2 + e_{12} * O1 - (G_{d2} + e_{21}) * O2 \quad (4)$$

$$C1 + C2 + O1 + O2 = 1 \quad (5)$$

Where C1, C2, O1, and O2 represents the population of each state. The light-dependent transitions k_1 and k_2 represent the transition from C1 -> O1 and C2 -> O2. The back reactions for these transitions are G_{d1} and G_{d2}, respectively. The rates e_{12} and e_{21} are the forward and back reactions between the open states and G_r is the thermal conversion from the desensitized C2 to the C1 state. The light-dependent activation rates are determined by the quantum efficiency of photon absorption for retinal:

$$k_{1/2} = \varepsilon_{1/2} F p \quad (6)$$

Where $\varepsilon_{1/2}$ is the quantum efficiency of C1 or C2, F is the photon flux, and p is the sigmoidal activation function described previously(141) :

$$\frac{dp}{dt} = (S_o(\Theta) - p)/T_{ChR2} \quad (7)$$

With T_{ChR2} representing the time constant of ChR2 activation. Finally, the current (I) flowing through ChR2:

$$I = I_{max} (O1 + \gamma O2) \quad (8)$$

where $I_{max} = (V_m - E_{rev}) * g_1$ and γ is the ratio of channel conductance between O2 and O1 (g_2/g_1).

Photocurrent traces were imported and curve fittings for the four-state model were performed using Mathworks MATLAB R2013. Differential equations were solved using the ODE23 solver in MATLAB. Parameter optimization and minimization was done using the sum of squared errors. For each ChR2 mutant, a global optimization of the parameters was performed using the simulated annealing algorithm(20). Parameters were altered until the fit was a good approximation of the data. Lastly, a constrained gradient optimization was performed using the fmincon function (19).

4.3 Results

To minimize the system energetic state prior to SMD experiments, lipid tail groups were melted during a 500 ps equilibration while keeping water and protein fixed. Next, a second 500 ps equilibration was performed with only the protein fixed. Finally, the entire system was released during a 40 ns equilibration. This time frame has been shown previously to be sufficient for performing SMD simulations (140, 142). Figure 4.3.1 shows the overall structure and RMSD of the protein backbone during the 40 ns equilibration. Following an initial change (< 0.5 ns) in RMSD only small fluctuations were observed during the 40 ns equilibration. This indicated that the structure was equilibrated. Analysis of residue dihedrals demonstrated that they were within the allowable limits after the 40 ns simulation (Figure 4.3.2).

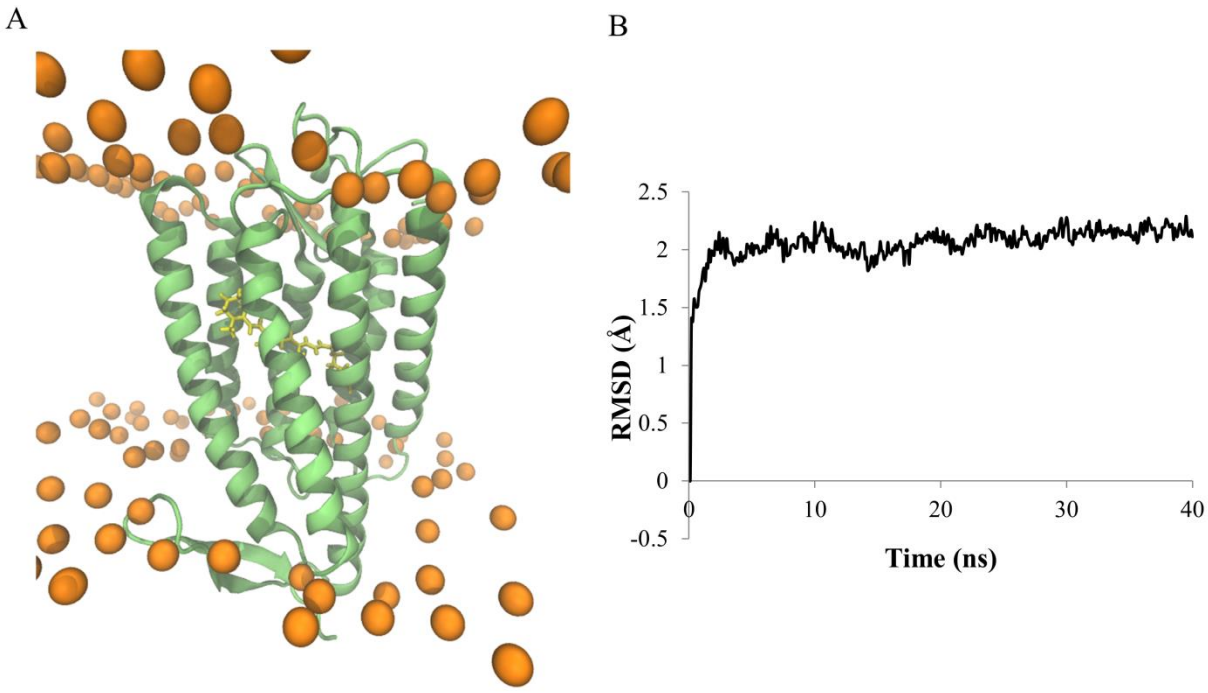

Figure 4.3.1 – Channelrhodopsin-2 model after 40 ns equilibration.
(A) Overall structural model of ChR2 used for SMD simulations with retinal shown in yellow and phosphate lipid head groups shown in orange. (B) Root mean square deviation (RMSD) of ChR2 alpha-helical backbone atoms during equilibration. The RMSD was calculated using the initial timestep as a reference point.

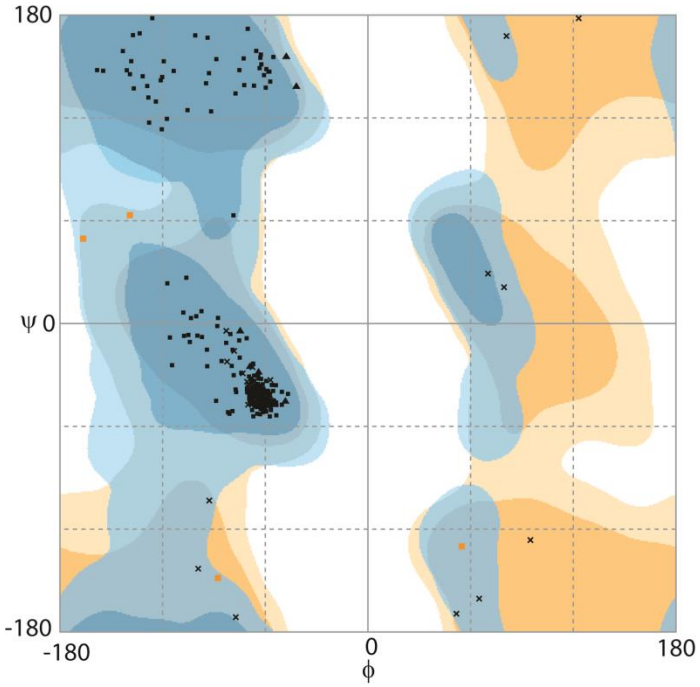

Figure 4.3.2 - Ramachandran plot of equilibrated ChR2 homology model
Plot created after a 40 ns equilibration using the RMAPAGE server, as in chapter 3.

Visual inspection of the equilibrated ChR2 model resulted in the observation of bends in both TM 3 and 5, a result of intrahelical hydrogen-bonding between a threonine at position *i* and the carbonyl backbone at *i-4* (92, 143). The hydrogen-bond on TM 3 was formed between the hydroxyl sidechain of T127 and the backbone carbonyl of E123 while the hydrogen-bond on TM 5 was formed between the hydroxyl group of T188 and the backbone carbonyl of Y184. Hydrogen bond stability was also observed for the E90/K93 and S63/N258 pairings during the equilibration. No hydrogen bonding between C128 and D156 was observed in our equilibrated structure. The presence or absence of hydrogen-bonds between these sets of residues are consistent with that found in the C1C2 chimera and other ChR2 homology models (33, 47, 143).

4.3.1 Conduction Pathway

Following equilibration, SMD was applied to a sodium ion placed above the center of the electronegative cavity of ChR2. SMD has previously been used to resolve the conduction pathway in the KcsA potassium channel, ion binding sites of the sodium symporter LeuT and identify barriers for glycerol permeation in aquaglyceroporin (135, 142, 144). SMD allows for external forces to be applied to molecules on a time scale suitable for molecular dynamic simulations (144). Sodium entered the pore at the large extracellular vestibule formed between TM domains 1, 2, 3 and 7 (Figure 4.3.3A). This region contains several residues which have been shown to contribute to funneling cations into the pore in addition to negatively charged residues which contribute to ChR2 selectivity(138, 145). The Na^+ permeation pathway continued in this direction to the side chain of K93 where the applied force increased. From here, the ion entered the TM occlusion site formed by S63, E90, and N258. Notably, two pairs of stable hydrogen bonds were formed between S63/N258 and K93/E90. When sodium entered this occlusion site, both of these hydrogen bonds were broken and then reformed following sodium permeation. The side chain of V86 steered the ion to the inner gate of Y70 (Figure 4.3.3C) by preventing the ion from permeating out of the pore either through streic occlusion or a hydrophobic interaction. Sodium exits the pore between TMs 2, 3, 7, and the small intracellular loop between TMs 1 and 2 (IC1) where the applied force reached a second maxima (8 ns in Figure 4.3.3B). IC1 contains highly conserved residues between other microbial-type and channelrhodopsins. No large change in conformation of IC1 was observed.

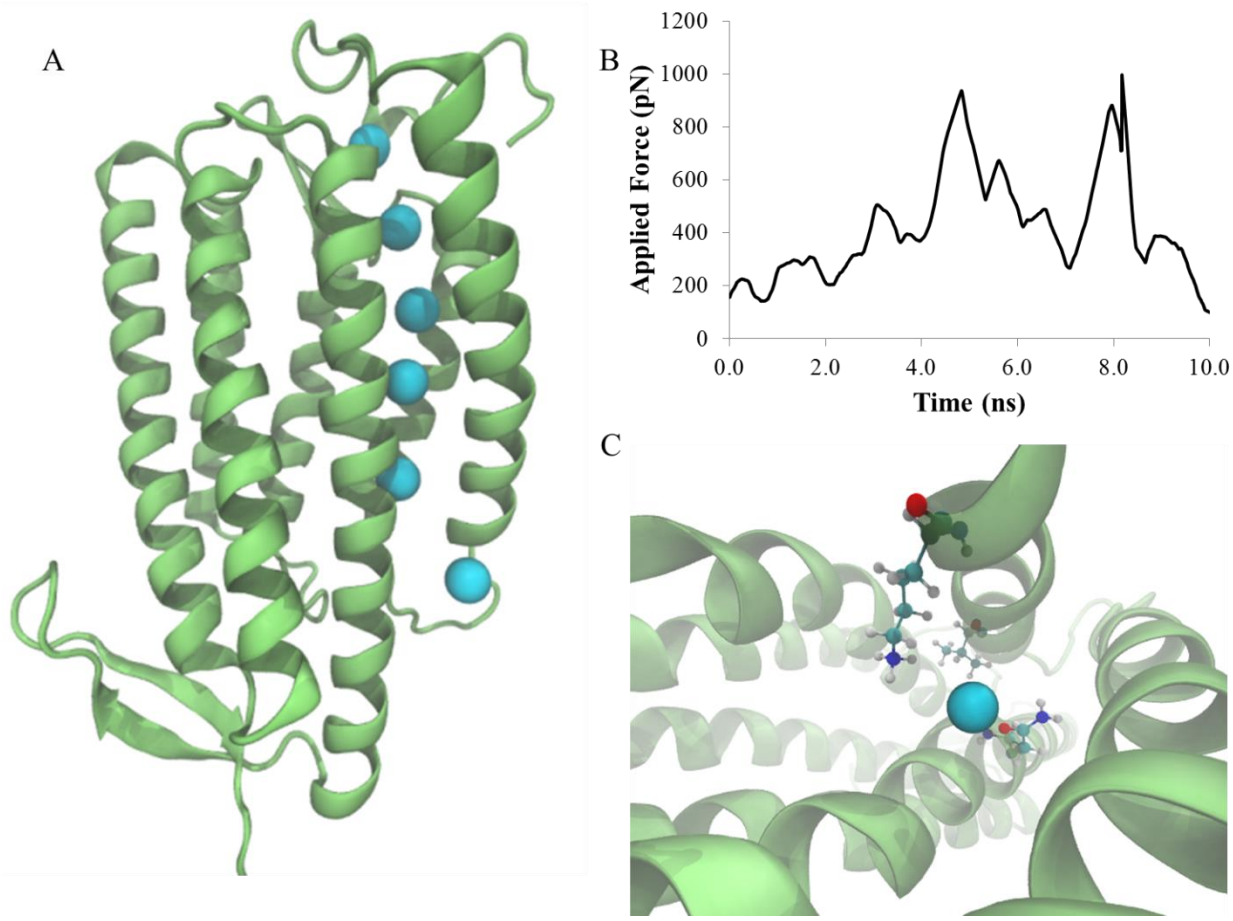

Figure 4.3.3 – SMD pulling profile

(A) Pathway of sodium permeation during a 9.3 ns SMD simulation represented by time points every 1.5 ns. (B) Average force calculated from individual SMD runs using a rolling average window of 500 fs. The force was normalized to the vector used for pulling. The large initial force maximum region corresponded to residues V86, K93, and N258. The second peak was observed as sodium was exiting the pore at the interface of the TM domains and intracellular space. (C) View down the ChR2 pore from the extracellular side with the three residues of interest shown.

4.3.2 Force profile of sodium conduction

A normalized force profile was calculated for each individual trial as a rolling average of 500 fs windows and averaged (Figure 4.3.3C). Distinct force maxima were observed at 5.0 ns and 8.3 ns which suggest that multiple barriers to ion translocation were encountered during SMD trajectories. Snapshots of this trajectory revealed residues surrounding sodium at time

points corresponding to the force maxima. Analysis of our model between 4.5-6.0 ns revealed that V86, K93, and N258 closely interacted with the pulled sodium ion and prevented it from progressing down the pore (Figure 4.3.3C). The second force maximum was encountered at the interface of the intracellular and TM domains as the ion exits the pore.

4.3.3 Electrophysiology of barrier mutants

We utilized two-electrode voltage clamp electrophysiology to quantify the functional role of the three residues which comprise the TM constriction site. Mutations were guided by a ChR2 sequence alignment with known algal opsin proteins (Figure 4.3.4) (67). V86 was mutated to alanine and leucine, K93 to asparagine and isoleucine and N258 to valine and glutamine. ChR2 mutants were then tested for functional expression in *X. laevis* oocytes. The ChR2 proteins containing V86L, K93I, K93N, and N258Q mutations had light-induced current (Figure 4.3.6A). The V86A and N258V mutations resulted in no functional expression and were not examined further. Interestingly, a complete reduction of peak currents was observed for the V86A mutation upon subsequent light pulses (Figure 4.3.5).

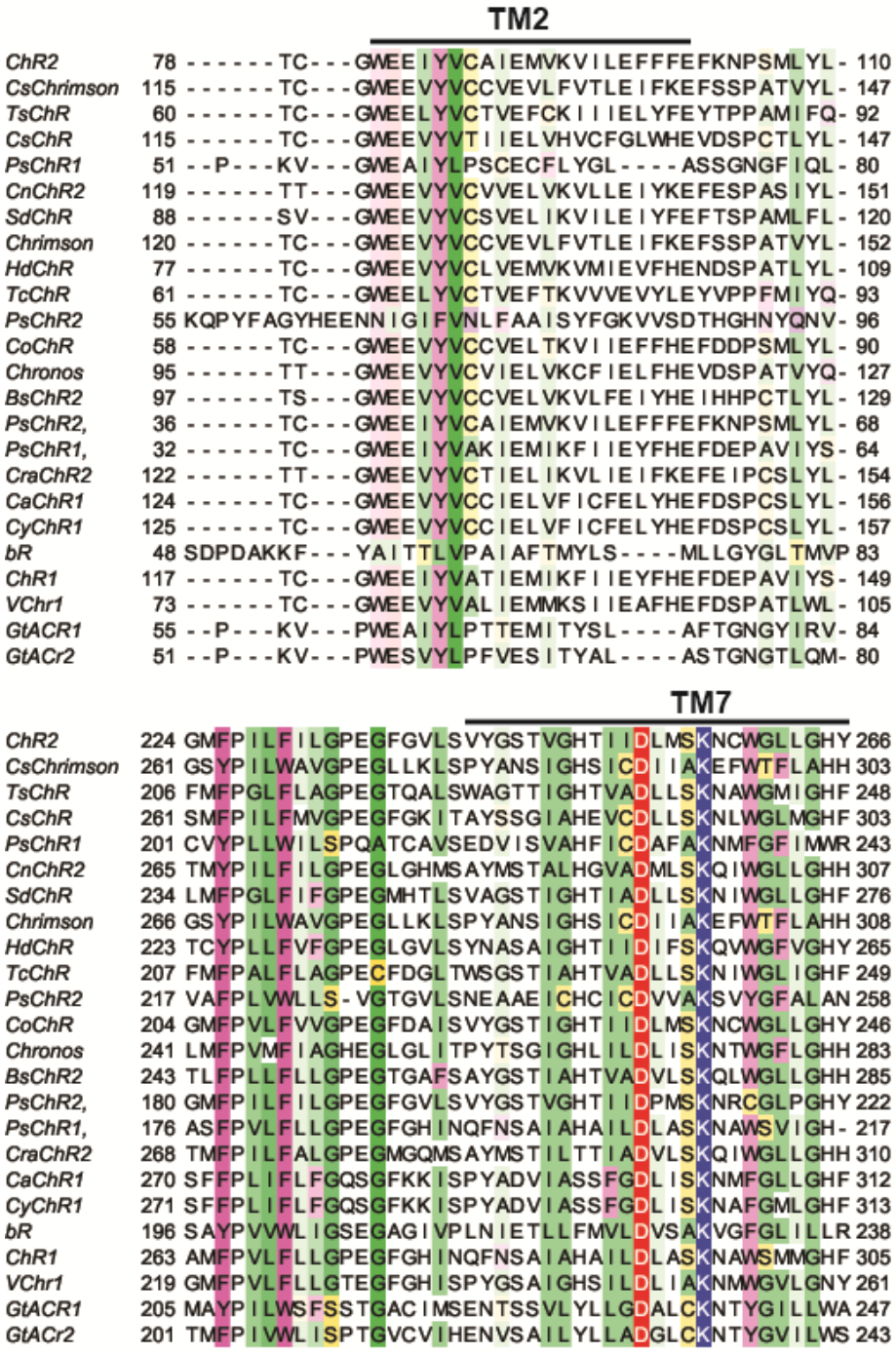

Figure 4.3.4 – Sequence alignment of known channelopsins

Putative transmembrane domains are indicated by black bars. Shaded regions indicate sequence conservation. Green – hydrophobic residues; pink – aromatic residues; red – acidic residues; yellow – polar residues; blue – basic residues.

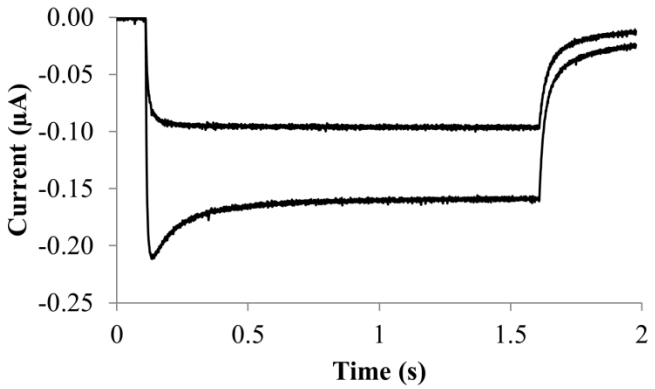

Figure 4.3.5 - Experimental photocurrent traces of ChR2-V86L mutation
Peak currents were abolished upon subsequent light pulses after a 10 s recovery period. Bottom trace – V_m = -100 mV; top trace – V_m = -80 mV.

To quantify changes in ion selectivity for barrier mutants, we measured reversal potentials (E_{rev}) in 115 mM Na^+ solutions at pH 7 and 9 and a 115 mM K^+ solution at pH 9 (Figure 4.3.6B and C and Table 4.3.1). N258Q had a significantly more negative E_{rev} at pH 9 when compared to WT. However, E_{rev} was only slightly more negative at pH 7.0 where the photocurrent is carried mostly by H^+ (145). These large changes in reversal potential demonstrate that N258Q loses permeability for Na^+ and K^+, but not H^+. E_{rev} for both K93 mutants were similar to WT and did not appear to alter the selectivity for any of the ions measured. However, when changes in I_p and I_{ss} E_{rev} were considered, both mutations at K93 had progressively decreased permeability for Na^+ compared to WT. This ΔE_{rev} gives an indication of the permeability of ions as ChR2 progresses through the photocycle (17). Conversely, V86L E_{rev} were shifted more positive showing increased permeability for Na^+ (-20.3 ± 0.6) and K+ (-17.5 ± 0.8) with respect to WT.

	Erev (Na pH 7.0)	Erev (Na pH 9.0)	Erev (K pH 9.0)	Iss/Ip	Tau decay (ms)	Tau off (ms)
WT	0.24 ± 0.6	-31.7 ± 0.6	-37.0 ± 0.8	0.36 ± 0.01	51.8 ± 5.9	6.4 ± 0.2
V86L	2.6 ± 1.0	-20.3 ± 0.6*	-17.5 ± 0.8*	0.69 ± 0.01*	83.6 ± 7.1*	17.2 ± 0.5*
K93I	2.1 ± 0.7	-30.3 ± 0.8	-34.2 ± 1.2	0.48 ± 0.008*	35.6 ± 1.7*	5.7 ± 0.2
K93N	2.5 ± 1.0	-31.3 ± 0.8	-36.3 ± 0.9	0.36 ± 0.01	25.8 ± 1.2*	5.5 ± 0.2*
N258Q	-3.8 ± 0.6	-58.3 ± 1.9*	-69.5 ± 1.0*	0.20 ± 0.003*	26.9 ± 0.8*	5.7 ± 0.09*

Table 4.3.1 - Summary of results from analysis of electrophysiological recordings
Reversal potentials were determined from stationary currents in the indicated solution. Tau values reported are at Vm = -100 mV. Values reported are ± SEM with n = 7-11; * P < 0.05

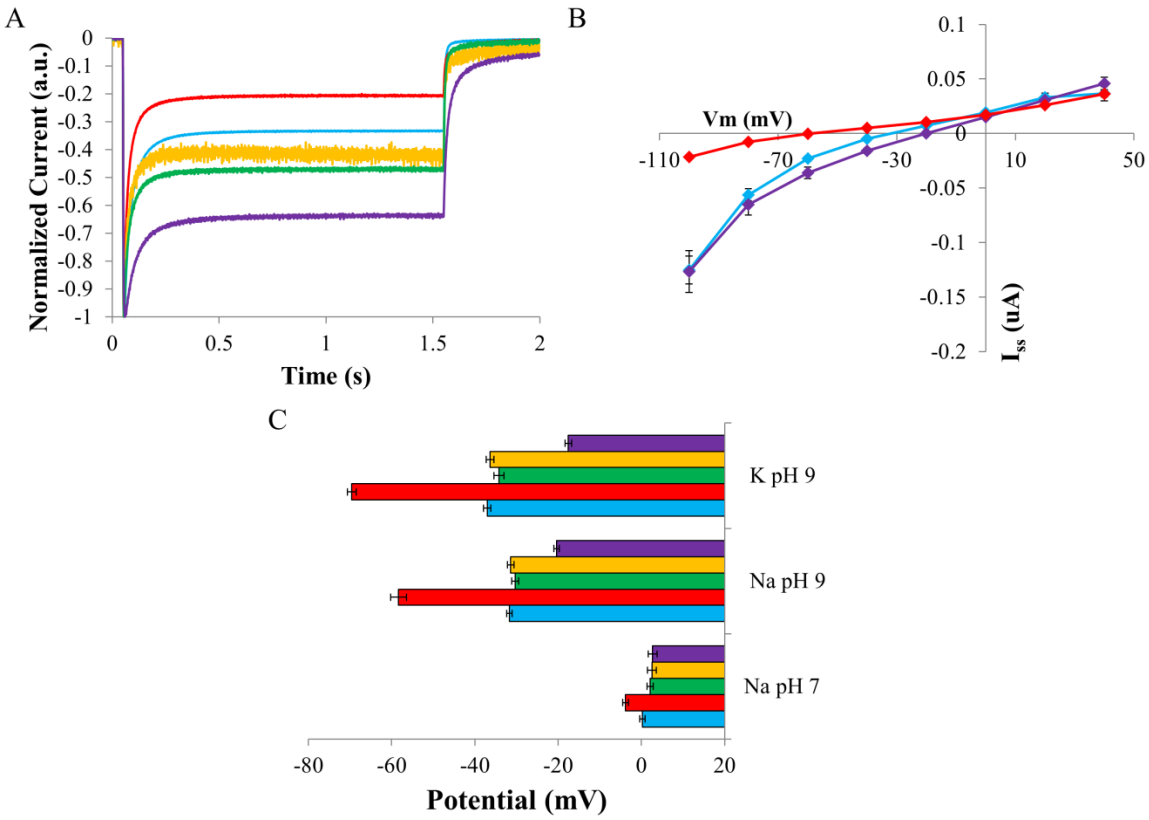

Figure 4.3.6 – Summary of electrophysiological results
WT – blue; V86L – purple; K93I – green; K93N – yellow; N258Q – red. (A) Normalized ChR2 photocurremt for WT and barrier mutants at V_m = -100 mV in Na^+ solution pH 7.0. The blue bar corresponds to light activation with 470 nm light. (B) Current-voltage relationship of WT, V86L, and N258Q in Na^+ pH 9.0 solution. (C) Average reversal potentials calculated for each solution from stationary current I/V curves. n = 7-11; error bars represent the SEM. * P < 0.05; ** P < 0.01.

We also compared steady-state to peak current ratios (I_{ss}/I_p), which are a measure of ChR2 inactivation during prolonged light exposure(34). V86L and K93I had significantly increased ratios compared to WT indicating less inactivation (Table 4.3.1 and Figure 4.3.6A). Conversely, N258Q had small ratios and therefore higher inactivation (18.8 ± 0.8%), while K93N had no significant change.

Apparent kinetic rates were extracted from photocurrent traces by exponential fitting. The decay rate is quantified by fitting photocurrents with a monoexponential equation (34). Similarly, ChR2 undergoes biphasic decay when the light is turned off which is quantified by fitting with a biexponential equation. Apparent decay and off rates for all barrier mutants were determined at different holding potentials (Figure 4.3.7 and Table 4.3.1). Both K93I and N258Q had faster decay rates compared to WT (Figure 4.3.7A). Likewise, both of these mutants had faster off-rates than WT, but were less drastic (Figure 4.3.7B). In contrast, V86L decay and off kinetics were severely reduced. Decay rates for V86L were only determined at -100 mV because of the loss of I_p upon subsequent light pulses (Figure 4.1.1A). These rates were used as guidance for the four-state kinetic model.

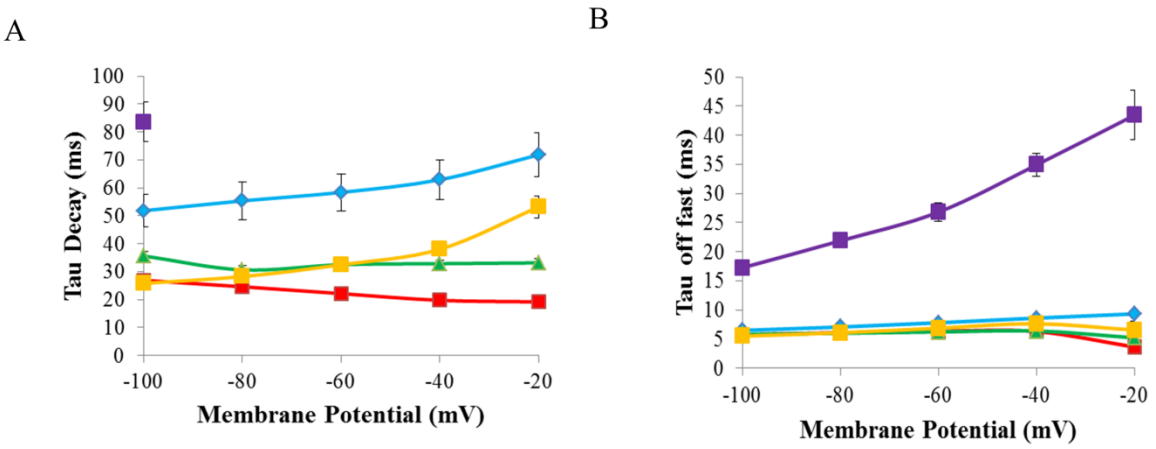

Figure 4.3.7 – Kinetic analysis of ChR2 photocurrent
(A) Decay rates are determined from monoexponential fitting from I_p to I_{ss} at the indicated V_m. (B) Off rates were determined from the biexponential decay after the light was turned off.

4.3.4 Four-state kinetic model

The four-state kinetic algorithm was applied to ChR2 experimental photocurrent traces to quantify the discrete transitions that occur during the photocycle. Furthermore, this approach can be used to look at the relative occupancy of open and closed states in a time-resolved manner. Here, we used multi-parameter optimization to obtain theoretical fits and physical parameters describing ChR2 transition under continuous illumination using equations 1-5 and 8 (Figure 4.3.8). Analysis of electrophysiology experiments were used as guidance for seeding initial parameter values (16, 19). Inspection of N258Q parameters identified a faster transition from O1 to O2 and lower γ than WT (Table 4.3.2). In contrast, the conductance ratio for V86L was much higher than WT and other barrier mutants, indicating that the large relative stationary currents observed for this mutant were caused by a higher conductance in O2. There were no changes in γ for both K93 mutants.

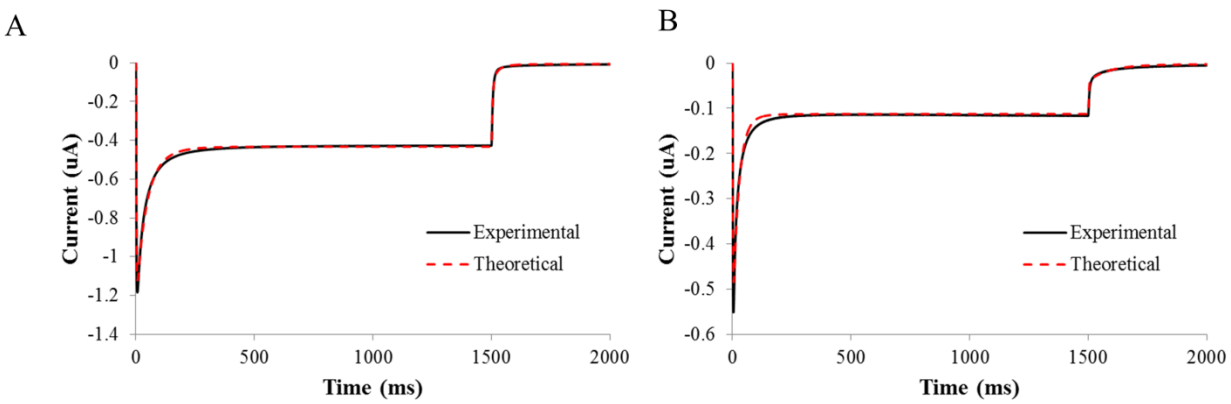

Figure 4.3.8 - ChR2 kinetic modeling fitting results of WT and N258Q
The experimental traces are shown in black and the theoretical model is shown as red dashed lines.

	G_{d1} (ms^{-1})	G_{d2} (ms^{-1})	E_{12} (ms^{-1})	e_{21} (ms^{-1})	I_{max} (μA)	γ	G_r (ms^{-1})	T_{ChR2} (ms)
WT	0.26 ± 0.03	0.029 ± 0.009	0.036± 0.005	0.008± 0.002	2.55 ± 0.4	0.047± 0.01	0.0067± 0.001	0.63± 0.02
V86L	0.045 ± 0.001*	0.0003 ± 0.0001*	0.006 ± 0.0007*	0.0066 ± 0.0006	0.384 ± 0.05	0.201± 0.02*	0.016 ± 0.004*	0.90 ± 0.05*
K93I	0.238 ± 0.01	0.010± 0.001*	0.047± 0.008	0.021± 0.004*	0.71 ± 0.1	0.034± 0.006	0.0065± 0.001	0.64 ± 0.01
K93N	0.19 ± 0.01	0.0043 ± 0.001	0.057± 0.003*	0.016± 0.001*	0.348 ± 0.05	0.017 ± 0.006*	0.010 ± 0.002*	0.74 ± 0.1
N258Q	0.51 ± 0.2*	0.0058± 0.001*	0.105 ± 0.004*	0.0070 ± 0.0008	1.68 ± 0.13	0.019± 0.001*	0.0093 ± 0.001*	0.98 ± 0.07*

Table 4.3.2 - calculated parameters for fitting experimental photocurrent traces
Each parameter is the average of 7-11 cells and values are reported ± SEM.

Rates of transitions between states were also calculated. The rates of transition from O1 -> O2 (e_{12}) differed for barrier mutants. For N258Q and K93I, this rate was accelerated while for V86L it was highly reduced. These theoretical results correlated with the decay rates calculated for each mutant where N258Q and K93I were faster than the WT and V86L was slower.

Additionally, we investigated the population of conducting states at I_p and I_{ss} (Table 4.3.3). The population of the O2 state was similar at maximal currents for WT and all barrier mutants (7-11%). However, large differences in O1 population were calculated. V86L was made up primarily of O1 at maximal current (77%) while WT was significantly less (46%). A similar trend was observed under stationary conditions where V86L had a much higher contribution from O1 than WT. Thus, the large I_{ss}/I_p ratio observed for V86L is a consequence of a higher population of O1 together with higher O2 conductance. In contrast, N258Q has a small population of O1 (28%) at maximal current. Furthermore, during stationary currents, the O1 population dropped off drastically to 5% with a large rise in O2 population (78%). Therefore, N258Q current is carried largely by the O2 state because of low O1 population at stationary currents and a low γ value. Both mutations at K93 did not significantly affect the population of states compared to WT ChR2. Lastly, we compared I_{ss}/I_p ratios to the results of our population analysis. The percent decrease in O1 population from I_p to I_{ss} in our model correlated well with I_{ss}/I_p ratios determined from analysis of our electrophysiology results.

State Population	**WT**	**V86L**	**K93I**	**K93N**	**N258Q**
Time to Peak (ms)	7.4	15.8	7.6	6.9	5.3
O1 Peak	0.46	**0.77**	0.44	0.46	**0.28**
O2 Peak	0.07	0.05	0.09	0.12	0.11
O1 Stat	0.15	**0.47**	0.21	0.18	**0.05**
O2 Stat	0.54	0.42	0.43	0.61	**0.78**

Table 4.3.3 – Population of ChR2 states determined for calculating the theoretical current.

Peak populations are representative of the open states at maximal current while the stationary population was determined from 10 ms before the light was turned off.

4.4 Discussion

Channelrhodopsin-2 is a unique dual-functionality protein in that it conducts cations of multiple valencies down the electrochemical gradient as well as pumps protons with low efficiency (0.3 H^+ per photocycle) in the absence of an electrochemical gradient (55). Activation of ChR2 is the first committed step in phototaxis and has become a facile tool to control excitable cells such as muscle and neuronal cells, with light. Here, we have used a multi-modal approach, including steered molecular dynamics, two-electrode voltage clamp and enzyme kinetic modeling to identify and quantify the contribution of spatially proximal residues along adjacent TMs to the ChR2 photocycle and cation selectivity.

Trajectories obtained from SMD simulations were consistent with cations entering the putative pore region between TMs 1, 2, 3, and 7. Small resistance was encountered during the beginning stages of pulling, where the ion was located in the large electronegative vestibule. The large force observed from 4.5 ns to 6.5 ns was correlated to three residues, V86, K93, and N258, which directly hinder sodium translocation (Figure 4.4.1). A second force maximum was observed at the end of the trajectory and was located at the interface of the intracellular and TM domains.

Inspection of a sequence alignment of homologous algal opsin proteins revealed that V86 (in TM2) encodes hydrophobic residues (I, A, or L) (Figure 4.3.4). While V86A resulted in a photoinsensitive protein, the V86L mutation had larger I_{ss}/I_p ratios than WT or any of the other mutants presented here, indicating a low level of inactivation and increased O2 ion conductance. This was confirmed through our kinetic-modeling data with significantly higher γ values than WT. As there was a complete abolishment of peak currents on subsequent light activation, this is indicative that V86 contributes to the recovery back to the ground state.

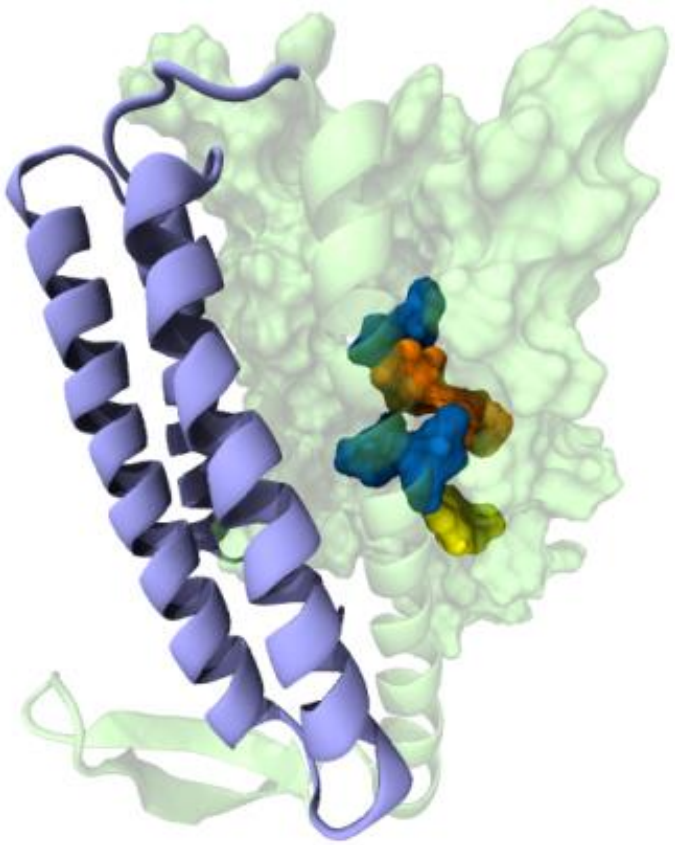

Figure 4.4.1 – ChR2 barrier mutant location

ChR2 homology model showing the location of V86, K93, and N258 (blue), the central gate (orange; S63 and E90) and inner gate (yellow; Y70). TMs that line the permeation pathway are shown in green while TMs 4-6 are shown in blue. Figure created using VMD.

Analysis of the modeling results also indicates a very slow rate of transition from O2 to C2 (G_{d2}) and from C2 to C1 (G_r) when compared to WT ChR2. A similar kinetic effect was observed for the slow-cycling C128T and G224S mutants where subsequent light pulses had severely reduced I_p and had an extended conducting state life-time (42, 57). Previously, it has been demonstrated that TM 2 undergoes a large conformational change that is partially responsible for channel gating (65, 94). Additionally, E82 has been implicated as a crucial

structural element in ChR2 that links movement of TM2 with the other helices. Therefore, it is likely that V86L, which is located one turn above E82, inhibits the movement of TM 2 delaying the opening and closing of the channel. Interestingly, V86L has nearly identical rates for the forward and back transitions of O1 <-> O2 indicating no preference for either state. This position appears to be structurally important for the transition from O1 to O2 under continuous illumination.

Further evidence of the importance of V86 to ChR2 structure is the lack of photocurrent from V86A, which is a similar phenotype to the E82A mutant. Not only does TM 2 have strong structural implications in ChR2, it also has a large role in the ion selectivity for ChR2 (58). V86L had reversal potential shifts of +11.4 ± 0.9 mV and +19.4 ± 1.1 mV compared to WT for sodium and potassium respectively, indicating increased permeability for these ions.

Sequence homology among algal opsin proteins reveals that there is high conservation of asparagine or glutamine at positions homologous to N258 in ChR2. Mutation of N258 to the hydrophobic valine resulted in negligible photocurrent under our experimental conditions. However, the N258Q mutation resulted in functional ChR2, but with negatively shifted reversal potentials. The highly reduced permeability for N258Q has also been observed for the homologous mutation in C1C2. At pH 7.0, N258Q is similar to WT permeability, but decreasing the external H^+ component at pH 9.0 results in hyperpolarized E_{rev}. More specifically, when measuring current in K^+ solution, we would expect E_{rev} to be marginally less than 0 mV if K^+ is the only permeable ion. However, the internal pH of oocytes is approximately 7.4 and the measured E_{rev} of -69.5 ± 1.0 mV for N258Q at a pH_e of 9.0 indicates outward proton flux with minimal contribution from K^+. This is further supported by the similar E_{rev} with external Na^+ at

pH 9.0. We conclude that N258Q severely reduces both Na^+ and K^+ conductance and that this position is a major determinant of ChR2 selectivity.

N258Q also displayed accelerated decay kinetics compared to WT, which we attribute to the transition between O1 and O2. Not only does this transition occur much more rapidly than WT, but a larger population of ChR2 occupies O2 in the stationary state. O2 appears to be the kinetically favored state for N258Q. Mutation of the homologous residue in the C1C2 chimera to glutamine also revealed more hyperpolarizing $E_{rev,}$ which was suggested to contribute to chloride permeability (60).

It has been proposed that N258 forms a hydrogen-bond with E90 and also S63. Introduction of a negative charge at this position (N258D) results in increased permeability for divalent cations. We suggest that loss of Na^+ and K^+ flux is a result of the strengthening of the hydrogen-bonding network at the central gate and destabilization of O1. This would prevent larger ions from permeating, but allow for H^+ transport. Furthermore, this residue appears to be critical to ChR2 ion specificity and could be used to predict channel selectivity in channelopsins with unknown function.

Both K93 mutants had no effect on ion permeability. This result is surprising as K93 is located in the extracellular vestibule pointing into the pore and is positively charged. Previously, mutation of K132 in C1C2 (K93 in ChR2) to alanine indicated increased K^+ permeability relative to Na^+, but we observed no significant permeability difference (ΔE_{rev} = -3.8 ± 0.6 mV)(33). However, under our experimental conditions there is negligible inward H^+ flux (pH = 9.0) and may account for the discrepancy. Moreover, very little difference for our empirical parameters was observed between K93 mutants and WT. However, the kinetic preference for O2 over O1 was decreased for K93I but maintained for K93N when compared to WT. K93 has been shown

to be involved in a complex series of water-mediated hydrogen-bonds involving E123, E90, and N258 (143). The K93I mutation effectively removes this hydrogen-bond, disrupting the equilibrium between the two conducting states. K93N can retain, partially, the hydrogen-bonding network in this region which preserves the stability between O1 and O2 observed for WT. Because both K93I and K93N have similar ΔE_{rev}, the selectivity of ions is likely not related to the hydrogen-bonding network in the region. Instead, the hydrogen-bonding is related to the kinetic stability of states.

Together by combining steered molecular dynamics with electrophysiological measurements as well as molecular and kinetic modeling, we have identified three spatially proximal residues within the ChR2 conducting pathway that modulate fundamental channel properties, including ion selectivity. Equally, these residues are critical components to the structural integrity of ChR2 and mediate transitions between both open and closed states of the ChR2 photocycle. Analysis of these results can be used to elucidate the molecular underpinnings which define the ion channel functionality of ChR2, potentially predict functionality of homologous proteins which have not been tested directly as well as contribute to development of better constructs for optogenetic approaches.

5 Residual hydrophobic mismatch modulates channelrhodopsin-2 function

5.1 Introduction

The lipid membrane functions as a barrier to prevent molecules and solvent from entering and exiting the cell. Equally important is the role of the bilayer in regulating membrane protein structure and function. Membrane proteins consist of hydrophobic transmembrane segments that form a pathway for specific small molecules. The structure of these proteins vary widely, having TM segments of dissimilar length and different oligomerization states. Additionally, activation of membrane proteins induces conformational changes and dynamic interaction with the lipid environment. Thus, the membrane must be a fluid structure to accommodate the structural dynamics and diversity of membrane protein structure.

The physical properties of membranes, such as thickness, curvature, and compression factor, have been shown to directly affect the function of numerous membrane proteins (146-148). The membrane mediated regulation of proteins can be quantified in terms of hydrophobic mismatch. Hydrophobic mismatch occurs when the membrane spanning regions of proteins misalign with the bilayer. As a result, the length of the lipid bilayer will deform to match the hydrophobic core of the protein, minimizing the energetic cost of exposing nonpolar/polar residues at the interface. If the adaptation of the membrane does not fully compensate the hydrophobic core additional energy costs occur. In simple channels, such as the single TM helical gramicidin A channel, the hydrophobic mismatch is easily remediated (149). However, in more complex multi-TM channels the membrane deformation will be asymmetric. Asymmetric burying of hydrophobic residues occurs because adjacent TM segments influence the surrounding environment. The asymmetric profile of the bilayer exposes specific residues to an unfavorable environment (residual hydrophobic mismatch). Moreover, the type of lipid environment changes the exposure pattern of TM helices and residues (Figure 5.1.1). Recently, a

new approach using Continuum Theory-Molecular Dynamics (CTMD) has been developed to account for the complex lipid deformations that occur with multiple TM helices (150). This approach can be used to quantify the solvent accessible area of unfavorably exposed residues due to residual hydrophobic mismatch and calculate the energy penalty.

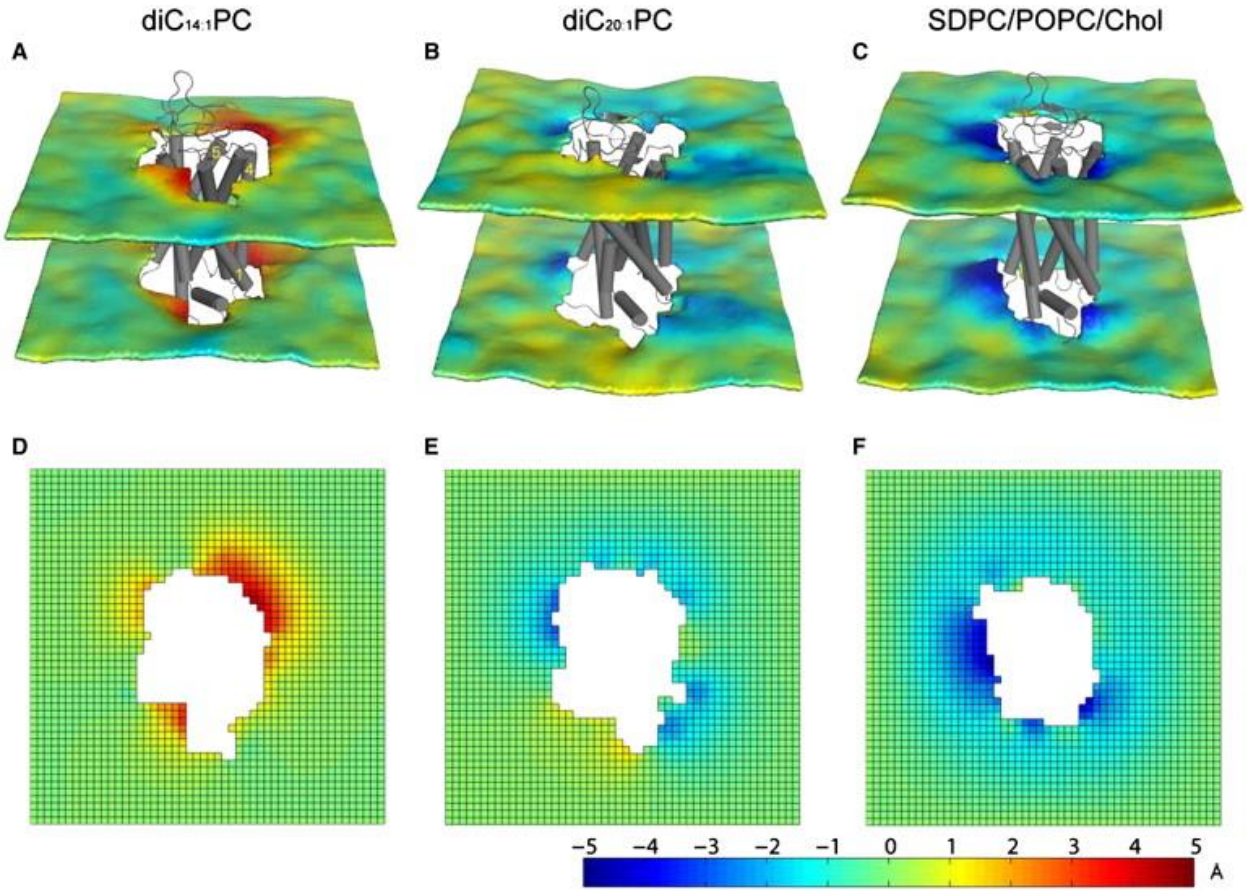

Figure 5.1.1 – Membrane deformation profile of the GPCR rhodopsin
Membrane-deformation profiles $u(x,y)$ for rhodopsin immersed in lipid bilayers of different bulk thicknesses. The upper panel shows $u(x,y)$ calculated directly from MD trajectories for rhodopsin in bilayers composed of (*A*) $diC_{14:1}PC$, (*B*) $diC_{20:1}PC$, and (*C*) 7:7:6 SDPC/POPC/Chol membranes. The lower panel shows the corresponding membrane-deformation profiles $u(x,y)$ for (*D*) $diC_{14:1}PC$, (*E*) $diC_{20:1}PC$, and (*F*) 7:7:6 SDPC/POPC/Chol calculated using the 3D-CTMD approach. The corresponding membrane-deformation energies ΔG_{def} are (*D*) 4.7 k_BT, (*E*) 2 k_BT, and (*F*) 2.6 k_BT. The calculated ΔG_{def} is 1.6 kT for rhodopsin in $diC_{16:1}PC$, and 0.8 kT for rhodopsin in $diC_{18:1}PC$. This figure was reused with permission from (150)

Previous calculations using CMTD have been used to predict the oligimerization state of the GPCRs rhodopsin and the serotonin receptor 5-HT_{2A}R (151). Results from these experiments provided an energetic framework for how these proteins reduce residual hydrophobic mismatch and the dependency of RHM on lipid composition. Alternatively, this approach can be used to identify residues which influence protein-lipid interaction. It was found in LeuT that K288 is facing the bilayer and induces lipid deformation and water penetration in the surrounding area (151). Simulations run with a K288A model reduced the hydrophobic mismatch and energy penalty. Correlated with the experimental observation that the LeuT K288A mutant has improved transport properties, the energetics of RHM is an important consideration of understanding how membrane proteins function in different lipid environments.

The unique properties of ChR2 have made it a popular tool in the new and emerging field of optogenetics, where excitable cells can be controlled by light. ChR2 has the ability to rapidly depolarize the membrane of excitable cells and induce neuronal spiking of action potentials (152). Furthermore, it can be genetically targeted to specific cell types and function without the need of exogenous retinal. ChR2 has been successfully expressed in functionally diverse cell lines, each with unique membrane compositions (152-155). The usefulness of ChR2 has limitations in optogenetics due to the activation wavelength, kinetics, ion conductance properties, and no means to inhibit spiking. In order to expand the optogenetic toolbox, the underlying mechanisms for ChR2 function must be fully resolved. An important consideration moving forward in optogenetics is the influence of lipid composition and RHM on ChR2 function.

Although the full gating mechanism is still unknown, the structural elements that contribute to channel opening are being resolved. Comparatively, ChR2 undergoes more drastic conformational changes than other microbial-rhodopsins. Through analysis of MD simulations

and spin-labeled EPR experiments, it was determined that TM 2 moves and tilts outward by over 3 Å (94, 113). This movement is also sensed by TM 7 through and interhelical hydrogen-bonding network. The TM movement causes reorientation of gating residues resulting in a water filled pore prior to ion conductance (65).

It is clear that the conformational flexibility of ChR2 is an important mechanistic determinant for function. Therefore, it is important to consider how the protein-lipid interaction influences ChR2 function as it progresses through the photocycle. We combine CTMD simulations with voltage-clamp electrophysiology and kinetic modeling to quantitatively describe the effect of RHM on ChR2 function. Previously, we found that mutation of V269 and Q210 to serine greatly reduced function and cation permeability of ChR2 (57). V269 and Q210 are adjacent to other polar and hydrophobic residues on the cytoplasmic side of ChR2 that have important implications for RHM (Figure 5.3.1). We calculated the energy cost of RHM for V269S, V269N, and Q210A. It was found that mutating V269 to asparagine and Q210 to alanine significantly reduced the RHM energy penalty. As a control, the RHM energy cost was calculated to be similar to WT for the null mutant Q210N. Next, we tested function of RHM mutants using electrophysiology. Analysis of experimental results revealed that V269N had smaller photocurrents, reduced permeability, higher inactivation, and accelerated kinetics. Q210A also had reduced photocurrents, higher inactivation, and accelerated kinetics. Finally, we quantified the discrete transitions of these mutants using our four-state kinetic algorithm and determined that RHM contributes to the stability of the open states. These results confirm that the lipid environment at adjacent residues has a fundamental role in regulating the function and conformational stability of ChR2. Additionally, it provides a physical premise for the observed effects of V269S and Q210S (See Chapter 2)

5.2 Materials and methods

5.2.1 Molecular Biology

The gene encoding for a truncated ChR2 (residues 1-308) with a C-terminal hemagluttanin tag was cloned into the pTLN vector between EcoRV and XbaI restriction sites. All point mutations were created using the Quikchange site-directed mutagenesis (Stratagene). Mutations were verified by full gene sequencing.

5.2.2 mRNA synthesis and oocyte injection

Oocytes were extracted from female *Xenopus laevis* frogs by partial ovarectomy. Oocytes were digested in ORI(-) buffer (90 mM NaCl, 2 mM KCl, 5 mM MOPS; pH 7.4) supplemented with 3 mg/mL collagenase type II at 17^{o}C with gentle shaking. After digestion, oocytes were washed with copious amounts of ORI(+) buffer (90 mM NaCl, 2 mM KCl, 2 mM $CaCl_2$, 5 mM MOPS; pH 7.4). ChR2 mRNA was synthesized *in vitro* using the SP6 mMessage mMachine kit (Agilent). The mRNA was diluted to 1 ug/uL in DEPC-treated water. A volume of 50 nL mRNA was injected into each oocyte (50 ng total). Post-injection, oocytes were stored in 5 mL of ORI(+) supplemented with 1.5 μM all-trans retinal and 1 mg/mL gentamycin at 17^{o}C in the dark for 3-4 days.

5.2.3 Electrophysiology

Borosilicate glass electrodes were pulled using a PC-10 puller (Narishge). The microelectrodes were filled with 3 M KCl and had tip resistances between 0.5 – 1.5 MΩ. Voltage-clamping of oocytes was achieved through a Turbo-tec 03X amplifier connected to a 1440A Axon Instruments digitizer. Voltage protocols and current recording were controlled with Clampex software. ChR2 was activated via a 1 mm light guide connected to an Omicron LEDMOD V2 300 mW LED module with an emission wavelength of 470 nm. The membrane

voltage was varied from -100 mV to +40 mV in 20 mV steps. Sodium solutions consisted of 100 mM NaCl, 2 mM $MgCl_2$, 0.1 $CaCl_2$, 5 mM MOPS/5 mM MES at pH 7.5 and 6.0, respectively. Reversal potentials were determined from current-voltage curves at either I_p or I_{ss}. Kinetic parameters were determined by fitting photocurrent traces with monoexponetial (T_{decay}) or biexponential equations (T_{off}).

5.2.4 Four-state modeling

See section 4.2.3 - Numerical Fitting for full details on the fitting procedure

5.2.5 Continuum-theory molecular dynamics and hydrophobic mismatch calculations

All MD simulations and calculations for RHM energy penalties were performed by Sayan Mondal of the Weinstein group at Cornell University (150, 151).

5.3 Results

We used CMTD to quantify the hydrophobic mismatch of a closed state ChR2 homology model embedded in a POPC lipid membrane. Analysis of CTMD trajectories revealed a significant hydrophobic mismatch in WT ChR2 despite membrane deformation. Although membrane deformation alleviated some unfavorable interactions, residues located at the cytoplasmic interface on TMs 2, 6, and 7 remained exposed to the polar/hydrophobic environment. Specifically, Q73 on TM 1 and Q210 on TM 6 were found to be embedded into the membrane. Both of these residues caused membrane thinning in the adjacent regions causing water penetration into the membrane and exposure of V269 to a polar environment (Figure 5.3.1).

The energy cost of residual hydrophobic mismatch was calculated for mutations located at V269 and Q210. Q73 was not calculated because it is located in a modeled loop connect TMs 1 and 2, which is unresolved in the C1C2 chimera template. Mutation of V269 to serine or

asparagine significantly lowered the residual exposure at this position because of the favorable interaction with penetrating water. Equally, mutation of Q210 to alanine also reduced the energetic penalty. Interestingly, the Q210A mutation also lowered RHM at V269, likely by means of reduced water penetration. The energy penalty was also calculated for I95L and Q210N, two mutations which would not affect RHM. Indeed, neither of these null mutations changed the energy penalty compared to WT ChR2.

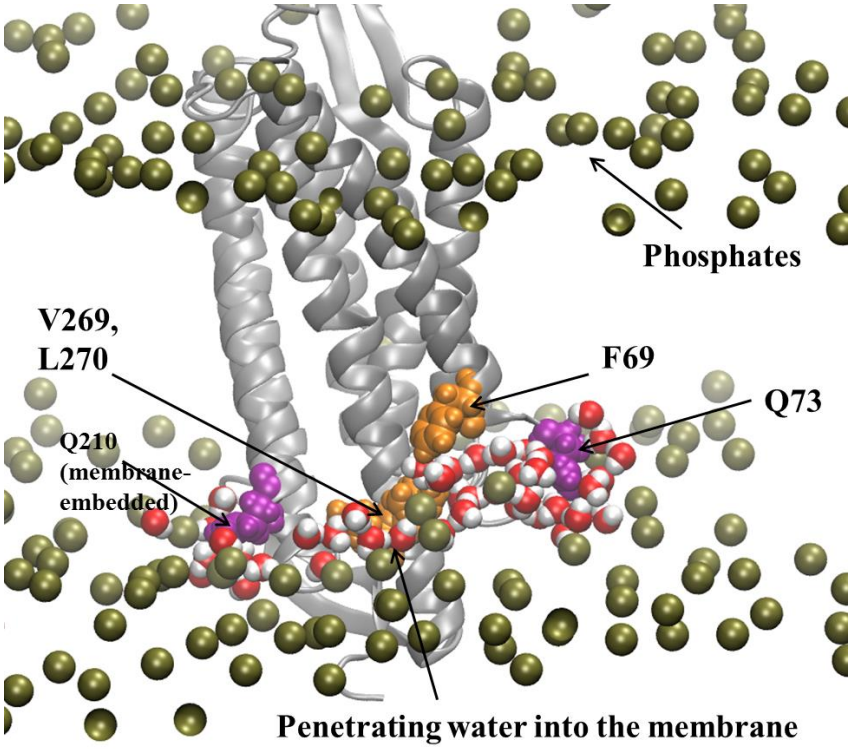

Figure 5.3.1 – Residual hydrophobic mismatch at TM 1, 6, and 7
Snapshot from WT ChR2 MD simulations. Purple – polar residues; orange – hydrophobic residues. The RHM includes contribution from V269 exposed to penetrating water molecules caused by the adjacent membrane embedded polar residues Q73 and Q210.

To understand how RHM functionally affects ChR2 channel conductance, we performed two-electrode voltage clamp measurements in oocytes expressing RHM mutants. We mutated the trio of residues located at the cytoplasmic/TM interface (Q73, Q210, and V269).

Additionally, both null mutants were created (Q210N and I95L). Functional expression of RHM mutants was tested in *X. laevis* oocytes under voltage-clamp conditions. Reduced photocurrent was observed for Q73A, Q210A, and V269N while Q210N had moderately increased photocurrent compared to WT (Figure 5.3.2). Q73A had currents < 50 nA and was not analyzed further. I95L had no observable photocurrent under our experimental conditions.

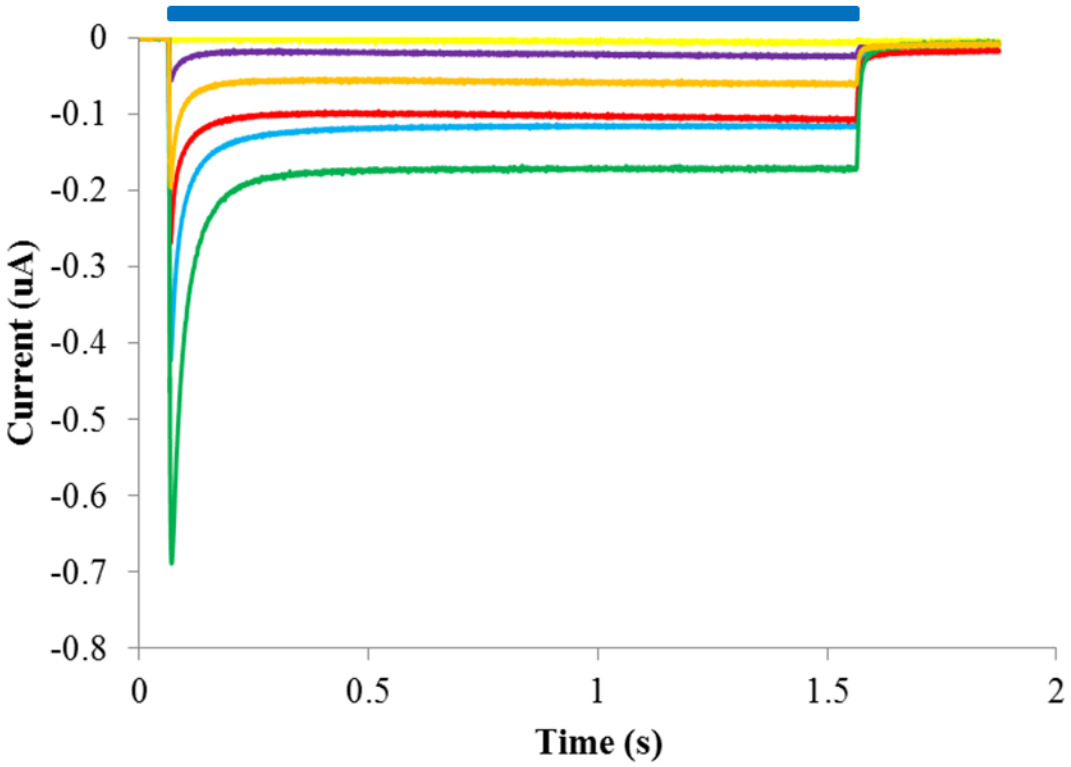

Figure 5.3.2 – Representative photocurrent traces
Photocurrents were recorded in Na^+ solution at pH 7.5 at V_m = -100 mV. Blue bar indicates illumination with blue light. WT – blue; Q73A – purple; I95L – yellow; Q210A – red; Q210N – green; V269N – orange.

We quantified the effect RHM has on ChR2 selectivity by measuring reversal potentials (E_{rev}) at I_p and I_{ss} in Na^+ solutions at pH 7.5 and 6.0 (Figure 5.3.3A) (see Materials and Methods). A positive shift in I_p E_{rev} for V269N was observed at both pH 7.5 and 6.0 compared to WT. The

shift was much larger at pH 6.0 than at pH 7.5, where the current is carried mostly by protons (pH 6.0) and not a mixture of Na^+ and H^+ (pH 7.5). In contrast, a hyperpolarizing shift was observed for this mutant at E_{revs} determined at I_{ss} only at pH 6.0 (V269N – 13.2 ± 1.2; WT – 24.6 ± 1.5) (Figure 5.3.3B and C; Table 5.3.1). This indicated that at the beginning of ion conductance (I_p) permeability of H^+ was increased but decreased at steady-state (I_{ss}) when compared to WT. Equally, when changes in E_{rev} were considered, V269N becomes progressively less permeable for H^+ at pH 6.0. Interestingly, the Q210A mutant had no observable effect on ion permeability. The null mutant did alter the progressive ion selectivity at pH 7.5 and 6.0, but only to a small degree. Steady-state to peak current ratios were also determined, which is a measure of ChR2 inactivation during prolonged light exposure (Figure 5.3.3D). Both Q210A and V269N had significantly increased ratios (Q210A – 0.37 ± 0.01; V269N – 0.33 ± 0.01; V_m = -100 mV, pH 7.5), correlating to larger inactivation under continuous illumination (WT – 0.29 ± 0.007). The Q210N mutation had no effect on I_{ss}/I_p ratios.

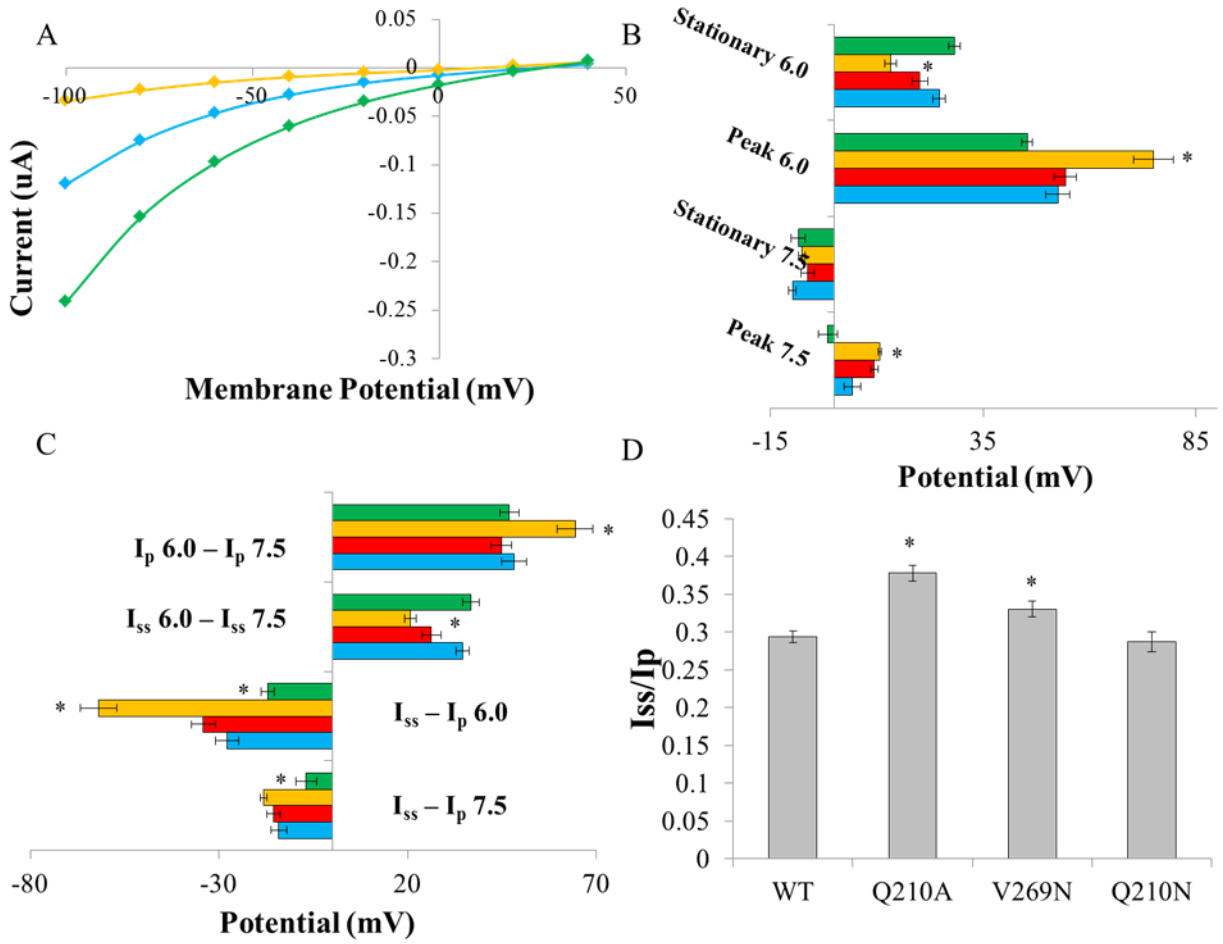

Figure 5.3.3 – Biophysical analysis of RHM mutants

(A) Current-voltage relationship of select RHM mutants. (B) Absolute reversal potentials determined at I_p and I_{ss} in Na^+ solutions at either pH 6.0 or 7.5. (C) Differences in E_{rev} determined as noted. (D) Steady-state to peak current ratios, which are a measure of ChR2 inactivation. Values are reported as the average ± SEM (n = 7-15). Statistically significant values are denoted with * ($p < 0.05$). WT – blue; Q210A – red; Q210N – green; V269N – orange.

	$I_p^{7.5}$	$I_{ss}^{7.5}$	$I_p^{6.0}$	$I_{ss}^{6.0}$	I_{ss}-$I_p^{7.5}$	I_{ss}-$I_p^{6.0}$	$I_{ss}^{6.0} - I_{ss}^{7.5}$	$I_p^{6.0} - I_p^{7.5}$
WT	4.30 ± 1.9	-9.84 ± 0.8	52.5 ± 2.7	24.6 ± 1.5	-14.1 ± 2.1	-27.8 ± 3.1	34.5 ± 1.7	48.2 ± 3.3
Q210A	9.39 ± 0.8	-6.20 ± 1.5	54.2 ± 2.6	20.1 ± 1.8	-15.6 ± 1.8	-34.1 ± 3.2	26.3 ± 2.4	44.8 ± 2.7
V269N	10.6 ± 0.4	-7.58 ± 0.7	75.0 ± 4.6*	13.2 ± 1.2*	-18.2 ± 0.8	-61.8 ± 4.8*	20.7 ± 1.4*	64.4 4.7*
Q210N	-1.55 ± 2.2	-8.5 ± 1.6	45.3 ± 1.2	28.2 ± 1.3	-6.9 ± 2.7*	-17.0 ± 1.8*	36.7 ± 2.1	46.9 ± 2.5

Table 5.3.1 – Summary of reversal potentials

The superscript denoted the pH of the solution used. Values are reported at the average ± SEM (n = 7-15). Statistically significant values are denoted with * ($p < 0.05$).

We also determined apparent rate constants for decay and off kinetics. Decay kinetics were calculated by fitting ChR2 photocurrent traces from I_p to I_{ss} with a monoexponential equation while off rates were calculated by fitting the portion of trace after light off with a biexponential equation (Figure 5.3.4A). V269N had the largest effect on decay kinetics, resulting in accelerated inactivation. Q210A and the null mutant Q210N had no significant effect on decay kinetics (Figure 5.3.4B). A similar trend was observed for off kinetics, with V269N having accelerated rates and both Q210 variants not significantly altering kinetics (Figure 5.3.4C).

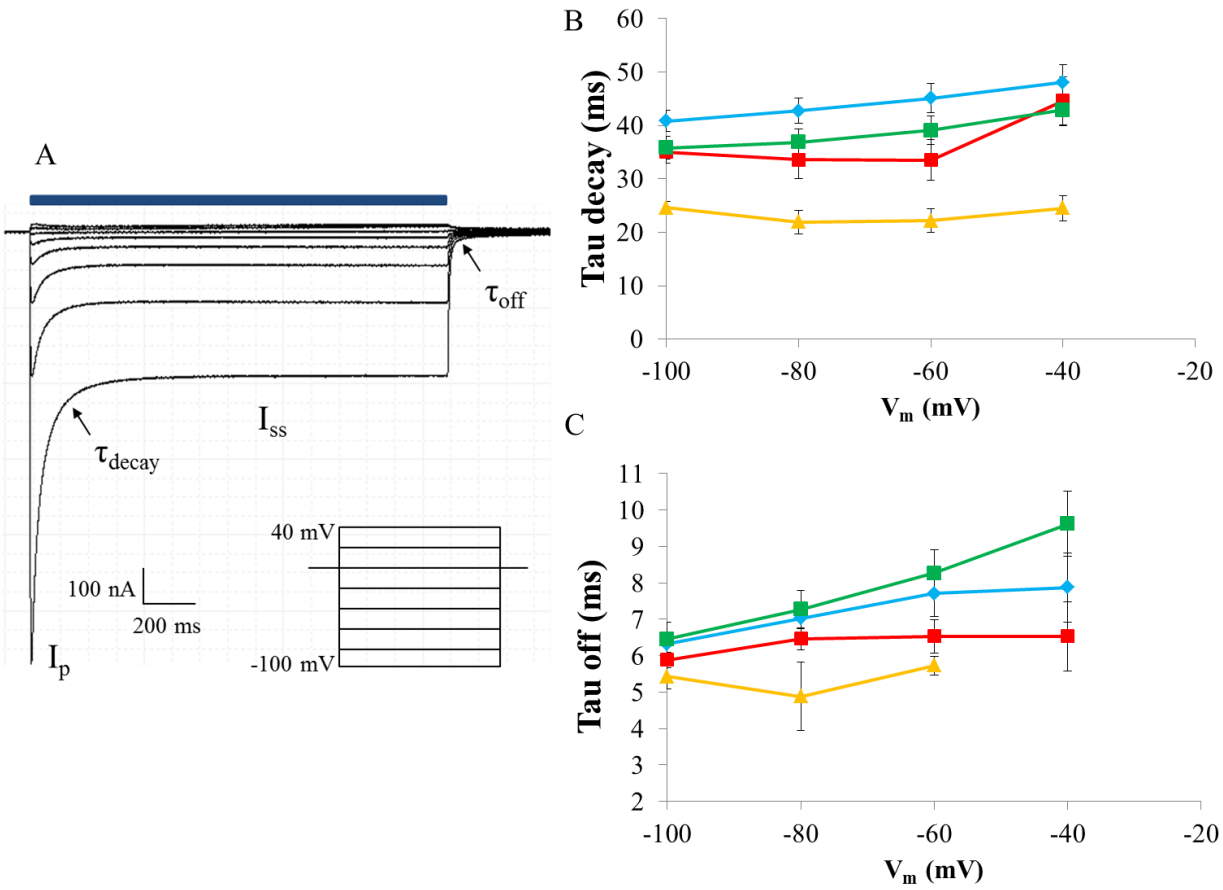

Figure 5.3.4 – Kinetics of RHM mutants

(A) Summary of exponential fitting of apparent rate constants. (B) Decay rate comparison of RHM and null ChR2 mutants. (C) Off rate comparison of RHM and null ChR2 mutants. Error bars represent the SEM (n = 7-15). WT – blue; Q210A – red; Q210N – green; V269N – orange.

Lastly, to determine how RHM modulates discrete transitions in the ChR2 photocycle, we applied a four-state kinetic model to fit experimental photocurrent traces. Theoretical fits were obtained by optimizing a set of 9 parameters describing rates of transition and fundamental properties of the channel (Figure 5.3.5) (see Materials and Methods). The null Q210N mutant had the least effect on our parameters compared to WT (Table 5.3.2). Only the transition from O1 to O2 was slightly accelerated for this mutant. Both V269N and Q210A saw the largest change

from the WT fits, having altered recovery and O2 -> O1 kinetics. Q210A also had a slower O2 to C2 rate while V269N had an accelerated O1 to O2 transition.

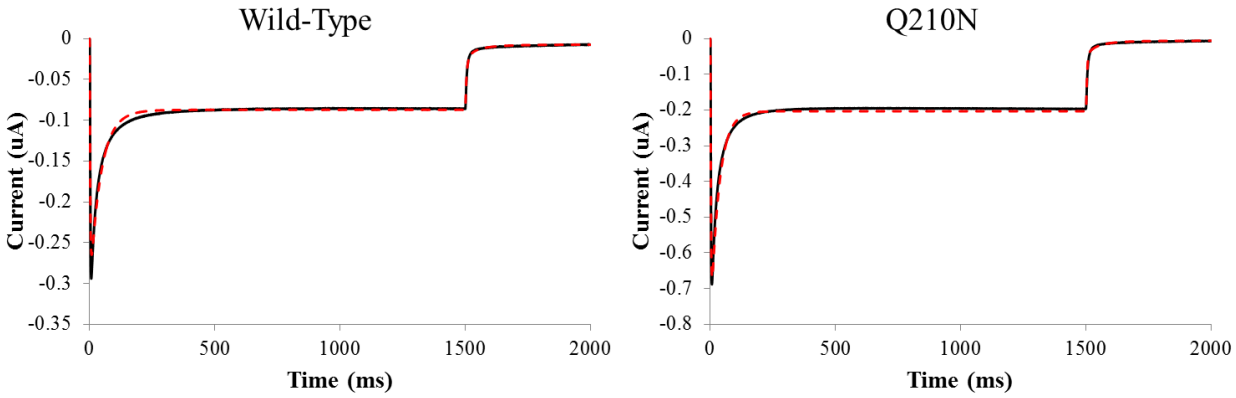

Figure 5.3.5 – Four-state photocycle theoretical fits
Theoretical fits were obtained by parameter optimization and objective function minimization as described in the Materials and Methods. Solid black line is the experimental average while the dashed red line is the average theoretical fit

-

	k_1	k_2	G_{d1} (ms^{-1})	G_{d2} (ms^{-1})	e_{12} (ms^{-1})	e_{21} (ms^{-1})	Imax	γ	G_r (ms^{-1})	T_{ChR2} (ms)
WT	0.26 ± 0.01	0.081 ± 0.01	0.24 ± 0.03	0.015 ± 0.005	0.038 ± 0.004	0.0057 ± 0.0004	0.57 ± 0.06	0.036 ± 0.007	0.0071 ± 0.001	0.73 ± 0.08
Q210A	0.30 ± 0.001	0.028 ± 0.007	0.16 ± 0.04	0.0055 ± 0.001*	0.036 ± 0.003	0.010 ± 0.001*	0.45 ± 0.08	0.050 ± 0.01	0.0093 ± 0.002*	0.61 ± 0.03
V269N	0.30 ± 0.002	0.037 ± 0.02	0.13 ± 0.05	0.006 ± 0.003	0.061 ± 0.009*	0.012 ± 0.001*	0.25 ± 0.05	0.035 ± 0.005	0.030 ± 0.01*	0.63 ± 0.2
Q210N	0.30 ± 0.03	0.058 ± 0.01	0.34 ± 0.03	0.013 ± 0.005	0.052 ± 0.002*	0.0067 ± 0.0006	1.7 ± 0.2	0.020 ± 0.004	0.0074 ± 0.001	1.45 ± 0.05

Table 5.3.2 - Summary of parameter optimization for the four-state photocycle model
Values are the average of parameters obtained from each cell ± SEM (n = 3-7). Statistically significant values are denoted with * ($p < 0.05$).

With the four-state model, we also explored the population of states at specific time points (Table 3). First, we determined the time at which each ChR2 construct reached peak current. Both Q210 variants were comparable to WT (8.0 ms), while V269N was accelerated (5.3 ms). Next, the population of O1 and O2 was evaluated at the time point that corresponded to I_p and also directly before the light was turned off at 1490 ms. Analysis of the two time points

revealed similar state populations for all mutants and the WT. The largest variation occurred for O1 at I_p where the RHM mutants Q210A and V269N had higher occupancy while the null Q210N mutant was lower.

State Population	WT	Q210A	V269N	Q210N
Time to Peak (ms)	8.0	7.7	5.3	7.3
O1 Peak	0.46	0.55	0.52	0.38
O2 Peak	0.09	0.10	0.11	0.09
O1 Stat	0.13	0.19	0.16	0.10
O2 Stat	0.65	0.61	0.67	0.65

Table 5.3.3 - State population comparison
The population of O1 and O2 were determined at specific time points as described in the text. Values are shown as a fraction of the maximum occupancy i.e. O1+O2+C1+C2 = 1.

5.4 Discussion

Combining molecular dynamics simulations, electrophysiology, and kinetic modeling, we quantified the functional effect of residual hydrophobic mismatch on ChR2. ChR2 undergoes large conformational changes during photoactivation which are crucial for the gating mechanism. We explored the contribution of the surrounding lipid environment on ChR2 dynamics by measuring the membrane deformation around the TM core. The membrane deformation does not fully eliminate hydrophobic mismatch in ChR2 and several residues remain exposed to unfavorable environments. The large energetic penalty associated with RHM was located at the cytoplasmic interface located between adjacent TMs 1/2, 6, and 7. This is especially interesting in the context of ChR2 gating because of the large helical movements of TMs 2 and 7 after photoexcitation. MD trajectories revealed the RHM penalty in WT ChR2 is associated with

water penetration into the membrane caused by thinning around the polar residues Q210 and Q73. As a result, V269 becomes exposed to a more polar environment.

The results of atomistic MD simulations provide a clear link between the structure-function-relationship at these positions. Mutation of V269 to asparagine reduces the hydrophobic mismatch and correlates with altered channel function. The measured reversal potentials for this mutant indicate severely reduced progressive ion selectivity, higher inactivation, and accelerated kinetics. Previously, we observed a similar effect at this position with the V269S mutant. V269S caused reduction in channel function, permeability, and pore size (57). It has been shown that this helix has a crucial role in the initial gating for ChR2 conductance. Upon photoisomerization, TM 7 undergoes significant reorientation and movement (64). Recent MD simulations comparing ATR and 13-cis retinal bound C1C2 structure revealed significant outward cytoplasmic bending of TM 7 (139). This is a common movement in microbial-rhodopsins that leads ion transport (105, 156). Moreover, a hydrophobic residue at this position is highly conserved in channelopsins. Our experimental results combined with previous data suggest the importance of hydrophobic mismatch at this position by a decrease in channel function. Our kinetic modeling parameterization also indicates a destabilization between the two open states compared to WT. There was also a reduction in quantum efficiency in the C2 -> O2 further supporting this notion. We propose that once the pore is formed, V269N becomes exposed to an unfavorable environment or allows for further water penetration exposing proximal hydrophobic residues resulting in the loss of function. This correlates with the conformational movement of TM 7 during pore formation and the influx in water prior to ion conductance (64, 65, 94).

Functionally similar was mutation of Q210 to alanine. Our computational results showed a larger reduction in the RHM penalty with Q210A. The primary reduction in energetic penalty was alleviating the mismatch in the membrane with hydrophobic alanine. Consequently, this removed the water penetration that V269 would be exposed to further lowering the RHM. Functionally, we observed a reduction in photocurrent, higher inactivation, and slightly accelerated decay kinetics. Although there was no change in selectivity under our experimental conditions, this is unsurprising as TM 4 does not contribute to the permeation pathway. This residue is also highly conserved among channelopsins and has a clear structural impact on ChR2 function as suggested by previous serine substitution (see Chapter 2). The kinetic parameters also indicated a similar destabilization of the open state preference to O2 and significantly reduced quantum efficiency of C2 -> O2 as in V269N. To test whether or not our results were a direct consequence of RHM, we created a null mutant at this position (Q210N), which we expected to have limited functional impact. Q210N has very similar photocurrents, reversal potentials, and kinetics. Our modeling also revealed very limited impact on kinetic parameters for this mutant.

We have shown that residual hydrophobic mismatch at the cytoplasmic interface in ChR2 has major implications on channel function. The energetic cost of residues in unfavorable environments can be reduced by polar/hydrophobic substitutions. The reduction of the RHM penalty in the closed state has deleterious effects on ChR2 conductance, selectivity, and open state stability. RHM appears to have the opposite effect on ChR2 compared to the bacterial transporter LeuT, where removal of RHM by the K288A mutant increases transport function nearly 5-fold (157). Nevertheless, ChR2 is a conformationally complex channel that it is highly

regulated by protein-lipid interactions. An open-state crystal structure will need to be resolved before the contribution of RHM to ChR2 structural dynamics can be fully elucidated.

ChR2 has been expressed in a variety of excitable cells including cardiomyocytes, CA1 pyramidal cells, and *Drosophila* motor neurons. The lipid composition across species and cell types varies greatly (158-160). As we have shown here, the residual exposure of ChR2 to unfavorable environments affects channel function. Moving forward, consideration should be given to lipid composition and the mutant ChR2 being used for optogenetics. A more targeted approach can be taken for engineering mutants that will favorably express/function depending on the cell line used.

6 Future Directions

6.1 *In vivo* incorporation of unnatural amino acids to probe channel electrostatics of aromatic residues

The functional role of aromatic residues within the TM domains of channels is difficult to determine. A major structural determinant of channel function is electrostatic cation-pi interactions, as shown in the ACh receptor (161). However, mutagenesis studies at these locations typically induce 'all or none' responses because there are only three canonical aromatic residues, each with different electrostatics and geometry. To overcome this challenge, we will incorporate non-canonical amino acids using nonsense suppression at putative cation-pi sites in ChR2.

ChR2 consists of several aromatic amino acids in the TM domains. Some of these residues are involved in lining the hydrophobic pocket surrounding retinal, while others appear to be involved in putative cation-pi interactions and facilitate TM packing. W124 appears to be involved in a putative cation-pi interaction and is critical for protein function. Analysis of our preliminary results reveals that mutation of W124 to phenylalanine or tyrosine has no observable photocurrent upon photoactivation (data not shown). We hypothesize that incorporating fluorine substituted tryptophan will deactivate the ring structure and reduce the cation-pi interaction. Progressive fluorination of the ring results in linear deactivation and therefore mono-, di-, or tri-substituted will reduce ChR2 function correspondingly (162). This strategy will provide quantitative information about structural dynamics without the need of an open state crystal structure.

6.2 Using ChR2 as a heavy metal channel to temporally induce oxidative stress

Cellular homeostasis of biometals is a highly regulated process critical for proper cell function (163). These heavy metals are required for a variety of catalytic processes that occur within the cell. Disturbing the equilibrium of metal ions can cause cytotoxicity through multiple pathways by generating reactive oxygen species (ROS) (163, 164). The inability of cells to reduce excess ROS induced by increased cellular metal concentration leads to oxidative stress. Oxidative stress is prevalent in many forms including oxidation of proteins, DNA, lipids, and other molecules affecting cell function (164-167). Although the initial and final steps of ROS induced cellular stress have been determined, the mechanisms and pathway of ROS release are not fully understood. Current methods of elucidating the pathway of increased biometals and ROS release are hindered by the lack of time resolution and controlled influx of metal. In this manner, ChR2 can be used as a tool to temporally monitor the release of ROS caused by the controlled influx of Cu^{2+} ions through the channel using a fluorescence-based technique in the model yeast system *Saccharomyces cerevisiae*.

We hypothesize that the influx of Cu^{2+} through ChR2 will release specific ROS that will cause oxidative stress and cytotoxicity through lipid peroxidation and oxidation of glutathione to glutathione disulfide. To test this hypothesis, we will initially quantify the amount of Cu^{2+} entering ChR2 expressing *S. cervissae* cells. ROS release will be temporally monitored using different commercially available ROS fluorescent probes. These probes, when oxidized by specific ROS, emit at characteristic wavelengths. This technique can further be extended using probes for *specific* ROS. Our experimental approach will not only elucidate the specific ROS released upon Cu^{2+} influx, but resolve the time course for ROS release. Lastly, we will use ChR2 to observe the downstream oxidative effects of Cu^{2+} induced ROS release. The initial

pathways of interest are lipid peroxidation and the oxidation of glutathione (GSH) to glutathione disulfide (GSSG). Excessive lipid peroxidation can lead to lipid damage and cell death while GSH reduction is used as a marker for cellular toxicity. Using ChR2 as a heavy metal channel will provide better temporal resolution in elucidating the discrete mechanisms and pathways involved in ROS release. Furthermore, the ability to express ChR2 cell specifically will allow for greater spatial resolution for specific pathways *in vivo*.

References

1. Foster, K. W., and R. D. Smyth. 1980. Light Antennas in phototactic algae. Microbiological reviews 44:572-630.
2. Treviranus, L. C. 1817. Vermischte Schriften anatomischen und physiologischen Inhalts. J.G. Heyse, Bremen.
3. Lenci, F., and G. Colombetti. 1978. Photobehavior of microorganisms: a biophysical approach. Annual review of biophysics and bioengineering 7:341-361.
4. Nagel, G., D. Ollig, M. Fuhrmann, S. Kateriya, A. M. Musti, E. Bamberg, and P. Hegemann. 2002. Channelrhodopsin-1: a light-gated proton channel in green algae. Science 296:2395-2398.
5. Nagel, G., T. Szellas, W. Huhn, S. Kateriya, N. Adeishvili, P. Berthold, D. Ollig, P. Hegemann, and E. Bamberg. 2003. Channelrhodopsin-2, a directly light-gated cation-selective membrane channel. Proc. Natl. Acad. Sci. USA 100:13940-13945.
6. Colegrave, N. 2002. Sex releases the speed limit on evolution. Nature 420:664-666.
7. Demurtas, O. C., S. Massa, P. Ferrante, A. Venuti, R. Franconi, and G. Giuliano. 2013. A Chlamydomonas-Derived Human Papillomavirus 16 E7 Vaccine Induces Specific Tumor Protection. Plos One 8.
8. Hille, B. 2001. Ion channels of excitable membranes. Sinauer, Sunderland, Mass.
9. Doyle, D. A. 2004. Structural changes during ion channel gating. Trends Neurosci. 27:298-302.
10. Beckstein, O., P. C. Biggin, P. Bond, J. N. Bright, C. Domene, A. Grottesi, J. Holyoake, and M. S. P. Sansom. 2003. Ion channel gating: insights via molecular simulations. FEBS Lett. 555:85-90.
11. Okita, N., N. Isogai, M. Hirono, R. Kamiya, and K. Yoshimura. 2005. Phototactic activity in Chlamydomonas 'non-phototactic' mutants deficient in Ca2+-dependent control of flagellar dominance or in inner-arm dynein. J. Cell Sci. 118:529-537.
12. Gadsby, D. C. 2009. Ion channels versus ion pumps: the principal difference, in principle. Nature Reviews Molecular Cell Biology 10:344-352.
13. Wietek, J., M. Broser, B. S. Krause, and P. Hegemann. 2016. Identification of a natural green light absorbing chloride conducting channelrhodopsin from Proteomonas sulcata. J. Biol. Chem.

14. Govorunova, E. G., O. A. Sineshchekov, R. Janz, X. Q. Liu, and J. L. Spudich. 2015. Natural light-gated anion channels: A family of microbial rhodopsins for advanced optogenetics. Science 349:647-650.
15. Humphrey, W., A. Dalke, and K. Schulten. 1996. VMD: Visual molecular dynamics. J. Mol. Graphics Model. 14:33-38.
16. Nikolic, K., N. Grossman, M. S. Grubb, J. Burrone, C. Toumazou, and P. Degenaar. 2009. Photocycles of channelrhodopsin-2. Photochem. Photobiol. 85:400-411.
17. Hegemann, P., S. Ehlenbeck, and D. Gradmann. 2005. Multiple Photocycles of Channelrhodopsin. Biophys. J 89:3911-3918.
18. Berndt, A., M. Prigge, D. Gradmann, and P. Hegemann. 2010. Two open states with progressive proton selectivities in the branched channelrhodopsin-2 photocycle. Biophys. J 98:753-761.
19. Stefanescu, R. A., R. G. Shivakeshavan, P. P. Khargonekar, and S. S. Talathi. 2013. Computational modeling of channelrhodopsin-2 photocurrent characteristics in relation to neural signaling. Bull. Math. Biol. 75:2208-2240.
20. Williams, J. C., J. Xu, Z. Lu, A. Klimas, X. Chen, C. M. Ambrosi, I. S. Cohen, and E. Entcheva. 2013. Computational optogenetics: empirically-derived voltage- and light-sensitive channelrhodopsin-2 model. PLoS Comp. Biol. 9:e1003220.
21. Grossman, N., K. Nikolic, C. Toumazou, and P. Degenaar. 2011. Modeling Study of the Light Stimulation of a Neuron Cell With Channelrhodopsin-2 Mutants. Ieee Transactions on Biomedical Engineering 58:1742-1751.
22. Bamann, C., T. Kirsch, G. Nagel, and E. Bamberg. 2008. Spectral Characteristics of the Photocycle of Channelrhodopsin-2 and Its Implication for Channel Function. J. Mol. Biol. 375:686-694.
23. Ernst, O. P., P. A. Sanchez Murcia, P. Daldrop, S. P. Tsunoda, S. Kateriya, and P. Hegemann. 2008. Photoactivation of channelrhodopsin. J. Biol. Chem. 283:1637-1643.
24. Radu, I., C. Bamann, M. Nack, G. Nagel, E. Bamberg, and J. Heberle. 2009. Conformational changes of channelrhodopsin-2. J. Am. Chem. Soc. 131:7313-7319.
25. Verhoefen, M.-K., C. Bamann, R. Blöcher, U. Förster, E. Bamberg, and J. Wachtveitl. 2010. The photocycle of channelrhodopsin-2: ultrafast reaction dynamics and subsequent reaction steps. Chemphyschem : a European journal of chemical physics and physical chemistry 11:3113-3122.
26. Lórenz-Fonfría, V. A., and J. Heberle. 2014. Channelrhodopsin unchained: structure and mechanism of a light-gated cation channel. Biochim. Biophys. Acta 1837:626.
27. Lórenz-Fonfría, V. A., T. Resler, N. Krause, M. Nack, M. Gossing, G. Fischer von Mollard, C. Bamann, E. Bamberg, R. Schlesinger, and J. Heberle. 2013. Transient protonation changes in channelrhodopsin-2 and their relevance to channel gating. Proc. Natl. Acad. Sci. USA 110:E1273-E1281.
28. Ritter, E., K. Stehfest, A. Berndt, P. Hegemann, and F. J. Bartl. 2008. Monitoring Light-induced Structural Changes of Channelrhodopsin-2 by UV-visible and Fourier Transform Infrared Spectroscopy. J. Biol. Chem. 283:35033-35041.
29. Eisenhauer, K., J. Kuhne, E. Ritter, A. Berndt, S. Wolf, E. Freier, F. Bartl, P. Hegemann, and K. Gerwert. 2012. In channelrhodopsin-2 Glu-90 is crucial for ion selectivity and is deprotonated during the photocycle. J. Biol. Chem. 287:6904-6911.
30. Luecke, H., H. T. Richter, and J. K. Lanyi. 1998. Proton transfer pathways in bacteriorhodopsin at 2.3 Angstrom resolution. Science 280:1934-1937.

31. Berndt, A., O. Yizhar, L. A. Gunaydin, P. Hegemann, and K. Deisseroth. 2009. Bi-stable neural state switches. Nat. Neurosci. 12:229-234.
32. Sineshchekov, O. A., E. G. Govorunova, J. Wang, H. Li, and J. L. Spudich. 2013. Intramolecular proton transfer in channelrhodopsins. Biophys. J 104:807-817.
33. Kato, H. E., F. Zhang, O. Yizhar, C. Ramakrishnan, T. Nishizawa, K. Hirata, J. Ito, Y. Aita, T. Tsukazaki, S. Hayashi, P. Hegemann, A. D. Maturana, R. Ishitani, K. Deisseroth, and O. Nureki. 2012. Crystal structure of the channelrhodopsin light-gated cation channel. Nature 482:369-374.
34. Gunaydin, L. A., O. Yizhar, A. Berndt, V. S. Sohal, K. Deisseroth, and P. Hegemann. 2010. Ultrafast optogenetic control. Nat. Neurosci. 13:387-392.
35. Heberle, J., D. Oesterhelt, and N. A. Dencher. 1993. Decoupling of photo-cycle and proton cycle in the Asp85- Glu mutant of bacteriorhodopsin. Embo Journal 12:3721-3727.
36. Popot, J. L., and D. M. Engelman. 1990. Membrane protein folding and oligomerization: the two-stage model. Biochemistry 29:4031-4037.
37. Dawson, J. P., J. S. Weinger, and D. M. Engelman. 2002. Motifs of serine and threonine can drive association of transmembrane helices1. J. Mol. Biol. 316:799-805.
38. Adamian, L., R. Jackups, T. A. Binkowski, and J. Liang. 2003. Higher-order Interhelical Spatial Interactions in Membrane Proteins. J. Mol. Biol. 327:251-272.
39. Jayasinghe, S., K. Hristova, and S. H. White. 2001. Energetics, stability, and prediction of transmembrane helices. J. Mol. Biol. 312:927-934.
40. Fleming, K. G., A. L. Ackerman, and D. M. Engelman. 1997. The effect of point mutations on the free energy of transmembrane alpha-helix dimerization. J. Mol. Biol. 272:266-275.
41. Bamann, C., R. Gueta, S. Kleinlogel, G. Nagel, and E. Bamberg. 2010. Structural guidance of the photocycle of channelrhodopsin-2 by an interhelical hydrogen bond. Biochemistry 49:267-278.
42. Stehfest, K., E. Ritter, A. Berndt, F. Bartl, and P. Hegemann. 2010. The branched photocycle of the slow-cycling channelrhodopsin-2 mutant C128T. J. Mol. Biol. 398:690-702.
43. Peralvarez-Marin, A., M. Marquez, J. L. Bourdelande, E. Querol, and E. Padros. 2004. Thr-90 Plays a Vital Role in the Structure and Function of Bacteriorhodopsin. J. Biol. Chem. 279:16403-16409.
44. Ihara, K., T. Umemura, I. Katagiri, T. Kitajima-Ihara, Y. Sugiyama, Y. Kimura, and Y. Mukohata. 1999. Evolution of the Archaeal Rhodopsins: Evolution Rate Changes by Gene Duplication and Functional Differentiation. J. Mol. Biol. 285:163-163.
45. Nack, M., I. Radu, M. Gossing, C. Bamann, E. Bamberg, G. F. von Mollard, and J. Heberle. 2010. The DC gate in Channelrhodopsin-2: crucial hydrogen bonding interaction between C128 and D156. Photochemical & Photobiological Sciences 9:194-198.
46. Watanabe, H. C., K. Welke, F. Schneider, S. Tsunoda, F. Zhang, K. Deisseroth, P. Hegemann, and M. Elstner. 2012. Structural Model of Channelrhodopsin. J. Biol. Chem. 287:7456-7466.
47. Watanabe, H. C., K. Welke, D. J. Sindhikara, P. Hegemann, and M. Elstner. 2013. Towards an understanding of channelrhodopsin function: simulations lead to novel insights of the channel mechanism. J. Mol. Biol. 425:1795-1814.

48. Alexej, D., N. Georg, J. K. Robert, G. Ronnie, L. Dmitrij, U. Sybille, H. Moritz, E. Nadine, G. Shiqiang, F. André, and L. Tobias. 2014. Channelrhodopsin-2–XXL, a powerful optogenetic tool for low-light applications. Proceedings of the National Academy of Sciences 111:13972-13977.
49. Alex, P. l.-M. n., M. r. Mercedes, B. JosÃ©-Luis, Q. Enric, and P. s. Esteve. 2004. Thr-90 Plays a Vital Role in the Structure and Function of Bacteriorhodopsin. J. Biol. Chem. 279:16403-16409.
50. Cohen, J., and K. Schulten. 2004. Mechanism of Anionic Conduction across ClC. Biophys. J 86:836-845.
51. Accardi, A., and C. Miller. 2004. Secondary active transport mediated by a prokaryotic homologue of ClC Cl- channels. Nature 427:803-807.
52. Feng, L., E. B. Campbell, and R. MacKinnon. 2012. Molecular mechanism of proton transport in CLC Cl-/H+ exchange transporters. P Natl Acad Sci USA 109:11699-11704.
53. Lisal, J., and M. Maduke. 2008. The ClC-0 chloride channel is a 'broken' Cl(-)/H(+) antiporter. Nature Structural & Molecular Biology 15:805-810.
54. Feldbauer, K., D. Zimmermann, V. Pintschovius, J. Spitz, C. Bamann, and E. Bamberg. 2009. Channelrhodopsin-2 is a leaky proton pump. P Natl Acad Sci USA 106:12317-12322.
55. Nack, M., I. Radu, B.-J. Schultz, T. Resler, R. Schlesinger, A.-N. Bondar, C. del Val, S. Abbruzzetti, C. Viappiani, C. Bamann, E. Bamberg, and J. Heberle. 2012. Kinetics of proton release and uptake by channelrhodopsin-2. FEBS Lett. 586:1344-1348.
56. Grzesiek, S., and N. A. Dencher. 1986. Time-course and stoichiometry of light-induced proton release and uptake during the photocycle of bacteriorhodopsin. FEBS Lett. 208:337-342.
57. Richards, R., and R. E. Dempski. 2012. Re-introduction of transmembrane serine residues reduce the minimum pore diameter of channelrhodopsin-2. PloS One 7:e50018.
58. Ruffert, K., B. Himmel, D. Lall, C. Bamann, E. Bamberg, H. Betz, and V. Eulenburg. 2011. Glutamate residue 90 in the predicted transmembrane domain 2 is crucial for cation flux through channelrhodopsin 2. Biochem. Biophys. Res. Commun. 410:737-743.
59. Schneider, F., D. Gradmann, and P. Hegemann. 2013. Ion selectivity and competition in channelrhodopsins. Biophysical journal 105:91-100.
60. Wietek, J., J. S. Wiegert, N. Adeishvili, F. Schneider, H. Watanabe, S. P. Tsunoda, A. Vogt, M. Elstner, T. G. Oertner, and P. Hegemann. 2014. Conversion of channelrhodopsin into a light-gated chloride channel. Science 344:409-412.
61. Gaiko, O., and R. E. Dempski. 2013. Transmembrane domain three contributes to the ion conductance pathway of channelrhodopsin-2. Biophys. J 104:1230-1237.
62. Gradmann, D., A. Berndt, F. Schneider, and P. Hegemann. 2011. Rectification of the channelrhodopsin early conductance. Biophys. J 101:1057-1068.
63. Mueller, M., C. Bamann, E. Bamberg, and W. Kuehlbrandt. 2011. Projection structure of channelrhodopsin-2 at 6 angstrom resolution by electron crystallography. J. Mol. Biol. 414:86-95.
64. Muller, M., C. Bamann, E. Bamberg, and W. Kuhlbrandt. 2015. Light-induced helix movements in channelrhodopsin-2. J. Mol. Biol. 427:341-349.
65. Lorenz-Fonfria, V. A., C. Bamann, T. Resler, R. Schlesinger, E. Bamberg, and J. Heberle. 2015. Temporal evolution of helix hydration in a light-gated ion channel correlates with ion conductance. Proc. Natl. Acad. Sci. USA 112:E5796-E5804.

66. Hou, S.-Y., E. G. Govorunova, M. Ntefidou, C. E. Lane, E. N. Spudich, O. A. Sineshchekov, and J. L. Spudich. 2012. Diversity of Chlamydomonas channelrhodopsins. Photochem. Photobiol. 88:119-128.
67. Klapoetke, N. C., Y. Murata, S. S. Kim, S. R. Pulver, A. Birdsey-Benson, Y. K. Cho, T. K. Morimoto, A. S. Chuong, E. J. Carpenter, Z. Tian, J. Wang, Y. Xie, Z. Yan, Y. Zhang, B. Y. Chow, B. Surek, M. Melkonian, V. Jayaraman, M. Constantine-Paton, G. K.-S. Wong, and E. S. Boyden. 2014. Independent optical excitation of distinct neural populations. Nat. Methods 11:338-346.
68. Lasogga, L., W. Rettig, H. Otto, I. Wallat, and J. Bricks. 2010. Model systems for the investigation of the opsin shift in bacteriorhodopsin. The journal of physical chemistry. A 114:2179-2188.
69. Govorunova, E. G., O. A. Sineshchekov, H. Li, R. Janz, and J. L. Spudich. 2013. Characterization of a highly efficient blue-shifted channelrhodopsin from the marine alga Platymonas subcordiformis. The Journal of biological chemistry 288:29911-29922.
70. Scholz, F., E. Bamberg, C. Bamann, and J. Wachtveitl. 2012. Tuning the primary reaction of channelrhodopsin-2 by imidazole, pH, and site-specific mutations. Biophys. J 102:2649-2657.
71. Prigge, M., F. Schneider, S. P. Tsunoda, C. Shilyansky, J. Wietek, K. Deisseroth, and P. Hegemann. 2012. Color-tuned channelrhodopsins for multiwavelength optogenetics. The Journal of biological chemistry 287:31804-31812.
72. Tromberg, B. J., N. Shah, R. Lanning, A. Cerussi, J. Espinoza, T. Pham, L. Svaasand, and J. Butler. 2000. Non-invasive in vivo characterization of breast tumors using photon migration spectroscopy. Neoplasia 2:26-40.
73. Lin, J. Y., P. M. Knutsen, A. Muller, D. Kleinfeld, and R. Y. Tsien. 2013. ReaChR: a red-shifted variant of channelrhodopsin enables deep transcranial optogenetic excitation. Nat. Neurosci. 16:1499-1499.
74. Boyden, E. S., F. Zhang, E. Bamberg, G. Nagel, and K. Deisseroth. 2005. Millisecond-timescale, genetically-targeted optical control of neural activity. Nat. Neurosci. 8:1263-1268.
75. Ishizuka, T., M. Kakuda, R. Araki, and H. Yawo. 2006. Kinetic evaluation of photosensitivity in genetically engineered neurons expressing green algae light-gated channels. Neuroscience Research 54:85-94.
76. Li, X., D. V. Gutierrez, M. G. Hanson, J. Han, M. D. Mark, H. Chiel, P. Hegemann, L. T. Landmesser, and S. Herlitze. 2005. Fast noninvasive activation and inhibition of neural and network activity by vertebrate rhodopsin and green algae channelrhodopsin. Proc Natl Acad Sci USA 102:17816-17821.
77. Nagel, G., M. Brauner, J. F. Liewald, N. Adeishvili, E. Bamberg, and A. Gottschalk. 2005. Light activation of Channelrhodopsin-2 in excitable cells of Caenorhabditis elegans triggers rapid behavioral responses. Curr. Biol. 15:2279-2284.
78. Bi, A., J. Cui, Y. P. Ma, E. Olshevskaya, M. Pu, A. M. Dizhoor, and Z. H. Pan. 2006. Ectopic Expression of a Microbial-Type Rhodopsin Restores Visual Responses in Mice with Photoreceptor Degeneration. Neuron 50:23-33.
79. Schroll, C., T. Riemensperger, D. Bucher, J. Ehmer, T. Voller, K. Erguth, B. Gerber, T. Hendel, G. Nagel, E. Buchner, and A. Fiala. 2006. Light-Induced Activation of Distinct Modulatory Neurons Triggers Appetitive or Adversive Learning in Drosopphila Larvae. Curr. Biol. 16:1741-1747.

80. Zhang, Y. P., and T. G. Oertner. 2007. Optical induction of synaptic plasticity using a light-sensitive channel. Nat Methods 4:139-141.
81. Huber, D., L. Petreanu, N. Ghitani, S. Ranade, T. Hromadka, Z. Mainen, and K. Svoboda. 2008. Sparse optical microstimulation in barrel cortex drives learned behaviour in freely moving mice. Nature 451:61-64.
82. Petreanu, L., D. Huber, A. Sobczyk, and Svoboda. 2007. Channelrhodopsin-2-assisted circuit mapping of long range callosal projections. Nat Neurosci 10:663-668.
83. Adamantidis, A., F. Zhang, A. M. Aravanis, K. Deisseroth, and L. de Lecea. 2007. Neural substrates of awakenign probed with optogenetic control of hypocretin neurons. Nature 450:420-424.
84. Zhang, F., M. Prigge, F. Beyriere, S. P. Tsunoda, J. Mattis, O. Yizhar, P. Hegemann, and K. Deisseroth. 2008. Red-shifted optogenetic excitation: a tool for fast neural control derived from Volvox carteri. Nat Neurosci 11:631-633.
85. Kleinlogel, S., K. Feldbauer, R. E. Dempski, H. Fotis, P. G. Wood, C. Bamann, and E. Bamberg. 2011. Ultra light-sensitive and fast neuronal activation with the Ca(2)+-permeable channelrhodopsin CatCh. Nature neuroscience 14:513-518.
86. Karathanos, T. V., P. M. Boyle, and N. A. Trayanova. 2014. Optogenetics-enabled dynamic modulation of action potential duration in atrial tissue: feasibility of a novel therapeutic approach. Europace : European pacing, arrhythmias, and cardiac electrophysiology : journal of the working groups on cardiac pacing, arrhythmias, and cardiac cellular electrophysiology of the European Society of Cardiology 16 Suppl 4:iv69-iv76.
87. Park, S. A., S. R. Lee, L. Tung, and D. T. Yue. 2014. Optical mapping of optogenetically shaped cardiac action potentials. Scientific reports 4:6125.
88. Ambrosi, C. M., A. Klimas, J. Yu, and E. Entcheva. 2014. Cardiac applications of optogenetics. Progress in biophysics and molecular biology 115:294-304.
89. Dawydow, A., R. Gueta, D. Ljaschenko, S. Ullrich, M. Hermann, N. Ehmann, S. Gao, A. Fiala, T. Langenhan, G. Nagel, and R. J. Kittel. 2014. Channelrhodopsin-2-XXL, a powerful optogenetic tool for low-light applications. P Natl Acad Sci USA 111:13972-13977.
90. Spencer, R. H., and D. C. Rees. 2002. The alpha-helix and the organization and gating of channels. Annual Review of Biophysics and Biomolecular Structure 31:207-233.
91. Gray, T. M., and B. W. Matthews. 1984. Intrahelical hydrogen bonding of serine, threonine and cysteine residues within alpha-helices and its relevance to membrane-bound proteins. J. Mol. Biol. 175:75-81.
92. Ballesteros, J. A., X. Deupi, M. Olivella, E. E. Haaksma, and L. Pardo. 2000. Serine and threonine residues bend alpha-helices in the chi(1) = g(-) conformation. Biophys. J 79:2754-2760.
93. Lanyi, J. K. 2004. Bacteriorhodopsin. Annu Rev Physiol 66:665-688.
94. Sattig, T., C. Rickert, E. Bamberg, H. J. Steinhoff, and C. Bamann. 2013. Light-induced movement of the transmembrane HelixB in channelrhodopsin-2. Angew. Chem. 52:9705-9708.
95. Marti, T., H. Otto, T. Mogi, R. S.J, M. P. Heyn, and H. G. Khorana. 1991. Bacteriorhodopsin mutants containing single substitutions of serine or threonine residues are all active in proton translocation. J. Biol. Chem. 266:6919-6927.

96. Payandeh, J., T. Scheuer, N. Zheng, and W. A. Catterall. 2011. The crystal structure of a voltage-gated sodium channel. Nature 475:353-U104.
97. Cohen, B. N., C. Labarca, N. Davidson, and H. A. Lester. 1992. Mutations in M2 Alter the Selectivity of the Mouse Nicotinic Acetylcholine-Receptor for Organic and Alkali-Metal Cations. J. Gen. Physiol. 100:373-400.
98. Hille, B. 1973. Potassium Channels in Myelinated Nerve: Selective permeability to small cations. The Journal of General Physiology 61:669-686.
99. Richards, R., and R. E. Dempski. 2011. Examining the Conformational Dynamics of Membrane Proteins in situ with Site-directed Fluorescence Labeling. Jove-J Vis Exp.
100. Durr, K. L., N. N. Tavraz, D. Zimmermann, E. Bamberg, and T. Friedrich. 2008. Characterization of Na,K-ATPase and H,K-ATPase enzymes with glycosylation-deficient beta-subunit variants by voltage-clamp fluorometry in Xenopus oocytes. Biochemistry 47:4288-4297.
101. Kamsteeg, E. J., and P. M. T. Deen. 2001. Detection of aquaporin-2 in the plasma membranes of oocytes: A novel isolation method with improved yield and purity. Biochem. Biophys. Res. Commun. 282:683-690.
102. McKinnon, N. K., D. C. Reeves, and M. H. Akabas. 2011. 5-HT3 receptor ion size selectivity is a property of the transmembrane channel, not the cytoplasmic vestibule portals. The Journal of general physiology 138:453-466.
103. Hille, B. 1972. The Permeability of the Sodium Channel to Metal Cations in Myelinated Nerve. The Journal of General Physiology 59:637-658.
104. Angela, N. E., B. Amy, C. Debra, A. L. Henry, and S. K. Baljit. 2002. Control of P2X2 channel permeability by thye cytosolic domain. The Journal of General Physiology 120:119.
105. Radzwill, N., K. Gerwert, and H. J. Steinhoff. 2001. Time-resolved detection of transient movement of helices F and G in doubly spin-labeled bacteriorhodopsin. Biophys. J 80:2856-2866.
106. Berndt, A., P. Schoenenberger, J. Mattis, K. M. Tye, K. Deisseroth, P. Hegemann, and T. G. Oertner. 2011. High-efficiency channelrhodopsins for fast neuronal stimulation at low light levels. P Natl Acad Sci USA 108:7595-7600.
107. Gregoret, L. M., S. D. Rader, R. J. Fletterick, and F. E. Cohen. 1991. Hydrogen-Bonds Involving Sulfur-Atoms in Proteins. Proteins 9:99-107.
108. Smart, O. S., J. Breed, G. R. Smith, and M. S. P. Sansom. 1997. A novel method for structure-based prediction of ion channel conductance properties. Biophys. J 72:1109-1126.
109. Roberts, J. A., and R. J. Evans. 2007. Cysteine substitution mutants give structural insight and identify ATP binding and activation sites at P2X receptors. J. Neurosci. 27:4072-4082.
110. Chaves, L. A. P., and D. C. Gadsby. 2015. Cysteine accessibility probes timing and extent of NBD separation along the dimer interface in gating CFTR channels. The Journal of General Physiology 145:261-283.
111. Akabas, M. H., D. A. Stauffer, M. Xu, and A. Karlin. 1992. Acetylcholine-receptor channel structure probed in cysteine-substitution mutants. Science 258:307-310.
112. Goldschen-Ohm, M. P., D. L. Capes, K. M. Oelstrom, and B. Chanda. 2013. Multiple pore conformations driven by asynchronous movements of voltage sensors in a eukaryotic sodium channel. Nat Commun 4:1350.

113. Kuhne, J., K. Eisenhauer, E. Ritter, P. Hegemann, K. Gerwert, and F. Bartl. 2014. Early formation of the ion-conducting pore in channelrhodopsin-2. Angew. Chem.:4953–4957.
114. Krause, N., C. Engelhard, J. Heberle, R. Schlesinger, and R. Bittl. 2013. Structural differences between the closed and open states of channelrhodopsin-2 as observed by EPR spectroscopy. FEBS Lett. 587:3309-3313.
115. Berndt, A., S. Y. Lee, C. Ramakrishnan, and K. Deisseroth. 2014. Structure-guided transformation of channelrhodopsin into a light-activated chloride channel. Science 344:420-424.
116. Kiefer, F., K. Arnold, M. Kunzli, L. Bordoli, and T. Schwede. 2009. The SWISS-MODEL Repository and associated resources. Nucleic Acids Res. 37:D387-392.
117. Arnold, K., L. Bordoli, J. Kopp, and T. Schwede. 2006. The SWISS-MODEL workspace: a web-based environment for protein structure homology modelling. Bioinformatics 22:195-201.
118. Peitsch, M. C. 1995. Protein modeling by email. Nat. Biotechnol. 13:658-660.
119. Zhou, F., A. Windemuth, and K. Schulten. 1993. Molecular dynamics study of the proton pump cycle of bacteriorhodopsin. Biochemistry 32:2291-2306.
120. Tajkhorshid, E., B. Paizs, and S. Suhai. 1997. Conformational effects on the proton affinity of the Schiff base in bacteriorhodopsin: A density functional study. J. Phys. Chem. B 101:8021-8028.
121. Tajkhorshid, E., and S. Suhai. 1999. Influence of the Methyl Groups on the Structure, Charge Distribution, and Proton Affinity of the Retinal Schiff Base. J. Phys. Chem. B 103:5581-5590.
122. Tajkhorshid, E., J. Baudry, K. Schulten, and S. Suhai. 2000. Molecular dynamics study of the nature and origin of retinal's twisted structure in bacteriorhodopsin. Biophys. J 78:683-693.
123. Baudry, J., S. Crouzy, B. Roux, and J. C. Smith. 1997. Quantum chemical and free energy simulation analysis of retinal conformational energetics. J. Chem. Inform. Comput. Sci. 37:1018-1024.
124. Nina, M., B. Roux, and J. C. Smith. 1995. Functional interactions in bacteriorhodopsin: a theoretical analysis of retinal hydrogen bonding with water. Biophys. J 68:25-39.
125. Phillips, J. C., K. Schulten, R. Braun, W. Wang, J. Gumbart, E. Tajkhorshid, E. Villa, C. Chipot, R. D. Skeel, and L. Kalé. 2005. Scalable molecular dynamics with NAMD. J. Comput. Chem. 26:1781-1802.
126. Foloppe, N., and J. A. D. MacKerell. 2000. All-atom empirical force field for nucleic acids: I. Parameter optimization based on small molecule and condensed phase macromolecular target data. J. Comput. Chem. 21:86-104.
127. MacKerell, A. D., and N. K. Banavali. 2000. All-atom empirical force field for nucleic acids: II. Application to molecular dynamics simulations of DNA and RNA in solution. J. Comput. Chem. 21:105-120.
128. Huang, X. Q., and W. Miller. 1991. A Time-Efficient, Linear-Space Local Similarity Algorithm. Adv Appl Math 12:337-357.
129. Lovell, S. C., I. W. Davis, W. B. Adrendall, P. I. W. de Bakker, J. M. Word, M. G. Prisant, J. S. Richardson, and D. C. Richardson. 2003. Structure validation by C alpha geometry: phi,psi and C beta deviation. Proteins 50:437-450.
130. Green, W. N., and O. S. Andersen. 1991. Surface-charges and ion channel function. Annu Rev Physiol 53:341-359.

131. Nagano, N., M. Ota, and K. Nishikawa. 1999. Strong hydrophobic nature of cysteine residues in proteins. FEBS Lett. 458:69-71.
132. Isralewitz, B., J. Baudry, J. Gullingsrud, D. Kosztin, and K. Schulten. 2001. Steered molecular dynamics investigations of protein function. J. Mol. Graphics Model. 19:13-25.
133. Park, S., and K. Schulten. 2004. Calculating potentials of mean force from steered molecular dynamics simulations. J Chem Phys 120:5946-5961.
134. Kosztin, D., S. Izrailev, and K. Schulten. 1999. Unbinding of retinoic acid from its receptor studied by steered molecular dynamics. Biophys. J 76:188-197.
135. Jensen, M. Ø., S. Park, E. Tajkhorshid, and K. Schulten. 2002. Energetics of glycerol conduction through aquaglyceroporin GlpF. Proc. Natl. Acad. Sci. USA 99:6731-6736.
136. Gullingsrud, J., and K. Schulten. 2003. Gating of MscL studied by steered molecular dynamics. Biophys. J 85:2087-2099.
137. Kleinlogel, S., K. Feldbauer, R. E. Dempski, H. Fotis, P. G. Wood, C. Bamann, and E. Bamberg. 2011. Ultra light-sensitive and fast neuronal activation with the Ca2+-permeable channelrhodopsin CatCh. Nat. Neurosci. 14:513-518.
138. Richards, R., and R. E. Dempski. 2015. Cysteine substitution and labeling provide insight into channelrhodopsin-2 ion conductance. Biochemistry 54:5665-5668.
139. Takemoto, M., H. E. Kato, M. Koyama, J. Ito, M. Kamiya, S. Hayashi, A. D. Maturana, K. Deisseroth, R. Ishitani, and O. Nureki. 2015. Molecular dynamics of channelrhodopsin at the early stages of channel opening. Plos One 10.
140. Cui, Y. B., and D. A. Bastien. 2011. Water transport in human aquaporin-4: Molecular dynamics (MD) simulations. Biochem. Biophys. Res. Commun. 412:654-659.
141. Talathi, S. S., P. R. Carney, and P. P. Khargonekar. 2011. Control of neural synchrony using channelrhodopsin-2: a computational study. J. Comput. Biol. 31:87-103.
142. Shi, L., M. Quick, Y. F. Zhao, H. Weinstein, and J. A. Javitch. 2008. The mechanism of a neurotransmitter : sodium symporter - Inward release of Na+ and substrate is triggered by substrate in a second binding site. Mol. Cell 30:667-677.
143. Watanabe, H. C., K. Welke, F. Schneider, S. Tsunoda, F. Zhang, K. Deisseroth, P. Hegemann, and M. Elstner. 2012. Structural model of channelrhodopsin. The Journal of biological chemistry 287:7456-7466.
144. Isralewitz, B., M. Gao, and K. Schulten. 2001. Steered molecular dynamics and mechanical functions of proteins. Current Opinion in Structural Biology 11:224-230.
145. Schneider, F., D. Gradmann, and P. Hegemann. 2013. Ion selectivity and competition in channelrhodopsins. Biophys. J 105:91.
146. Johannsson, A., G. A. Smith, and J. C. Metcalfe. 1981. The effect of bilayer thickness on the activity of (Na+ + K+)-ATPase. Biochim. Biophys. Acta 641:416-421.
147. Andersen, O. S., and R. E. Koeppe. 2007. Bilayer Thickness and Membrane Protein Function: An Energetic Perspective. Annual Review of Biophysics and Biomolecular Structure 36:107-130.
148. Botelho, A. V., T. Huber, T. P. Sakmar, and M. F. Brown. 2006. Curvature and Hydrophobic Forces Drive Oligomerization and Modulate Activity of Rhodopsin in Membranes. Biophys. J 91:4464-4477.
149. Huang, H. W. 1986. Deformation free energy of bilayer membrane and its effect on gramicidin channel lifetime. Biophys. J 50:1061-1070.

150. Mondal, S., G. Khelashvili, J. Shan, Olaf S. Andersen, and H. Weinstein. 2011. Quantitative Modeling of Membrane Deformations by Multihelical Membrane Proteins: Application to G-Protein Coupled Receptors. Biophys. J 101:2092-2101.
151. Mondal, S., G. Khelashvili, L. Shi, and H. Weinstein. 2013. The cost of living in the membrane: A case study of hydrophobic mismatch for the multi-segment protein LeuT. Chemistry and Physics of Lipids 169:27-38.
152. Boyden, E. S., F. Zhang, E. Bamberg, G. Nagel, and K. Deisseroth. 2005. Millisecond-timescale, genetically targeted optical control of neural activity. Nat. Neurosci. 8:1263-1268.
153. Zhang, F., L.-P. Wang, E. S. Boyden, and K. Deisseroth. 2006. Channelrhodopsin-2 and optical control of excitable cells. Nat. Methods 3:785-792.
154. Arenkiel, B. R., J. Peca, I. G. Davison, C. Feliciano, K. Deisseroth, G. J. Augustine, M. D. Ehlers, and G. P. Feng. 2007. In vivo light-induced activation of neural circuitry in transgenic mice expressing channelrhodopsin-2. Neuron 54:205-218.
155. Douglass, A. D., S. Kraves, K. Deisseroth, A. F. Schier, and F. Engert. 2008. Escape behavior elicited by single, Channelrhodopsin-2-evoked spikes in zebrafish somatosensory neurons. Curr. Biol. 18:1133-1137.
156. Nakanishi, T., S. Kanada, M. Murakami, K. Ihara, and T. Kouyama. 2013. Large Deformation of Helix F during the Photoreaction Cycle of Pharaonis Halorhodopsin in Complex with Azide. Biophys. J 104:377-385.
157. Piscitelli, C. L., H. Krishnamurthy, and E. Gouaux. 2010. Neurotransmitter/sodium symporter orthologue LeuT has a single high–affinity substrate site. Nature 468:1129-1132.
158. Jones, H. E., J. L. Harwood, I. D. Bowen, and G. Griffiths. 1992. Lipid composition of subcellular membranes from larvae and prepupae of Drosophila melanogaster. Lipids 27:984-987.
159. Norton, W. T., T. Abe, S. E. Poduslo, and G. H. DeVries. 1975. The lipid composition of isolated brain cells and axons. J. Neurosci. Res. 1:57-75.
160. Hamazaki, K., and H.-Y. Kim. 2013. Differential modification of the phospholipid profile by transient ischemia in rat hippocampal CA1 and CA3 regions. Prostaglandins, leukotrienes, and essential fatty acids 88:299-306.
161. Zhong, W. G., J. P. Gallivan, Y. O. Zhang, L. T. Li, H. A. Lester, and D. A. Dougherty. 1998. From ab initio quantum mechanics to molecular neurobiology: A cation-pi binding site in the nicotinic receptor. P Natl Acad Sci USA 95:12088-12093.
162. Dougherty, D. A., and E. B. Van Arnam. 2014. In Vivo Incorporation of non-canonical amino acids by using the chemical aminoacylation strategy: A broadly applicable mechanistic tool. ChemBioChem 15:1710-1720.
163. Bleackley, M. R., and R. T. A. Macgillivray. 2011. Transition metal homeostasis: from yeast to human disease. Biometals : an international journal on the role of metal ions in biology, biochemistry, and medicine 24:785-809.
164. Shanmuganathan, A., S. V. Avery, S. A. Willetts, and J. E. Houghton. 2004. Copper-induced oxidative stress in Saccharomyces cerevisiae targets enzymes of the glycolytic pathway. FEBS Lett. 556:253-259.
165. Thannickal, V. J., and B. L. Fanburg. 2000. Reactive oxygen species in cell signaling. AJP - Lung Cellular and Molecular Physiology 279:1005-L1028.

166. Niki, E., Y. Yoshida, Y. Saito, and N. Noguchi. 2005. Lipid peroxidation: mechanisms, inhibition, and biological effects. Biochem. Biophys. Res. Commun. 338:668-676.
167. Liang, Q., and B. Zhou. 2007. Copper and manganese induce yeast apoptosis via different pathways. Molecular biology of the cell 18:4741-4749.